Vortex Induced Vibrations of Cylinders: Experiments in Reducing Drag Force and Amplitude of Motion

By

David Emmanuel Farrell

B.S., Mechanical Engineering
United States Naval Academy, 2005

Submitted in Partial Fulfillment of the Requirements for the Degree of
Master of Science in Mechanical Engineering

At the
Massachusetts Institute of Technology
And the
Woods Hole Oceanographic Institution

May 2007

Signature of Author..
Joint Program in Ocean Engineering/Applied Ocean Physics and Engineering
May 11, 2007

Certified by..
Michael S. Triantafyllou, Professor of Mechanical Engineering
Director, Center for Ocean Engineering
Thesis Supervisor

Certified by..
Franz S. Hover, Principal Research Engineer
Thesis Supervisor

Accepted by..
Lallit Anand, Professor of Mechanical Engineering
Chairman, Graduate Committee

REPORT DOCUMENTATION PAGE	*Form Approved* *OMB No. 0704-0188*

1. REPORT DATE *(DD-MM-YYYY)*	**2. REPORT TYPE**	**3. DATES COVERED** *(From - To)*
XX-05-2007	Master's Thesis	JAN-MAY 2007

4. TITLE AND SUBTITLE
Vortex Induced Vibrations of Cylinders: Experiments in Reducing Drag Force and Amplitude of Motion

5a. CONTRACT NUMBER
N62271-97-G-0026

5b. GRANT NUMBER

5c. PROGRAM ELEMENT NUMBER

6. AUTHOR(S)
David E. Farrell

5d. PROJECT NUMBER

5e. TASK NUMBER

5f. WORK UNIT NUMBER

7. PERFORMING ORGANIZATION NAME(S) AND ADDRESS(ES)
Massachusetts Institute of Technology

8. PERFORMING ORGANIZATION REPORT NUMBER

9. SPONSORING/MONITORING AGENCY NAME(S) AND ADDRESS(ES)
Naval Postgraduate School
Monterey, CA 93943

10. SPONSOR/MONITOR'S ACRONYM(S)
NPS

11. SPONSOR/MONITOR'S REPORT NUMBER(S)

12. DISTRIBUTION/AVAILABILITY STATEMENT
1. DISTRIBUTION STATEMENT A. Approved for public release; distribution is unlimited.

13. SUPPLEMENTARY NOTES

14. ABSTRACT
Reducing the deleterious effect of Vortex Induced Vibrations (VIV) in marine risers is an important task for ocean engineers; and many competing factors exist in the design of VIV suppression devices. This thesis explores the experimental minimization of the drag force and the disruption of the vortex formation by utilizing VIV suppression devices.

Two series of tests are conducted- both utilizing separate testing designs. The first tests are the flexible cylinder experiments, detailed in Chapter 2, which determine the drag force and vibration amplitude of numerous, original testing configurations. The second series of tests are the rigid cylinder, PIV experiments, detailed in Chapter 3. These rests measure both the drag force on the cylinder and the oscillating component of the lift force, the latter of which is a good indication of vortex formation. The Chapter 3 tests also image the test section wake- providing helpful insight into the physical process of vortex formation.

15. SUBJECT TERMS

16. SECURITY CLASSIFICATION OF: a. REPORT	b. ABSTRACT	c. THIS PAGE	**17. LIMITATION OF ABSTRACT**	**18. NUMBER OF PAGES**	**19a. NAME OF RESPONSIBLE PERSON** / **19b. TELEPHONE NUMBER** *(Include area code)*
			UU	92	Sean Tibbitts, Educational Technician / (831) 656-2319 civins@nps.edu

INSTRUCTIONS FOR COMPLETING SF 298

1. REPORT DATE. Full publication date, including day, month, if available. Must cite at least the year and be Year 2000 compliant, e.g. 30-06-1998; xx-06-1998; xx-xx-1998.

2. REPORT TYPE. State the type of report, such as final, technical, interim, memorandum, master's thesis, progress, quarterly, research, special, group study, etc.

3. DATES COVERED. Indicate the time during which the work was performed and the report was written, e.g., Jun 1997 - Jun 1998; 1-10 Jun 1996; May - Nov 1998; Nov 1998.

4. TITLE. Enter title and subtitle with volume number and part number, if applicable. On classified documents, enter the title classification in parentheses.

5a. CONTRACT NUMBER. Enter all contract numbers as they appear in the report, e.g. F33615-86-C-5169.

5b. GRANT NUMBER. Enter all grant numbers as they appear in the report, e.g. AFOSR-82-1234.

5c. PROGRAM ELEMENT NUMBER. Enter all program element numbers as they appear in the report, e.g. 61101A.

5d. PROJECT NUMBER. Enter all project numbers as they appear in the report, e.g. 1F665702D1257; ILIR.

5e. TASK NUMBER. Enter all task numbers as they appear in the report, e.g. 05; RF0330201; T4112.

5f. WORK UNIT NUMBER. Enter all work unit numbers as they appear in the report, e.g. 001; AFAPL30480105.

6. AUTHOR(S). Enter name(s) of person(s) responsible for writing the report, performing the research, or credited with the content of the report. The form of entry is the last name, first name, middle initial, and additional qualifiers separated by commas, e.g. Smith, Richard, J, Jr.

7. PERFORMING ORGANIZATION NAME(S) AND ADDRESS(ES). Self-explanatory.

8. PERFORMING ORGANIZATION REPORT NUMBER. Enter all unique alphanumeric report numbers assigned by the performing organization, e.g. BRL-1234; AFWL-TR-85-4017-Vol-21-PT-2.

9. SPONSORING/MONITORING AGENCY NAME(S) AND ADDRESS(ES). Enter the name and address of the organization(s) financially responsible for and monitoring the work.

10. SPONSOR/MONITOR'S ACRONYM(S). Enter, if available, e.g. BRL, ARDEC, NADC.

11. SPONSOR/MONITOR'S REPORT NUMBER(S). Enter report number as assigned by the sponsoring/ monitoring agency, if available, e.g. BRL-TR-829; -215.

12. DISTRIBUTION/AVAILABILITY STATEMENT. Use agency-mandated availability statements to indicate the public availability or distribution limitations of the report. If additional limitations/ restrictions or special markings are indicated, follow agency authorization procedures, e.g. RD/FRD, PROPIN, ITAR, etc. Include copyright information.

13. SUPPLEMENTARY NOTES. Enter information not included elsewhere such as: prepared in cooperation with; translation of; report supersedes; old edition number, etc.

14. ABSTRACT. A brief (approximately 200 words) factual summary of the most significant information.

15. SUBJECT TERMS. Key words or phrases identifying major concepts in the report.

16. SECURITY CLASSIFICATION. Enter security classification in accordance with security classification regulations, e.g. U, C, S, etc. If this form contains classified information, stamp classification level on the top and bottom of this page.

17. LIMITATION OF ABSTRACT. This block must be completed to assign a distribution limitation to the abstract. Enter UU (Unclassified Unlimited) or SAR (Same as Report). An entry in this block is necessary if the abstract is to be limited.

Vortex Induced Vibrations of Cylinders: Experiments in Reducing Drag Force and Amplitude of Motion

By

David Emmanuel Farrell

Submitted on May 14, 2007 in Partial Fulfillment of the
Requirements for the Degree of Master of Science in
Mechanical Engineering
At the Massachusetts Institute of Technology
And the Woods Hole Oceanographic Institution

ABSTRACT

Reducing the deleterious effect of Vortex Induced Vibrations (VIV) in marine risers is an important task for ocean engineers; and many competing factors exist in the design of VIV suppression devices. This thesis explores the experimental minimization of the drag force and the disruption of vortex formation by utilizing VIV suppression devices.

Two series of tests are conducted—both utilizing separate testing designs. The first tests are the flexible cylinder experiments, detailed in Chapter 2, which determine the drag force and vibration amplitude of numerous, original testing configurations. The second series of tests are the rigid cylinder, PIV experiments, detailed in Chapter 3. These tests measure both the drag force on the cylinder and the oscillating component of the lift force, the latter of which is a good indication of vortex formation. The Chapter 3 tests also image the test section wake—providing helpful insight into the physical process of vortex formation.

In brief, this thesis presents a detailed description and results of the two series of original VIV suppression tests. Many original configurations are tested, and the results are contained herein.

Thesis Supervisor: Michael Triantafyllou
Title: Professor of Mechanical Engineering

Thesis Supervisor: Franz Hover
Title: Principal Research Engineer

About the Author

David Emmanuel Farrell was born April 12th, 1983 in Santa Ana, California. He is the third of six children of Daniel and Wanda Farrell. He has two older brothers—Nick and Jesse, and three younger sisters—Heidi, Autumn, and Amy.

David has many interests: including swimming, dancing, boxing, cooking, talking to strangers, manual labor, learning about world affairs, trying new things, and discussing the most important lessons of life. He does not watch television or own an Ipod because he wants to experience life firsthand.

He went to college at the U.S. Naval Academy where he studied mechanical engineering, and learned many other lessons that can't be taught in a classroom. He now looks forward to a career of naval service; and later, other assignments in service of the United States and the many, many other valuable countries and people in this world.

Acknowledgments

Many people deserve heartfelt thanks for their time, and desire while assisting me during these past two years of graduate study. My fellow graduate students in the "tow tank" were of enormous assistance to each other and to me throughout this time. One of the things that I was most impressed with about the tow tank crew, was the willingness of everyone to assist each other—literally, all you had to do is ask! These wonderful people include Evan Lee, Ricardo Galvao, Jason Dahl, Stephen Licht, Pradya Prempraneerach, Vicente Fernandez, Matt Greytak, Matt Unger, and Matthias Blonnegin.

I'd like to thank my thesis advisors, Michael Triantafyllou and Franz Hover for their constant guidance throughout the research process. I am particularly thankful for their continuous commitment to actively participate in the research of their graduate students—manifested by meeting with all of their students at least once on a weekly basis. Advising their students is not a responsibility that either of them takes lightly.

I'd like to thank each member of my family for constant encouragement throughout this time! It is certainly assuring to know how much they love and support me.

I'd like to thank all of the great friends that I've made in the area while at school and at church, and out in the city. I don't want to get into a huge list of naming people, but, if you are reading this, assume that I am talking about you!

I give a very special thank you to Mark Belanger, Tony Calogerro, and Andrew Carvey at the Edgerton Student Machine Shop for all the help with machining so many different items. Thank you to Ken Stone for the help at the MIT Hobby Shop; and thank you to Gus Tipps of Freestyle CNC in Walworth, Wisconsin for his excellent craftsmanship and timely delivery of custom machined parts.

I'd like to thank the British Petroleum Company both for providing the funding to conduct these experiments, and also for allowing the publication of the results from these tests. I'd like to thank the Office of Naval Research for funding part of my tuition during these years of study. Based upon the knowledge and experience gained—I'd consider it money well spent. Lastly, I'd like to thank the United States Navy, and more specifically the aviation community, for allowing me the time to pursue this graduate degree. Again, I am confident that this was time well spent.

Contents

List of Figures

List of Tables

Chapter 1

Introduction

1.1 Marine Risers

The oil industry utilizes many types of "marine risers" (which include the structural support, drilling tubes, electronic conduits, and the oil transport cylinders in its oil platforms) to link the sea surface and the sea floor. These risers are essential lifelines between the sea surface and the sea floor. As the drilling of oil tends towards deeper waters, more platforms are becoming floating structures that require risers that are freely strung from the platform to the sea floor as shown below.

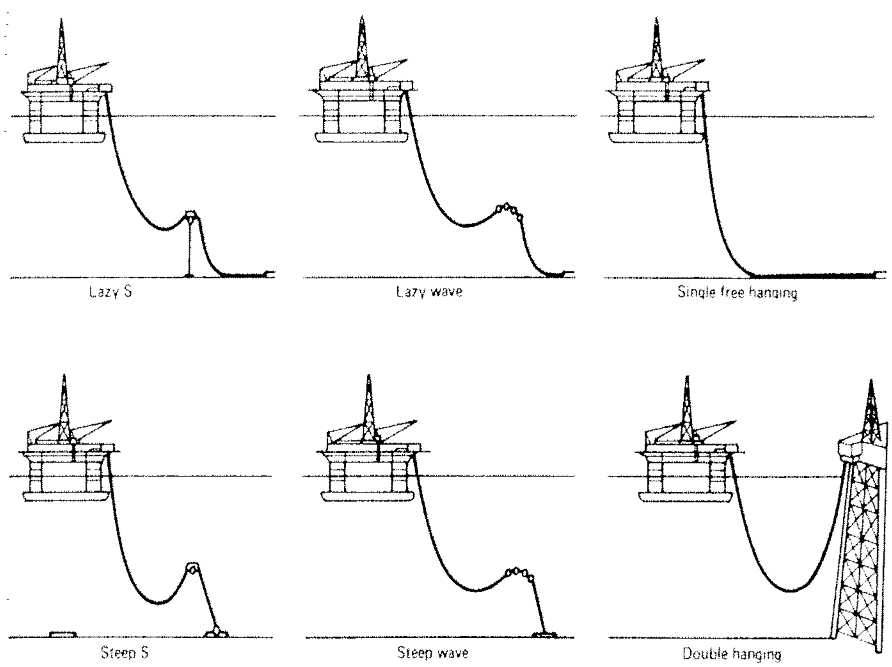

Figure 5.26 Flexible risers; an illustration of current configurations

Figure 1-1: Marine Riser Illustration (Morgan, 1990)

1.2 Vortex Shedding

Swirling masses of water are "shed" into the wake of a cylinder subjected to a cross-flow. These masses of water (called vortices) possess lower pressure than the fluid that surrounds them (described by the Bernoulli Effect), and thus they transmit a pulling force onto the cylinder that sheds them.

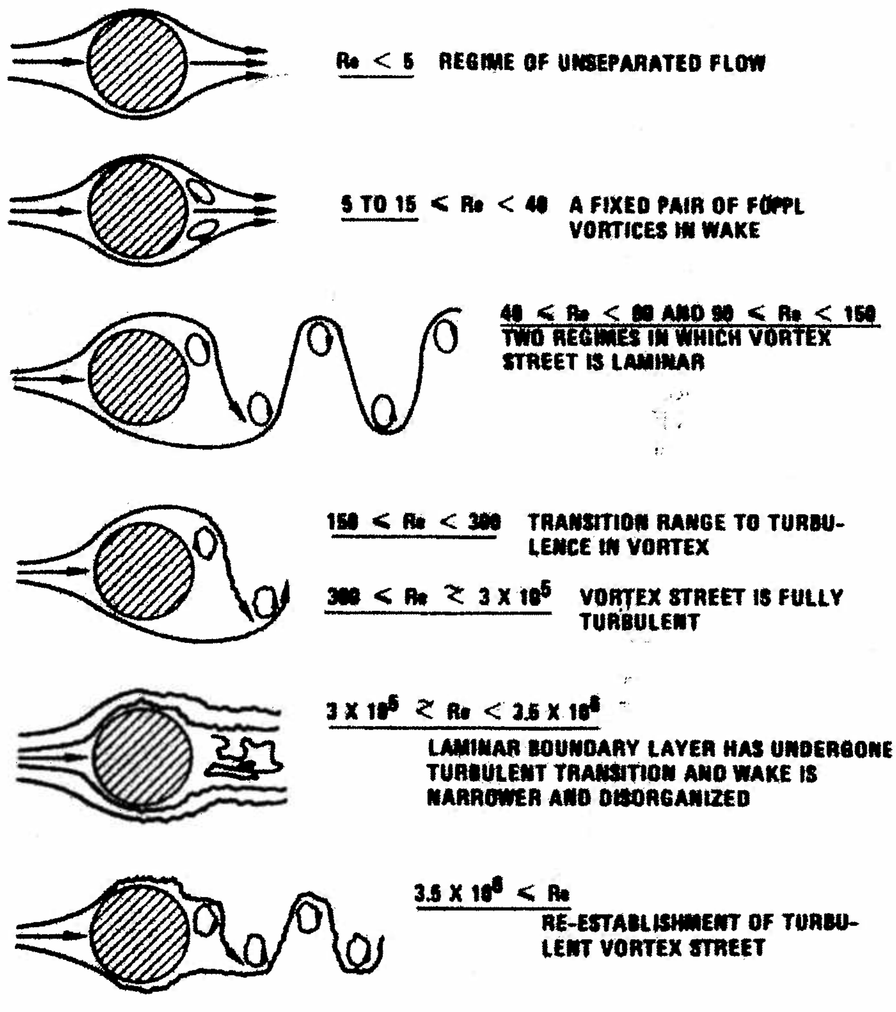

Figure 1-2: Cylinder Wake Pattern vs. Reynolds Number (Wiggins, 2005)

Shown above in Figure 1-2, the flow of water begins to separate off of a cylinder in the region of Reynolds number 5 to 15. Where Reynolds number, Re, is defined in Equation (1.1):

$$Re = \frac{\rho U D}{\mu} \tag{1.1}$$

Where ρ is the density of the fluid, U is the free-stream velocity of the fluid, D is the cylinder diameter, and μ is the dynamic viscosity of the fluid. As is seen in Figure 1-3 below, the rotation direction of a vortex is visualized by realizing that the "free-stream" velocity is higher than the velocity inside the wake of the cylinder.

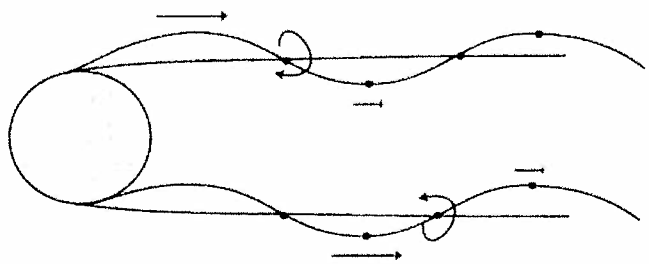

Figure 1-3: Flow Instabilities Developing in Cylinder Wake

Figure 1-4 shows a computer generated image taken from a Particle Image Velocimetry (PIV) experiment at the MIT towing tank. The red circle is a vortex rotating counter-clockwise, and the blue circle is a vortex rotating clockwise (the flow direction in this picture is from left to right). On the right is a picture of vortex formation in the clouds behind an island in the ocean. Vortex shedding is not merely a small scale phenomenon.

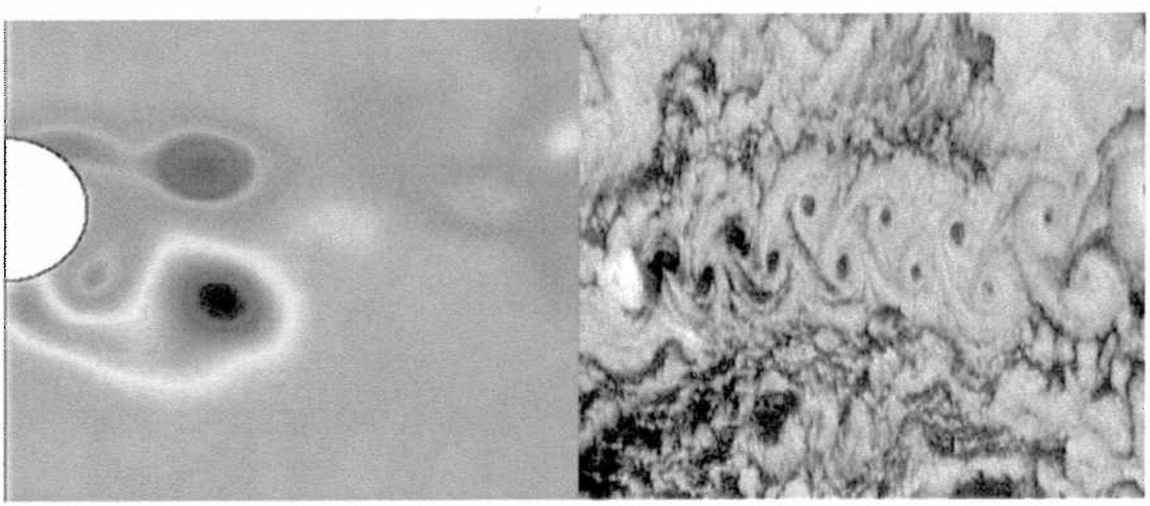

Figure 1-4: Vortex Wake, Small Scale ~cm (left), Large Scale ~100km (right)

The speed of the cross-flow determines the vortex shedding frequency, according to the Strouhal number, S, defined by Equation (1.2):

$$S = \frac{f_s D}{U} \tag{1.2}$$

Where f_s is the vortex shedding frequency, D is the diameter of the body, and U is the free stream velocity. As is shown in Figure 1-5 below, the Strouhal number remains nearly equal to 0.2 for the range of Reynolds numbers 300-100,000. Hence, in this range of Reynolds numbers, the vortices are shed from a cylinder at a frequency directly proportional to $0.2\frac{U}{D}$.

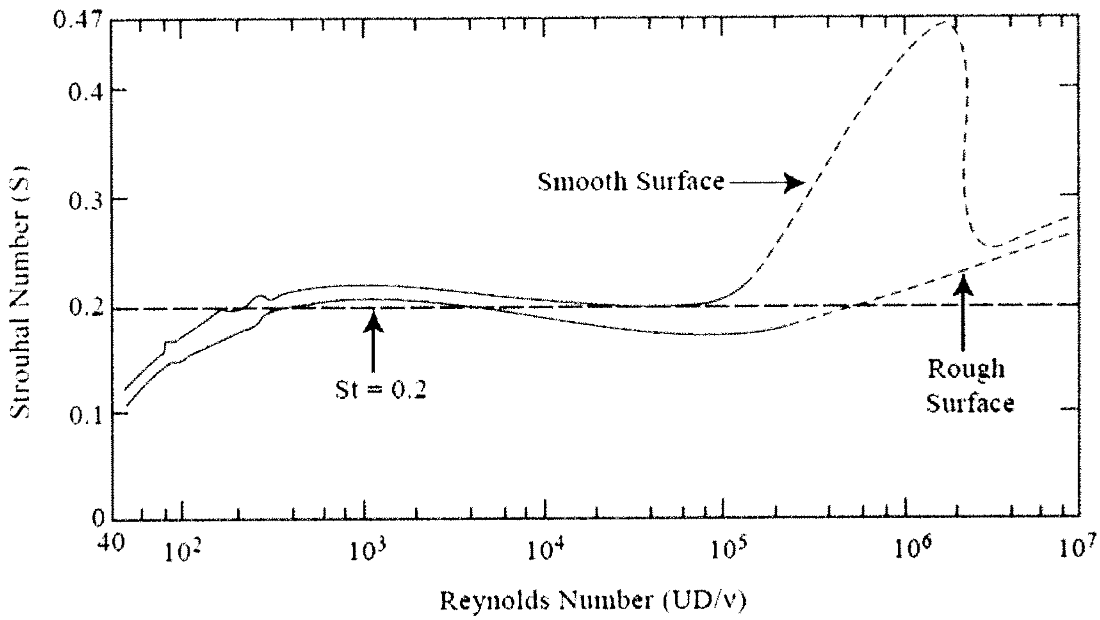

Figure 1-5: Strouhal Number vs. Reynolds Number (Circular Cylinder) (Techet, 2005)

1.3 Vortex Induced Vibrations

If the vortex shedding frequency is near a natural frequency of the cylinder, then the cylinder will undergo sustained oscillations. These oscillations are called "vortex-induced vibrations" (VIV), and will persist as long as the vortex shedding continues.

VIV is especially prominent with the marine risers of oil platforms in the Gulf of Mexico where the Gulf "loop current" remains a consistent source of cross-flow. Shown in

Figure 1-6 is map of the Gulf of Mexico displaying the strength of surface currents with arrows. Shown in white are the arrows that are typically defined as the "loop current."

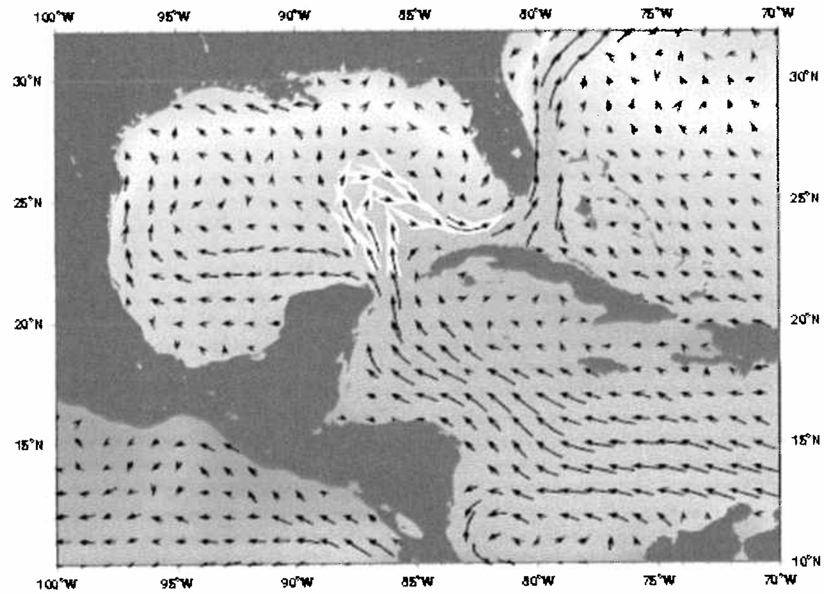

Figure 1-6: Surface Currents in the Gulf of Mexico (Gyory, 2007)

It is well known that hurricanes are also prevalent in the Gulf of Mexico. The intense winds from hurricanes can also cause large currents and waves that excite VIV in marine risers. Figure 1-7 shows an oil platform in the Gulf of Mexico damaged by a hurricane.

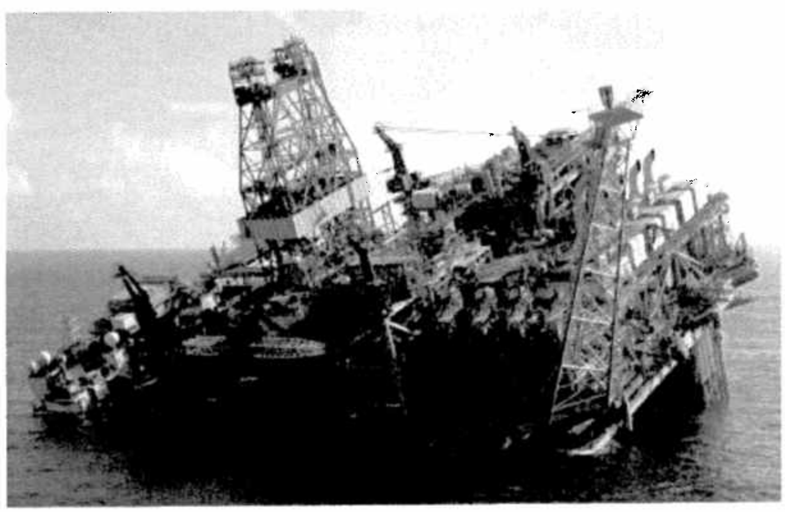

Figure 1-7: Hurricane Damage to an Oil Platform (Wood, 2005)

The severity of VIV typically has two standards of measure: the amplitude of vibration, and the mean drag force. Both of these standards are usually reported in their non-

dimensional form as (amplitude of motion/ diameter of the cylinder) A/D, and (coefficient of drag) C_d, respectively.

1.3.1 Drag Reduction

It is desired to lower the total drag force experienced by a marine riser, because large forces can cause yielding or failure at critical points along the riser length. It is noted that the total drag force of a riser is a combination of forces from both waves and from currents, but in this thesis only the drag force resulting from currents is examined (experiments including both waves and currents is suggested for future work). The mean drag force, F_d, of an object in a current, or cross-flow, can be described Equation (1.3):

$$F_d = \frac{1}{2}\rho U^2 A_f C_d \tag{1.3}$$

Where ρ is the density of the fluid, U is the velocity of the fluid, A_f is the frontal area of the object (equal to the length times the diameter for a cylinder), and C_d is the coefficient of drag. The coefficient of drag for a cylinder varies with Reynolds number, and is shown below in Figure 1-8.

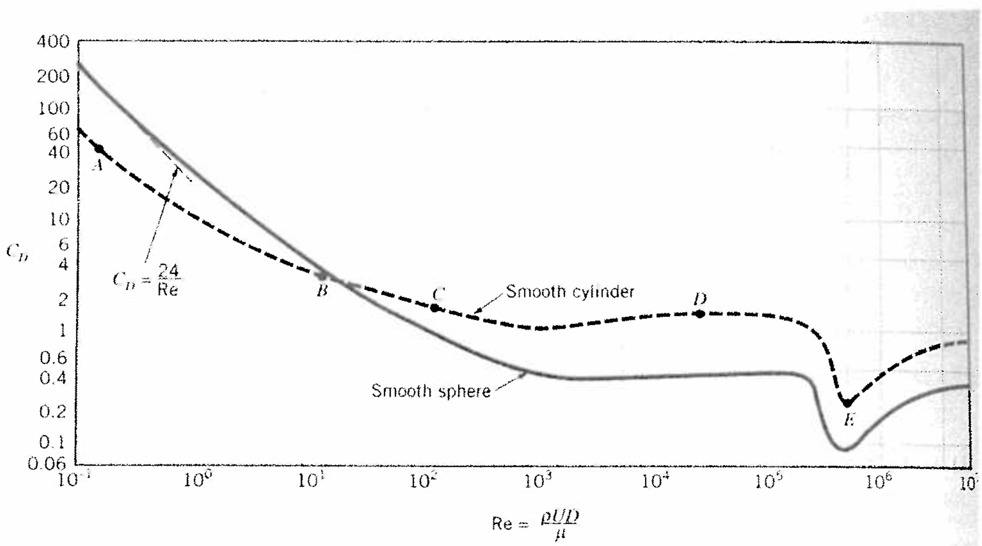

Figure 1-8: Coefficient of Drag vs. Reynolds Number (Munson, 2002)

All of the tests conducted in this report are in the range of Reynolds numbers from 10^3 to 10^5, so the expected value of Cd, is on the order of 1.2 as is seen above. It is essential to

note that the above figure describes the coefficient of drag versus Reynolds number for a fixed cylinder with rigid supports. However, if the cylinder is flexible or if it is mounted on flexible supports, then the coefficient of drag will increase significantly when the cylinder undergoes VIV. As a rule of thumb, the larger the wake behind a cylinder, the larger the drag force the cylinder will experience; and a cylinder that is oscillating due to VIV will have a much larger wake than a fixed cylinder on rigid supports. Hence, it is essential to keep cylinder vibrations as small as possible during VIV.

1.3.2 Amplitude of Motion Reduction

Reducing the vibration amplitude of a cylinder experiencing VIV is of paramount importance. As mentioned above, the larger the amplitude of vibration, the larger the drag force on the cylinder. An empirical chart that approximates the relationship between the amplitude (A/D) and the coefficient of drag (Cd) is shown below in Figure 1-9.

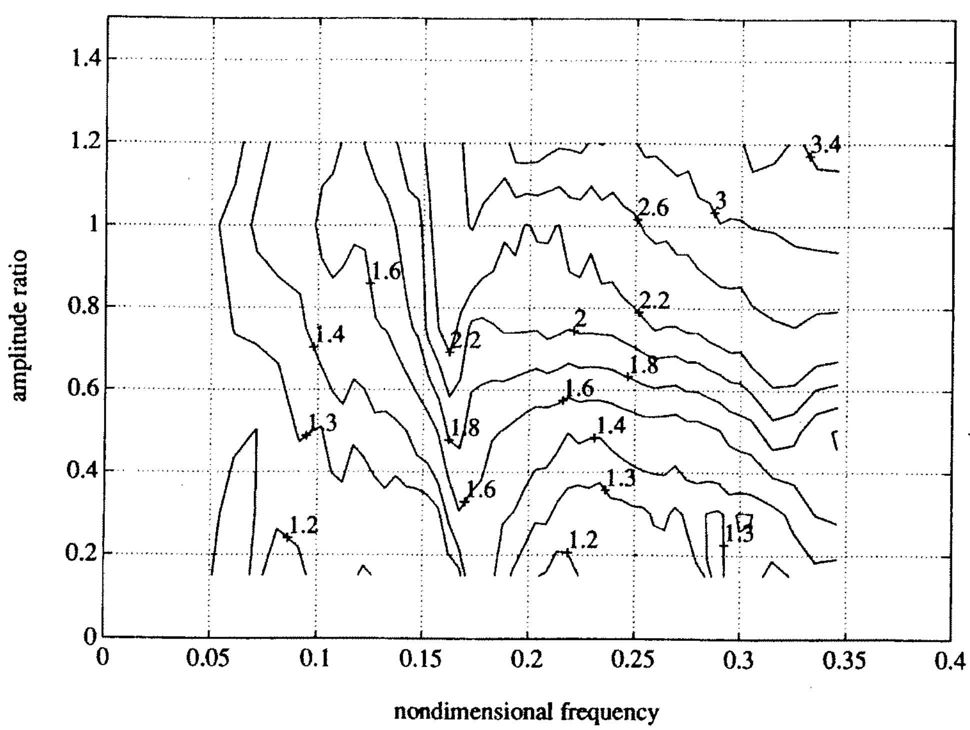

Figure 3-12: Contours of the mean drag coefficient; sinusoidal oscillations.

Figure 1-9: Mean Drag Coefficient Contours vs. Frequency and Amplitude (Gopalkrishnan, 1993)

Another major consequence of VIV is the danger of fatigue failure of critical areas along the riser length. A typical chart showing the number of "cycles" until fatigue failure of a steel rod is shown below in Figure 1-10. Notice that fatigue failure of the rod is predicted after only 10^6 cycles in bending (when the peak alternating stress is equal to half of the ultimate strength of the steel). In marine risers, due to the relative high frequency of vortex shedding, this number of cycles can be achieved quickly. As an example: if the flow speed, U, equals 1 m/s, the diameter of the riser, D, equals 1 m, and the Strouhal number equals 0.2, then the shedding frequency will equal 0.2 Hz. At 0.2 Hz, it will take less than 60 days for 10^6 vortices to shed.

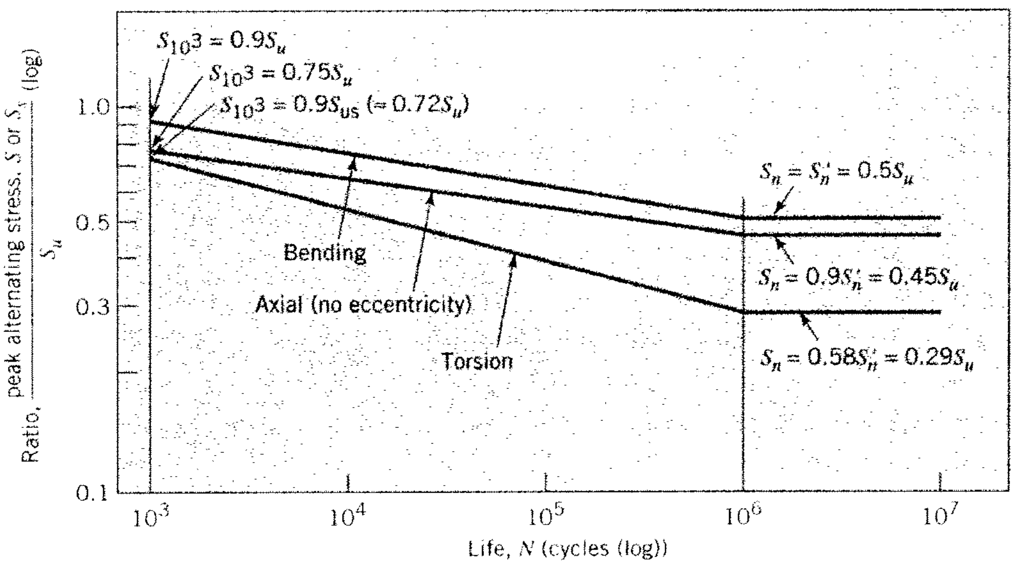

FIGURE 8.11
Generalized S–N curves for polished 0.3-in.-diameter steel specimens (based on calculated elastic stresses, ignoring possible yielding).

Figure 1-10: Stress vs. Life Cycle Curves (for Steel) (Juvinall, 2000)

The other way to increase the fatigue life of the riser, of course, is to decrease the amount of stress in each cycle of motion. Again, this is achieved by decreasing the amplitude of motion of the riser.

1.4 Existing Solutions

Much effort has already been made in suppressing VIV; and the tests that have been completed share the same goal of disrupting the vortex formation process while keeping the drag force to a minimum. It seems that the only limit to the testing possibilities is ones imagination. Shown in Figure 1-11 are 24 previously tested configurations of cylinders (with accoutrements) that are designed to suppress VIV. Each configuration shows both a side view, and a head-on view of the cylinder tested. A + sign indicates that the configuration successfully lowered the amplitude of cylinder vibration, while a – sign indicates that it did not. A number inside the circle of the head-on view indicates the coefficient of drag for that particular configuration.

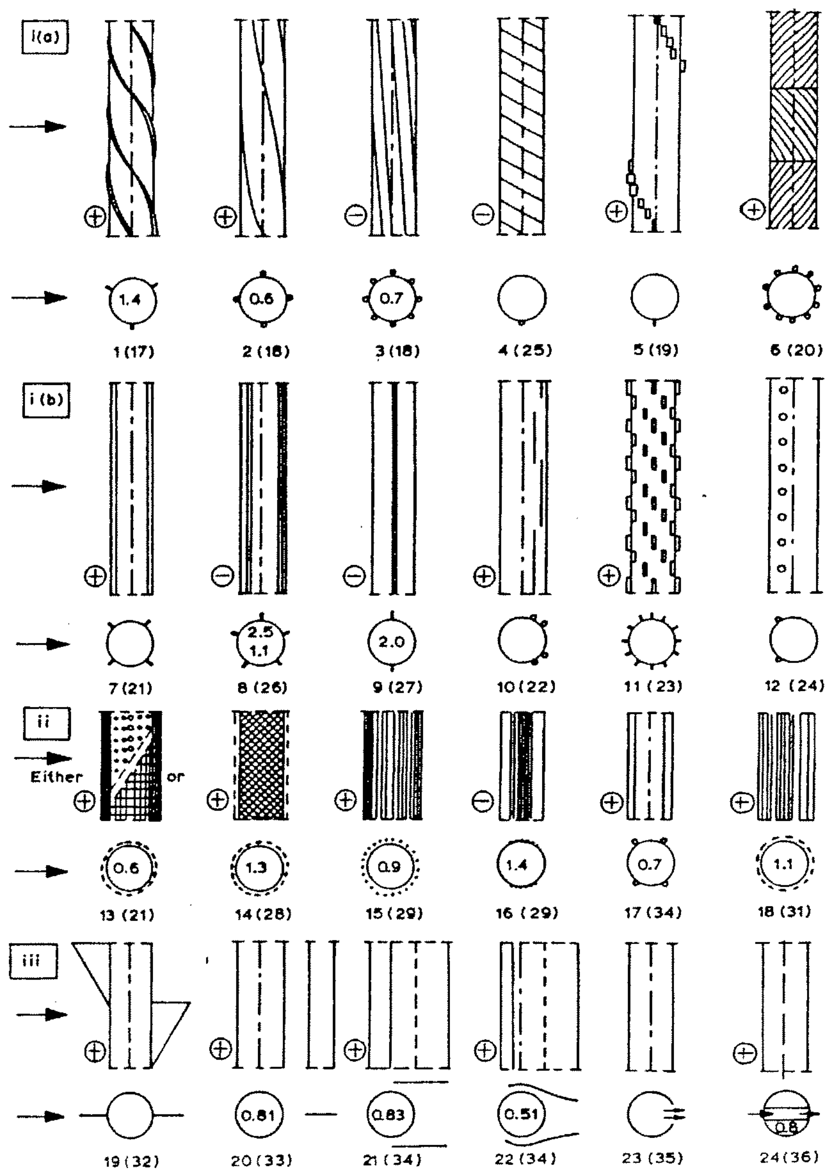

Figure 1-11: Previously Tested VIV Suppression Devices (Zdravkovich, 1980)

Notice that the suppression devices above are displayed in categories corresponding to similarities between the devices. Group i(a) are all "omnidirectional" surface protrusions. "Omnidirectional" means that the cylinder and the flow will interact the same way—independent of the direction of flow arrival. Group i(b) are all unidirectional surface protrusions—meaning that the interaction between flow and cylinder is flow direction specific. Group ii are all "shrouds", termed as such because they densely cover, or shroud, the surface of the cylinder; and group iii are called "near-wake stabilizers" because they try to stabilize the wake behind the cylinder (hence preventing VIV). In this report, further tests are conducted in all of the groups—with the exception of group ii ("shrouds").

A current state-of-the-art VIV suppression device for overhead power lines (in air) is a cylinder that is elliptical in cross-section and spirals down its length. A picture of this cylinder is shown below in Figure 1-12 and is taken from US Patent No. 6,353,177, titled "Vibration Resistant Overhead Electrical Cable". The same idea (an elliptically spiraling cable) is tested in this report for VIV suppression in water.

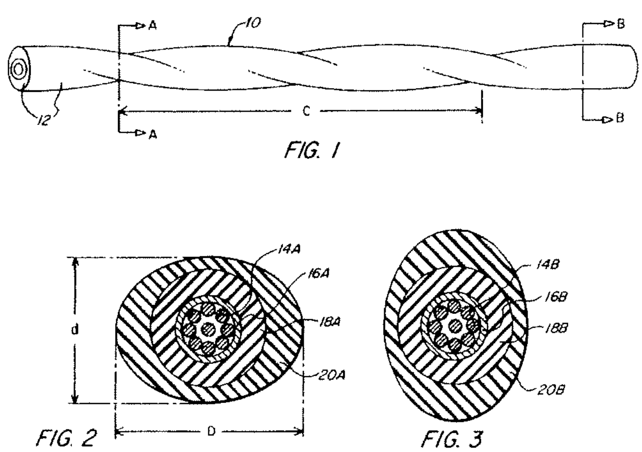

Figure 1-12: Elliptical Cross-Section Spiral Overhead Electrical Wire (Young, 2002)

1.5 Thesis Goals

The purpose of this thesis is to push the envelope of the current state-of-the-art in VIV suppression devices. Several varieties of devices are tested, and the results are presented herein. The varieties tested include omnidirectional and unidirectional surface protrusions, and near-wake stabilizers. In order to best accomplish this task, the experimental setup and testing strategy changes with each chapter. Stated again—the overarching theme of all VIV suppression tests is to lower the drag force and amplitude of motion of the test section.

Chapter 2

Flexible Cylinder Experiments

2.1 Motivation

This chapter details the results of tests conducted with flexible cylinders; primarily with one central cylinder and two or three accompanying smaller cylinders. The approximate diameter ratio of the central cylinder to the smaller cylinder is 2:1. These tests assume that the smaller cylinders are flexible enough to be wrapped around the main riser in various configurations. One example of the application of this experiment is on an offshore oil platform where the main riser pipe (rigid) and the (flexible) blow-out preventer (BOP) pipes travel alongside each other to the depths.

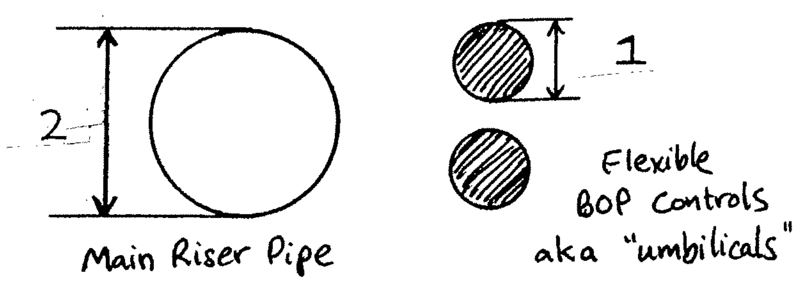

Figure 2-1: Cylinder Diameter Ratio Picture

The results of the flexible, elliptical spiraling cross-section cylinder are also shown in this chapter. In most cases, the amplitude of motion (A/D), and drag (C_d) are displayed over a range of reduced velocities, where reduced velocity, Vr, is defined in Equation (2.1):

$$Vr = \frac{U}{f_n D} \tag{2.1}$$

Where U is the flow speed, f_n is the natural frequency of the riser pipe test section (1^{st} mode), and D is the riser pipe test section outer diameter. The testing results are intentionally displayed using only non-dimensional parameters (A/D, C_d, and Vr) so that are easily compared with other experiments and real-world applications.

2.2 Testing Apparatus

2.2.1 General Setup

All of the tests from Chapters 2, and 3 were conducted in the MIT towing tank. The dimensions of the tank are approximately 30 m length, 2 m width, and 1 m depth (depth is variable). The testing apparatus consists of a belt and pulley driven by an electric motor. The term "carriage" is used to describe the part of the system that is rigidly attached to the belt and is driven along a rail down the length of the tank at the speed of the belt. Shown in Figure 2-2 is a picture of the test section, the sensing elements, and the tensioning mechanism (spring) for the flexible cylinder tests. The elliptical test section is shown.

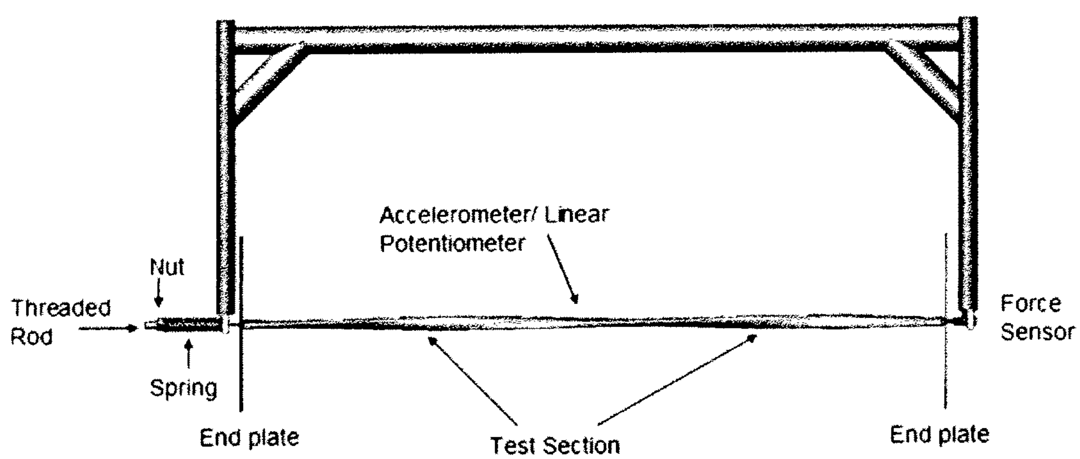

Figure 2-2: Flexible Cylinder Testing Apparatus

The above figure shows the arrangement of the test section during the experiments. The carriage velocity is into the page. As shown, the test section was attached with a force

sensor on one end. It was assumed that this force sensor measured only half of the force applied to the length of test section (because a simply supported beam with equally distributed forcing sees equal forces on both of its ends, and hence each end only sees half of the total load). The end plates helped to guarantee a two-dimensional flow across the test section. The other end of the test section was attached to a threaded rod. As is shown in the figure, a nut traveled down the threaded rod and compressed a spring which in turn tensioned the test section. Raising the tension in the test section raised its natural frequency, f_n (Hertz), according to the following equation for the natural frequency of a string:

$$f_n = \frac{n}{2L}\sqrt{\frac{T}{\rho}} \tag{2.2}$$

Where n is the mode number (we define the natural frequency of the first mode with n = 1), L is the length of the test section (m), T is the tension (N), and ρ is the mass of the test section per unit length (kg/m). The natural frequency for each experiment tended to vary in the range of 3-5 Hz, but each cylinder configuration was tested at a consistent set of reduced velocities (Vr). The natural frequency of each cylinder configuration was measured by perturbing the cylinder in air, and measuring the resulting force fluctuations due to the first-mode oscillations. "Pluck testing" was the phrase used to describe this procedure, and a typical time series is shown below in Figure 2-3.

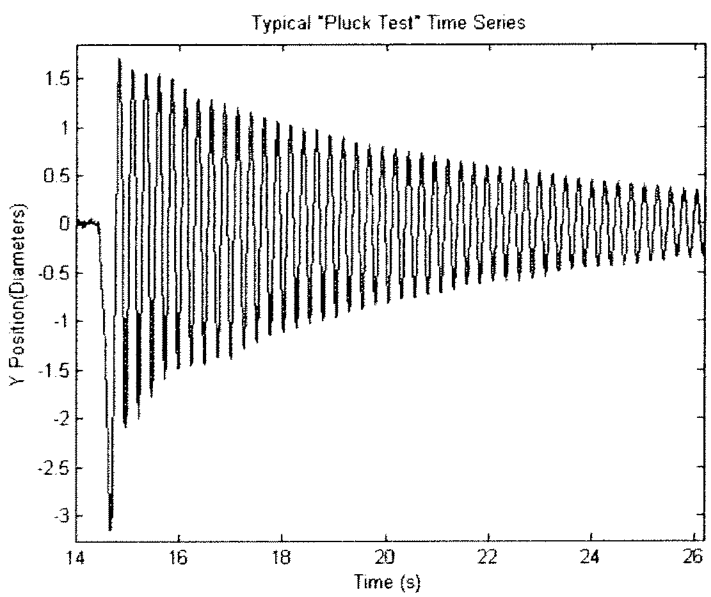

Figure 2-3: Pluck Test of Flexible Cylinder

From these "pluck test" graphs, the natural frequency of each configuration was determined (3.93 Hz as shown above) and the damping ratio of the system was also calculated (about 0.5% of critical damping for the time series shown). Such a low damping ratio from an in air "pluck test" indicates that if significant damping is present in the system during an experiment it is primarily hydrodynamic in origin.

An important side note that may help to clear up common confusion: in Chapter 2, the test section lies parallel to the plane of the water surface, but in Chapter 3, as in many marine riser systems, the test section is perpendicular to the water surface. Additionally, in all of the tests the *test section* is moved while the *water* remains stationary. The assumption in these tests is that the vibration amplitude and drag force of each test section relies only on the *relative* motion of the water with respect to the test section, not on the absolute orientation of the test section or of the flow.

2.2.2 Cylinder Construction

The flexible cylinder tests had an interesting set of design parameters:

1. Be able to tension the test section so that the natural frequency can be adjusted.
2. Minimal deformation of the test section is desired as a result of the tensioning.
3. No twisting or torque-ing motion is allowed of the test section during tests.
4. The test section material must be compliant enough to allow vortex-induced-vibrations.

The devised solution to these parameters was to create a cylinder out of a two-part, pourable rubber compound, with two Kevlar strings embedded into the rubber down the length of the cylinder. The high-strength of the Kevlar allowed the cylinder to be tensioned with minimal deformation, the flexibility of the rubber allowed VIV, and the having two separate Kevlar strings spaced apart from one another prevented any twisting of the cylinder during the runs.

The type of rubber used was PMC-724, made by Smooth-On Inc. PMC-724 has a specific gravity of 1.38, and a Shore A hardness rating of 40. This rubber was chosen due to its low viscosity (before hardening), good flexibility, and specific gravity close to one.

To fabricate the central cylinder, the inside of a PVC pipe was used as a mold for the poured rubber, and PVC end caps were used to seal the ends of the PVC pipe while the rubber hardened. Two small holes in the each PVC end cap allowed the two Kevlar strings to pass through the cylinder as the rubber hardened. As discussed above, after the rubber in the test section was set, these Kevlar strings were secured to a force sensor on one end of the test section and a threaded rod/spring tensioning mechanism on the other.

The smaller cylinders used in these tests were 5/8" garden hose commonly found in stores. Garden hose was chosen due to its availability, flexibility, and fulfillment of the 2:1 diameter ratio criteria. The design criteria of the smaller cylinders was less exacting then the central cylinder because Kevlar strings did not have to be embedded in the smaller cylinders—the only requirements were flexibility and correct outer diameter. Cable ties were used to attach the central cylinder and the garden hose (at several points down the length). An example of how this looked during a run is shown in Figure 2-4 ("configuration 3" is shown).

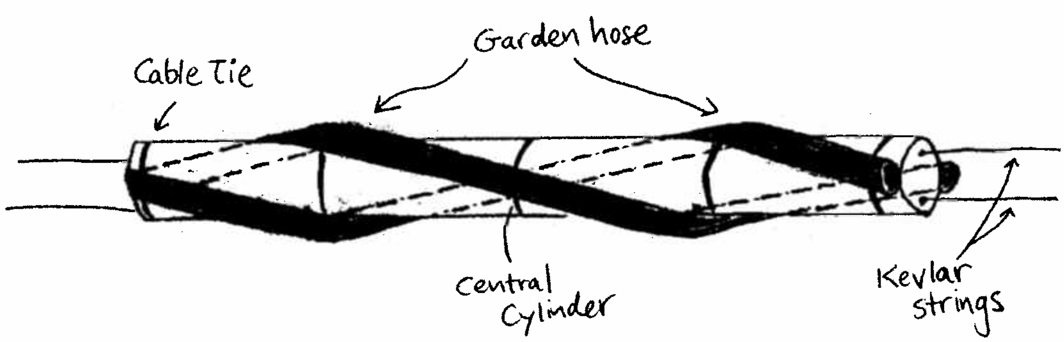

Figure 2-4: Flexible Cylinder with Garden Hose Attached

In the case of the elliptical cross-section spiral cylinder, a mold was custom machined out of aluminum. Half of the mold is shown below in Figure 2-5 (split in half so that the

contours can be seen). Similar to the circular cross-section cylinder, PMC- 724 rubber was poured into this elliptical mold while the Kevlar strings were strung down the length.

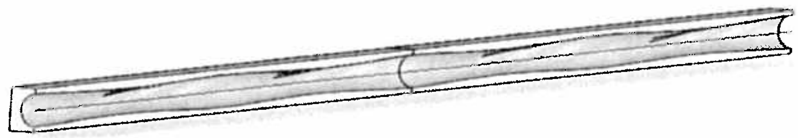

Figure 2-5: Elliptical Cross-Section Spiral Mold

2.3 Sensing and Data Processing

2.3.1 Accelerometer

In order to measure the amplitude of VIV and to retrace the path of cylinder motions of the experiments, a tri-axial, piezoelectric accelerometer was embedded into the rubber of the cylinder. The maximum acceleration that was expected during the VIV was 15.7 g's (this assumes the maximum towing speed of the tank (1.5 m/s) and an A/D of 1.5). Thus, an accelerometer with ±50 g range was chosen to provide ample range.

The accelerometer used is shown in Figure 2-6. The cubic geometry of the accelerometer allowed for easy alignment of the axes.

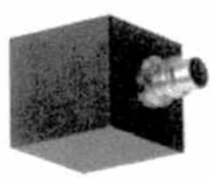

Figure 2-6: Triaxial Accelerometer (Kistler, 2007)

The accelerometer output was in units of mV/g; and according to the calibration provided by the manufacturer (Kistler Instruments) the nominal sensitivity of each accelerometer axis was 100 mV/g. This calibration was corroborated by a ± 1g static calibration conducted in the lab.

By double integrating the accelerometer output, the position of the cylinder was obtained. A high-pass Butterworth filter was implemented (forwards and backwards) to eliminate low frequency integration error without introducing any phase shift. Amplitude of motion peaks were picked off of the time series of the position graph. Figure 2-7 shows a plot of the elliptical cross-section cylinders motion over about twelve cycles of figure-eight motion. It is shown that the accelerometer does a good job of retracing the figure eight motion path of the cylinder.

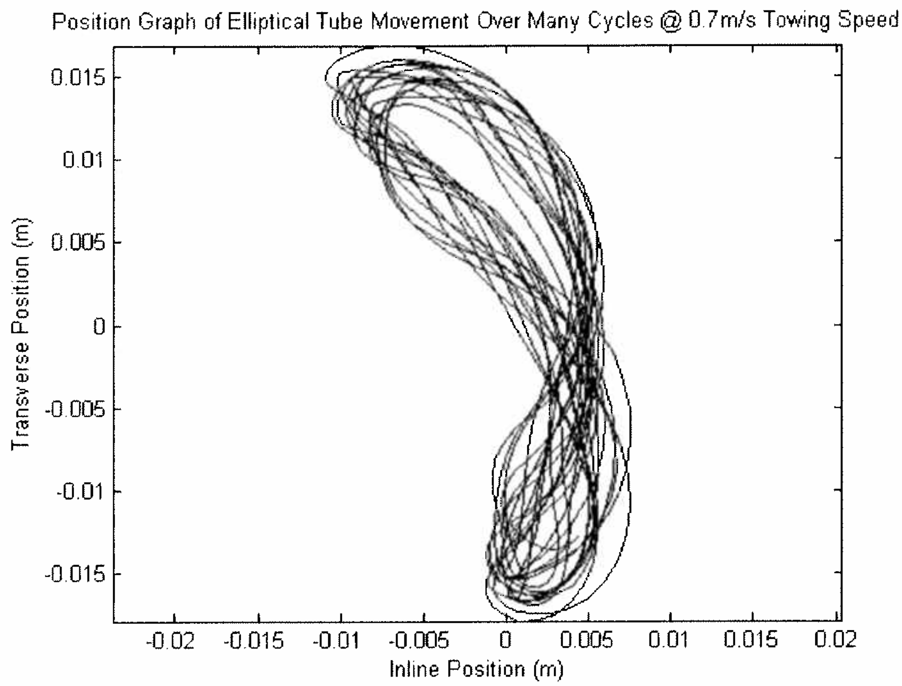

Figure 2-7: Elliptical Cross-Section Spiral Orbit

It proved difficult, however, to maintain a water-tight seal of the accelerometers during the underwater tests. Also, the plots of figure-eight motion did not contain specific information of interest (other than the peak values of A/D), so a linear potentiometer was implemented for the remainder of the tests to measure the amplitude of motion.

2.3.2 Linear Potentiometer

A linear potentiometer measures displacement directly. In this case, a wire is extended outside of the transducer housing and the displacement of the outstretched wire is

recorded. For this experiment, the transducer housing was secured to the carriage directly above the test section, and the wire extended down into the water and terminated into the middle of the test section. In this way, the linear potentiometer measured the transverse amplitude of vibration of the test section at the location with the maximum first mode response. A picture of the linear potentiometer, made by UniMeasure Inc., is shown below in Figure 2-8.

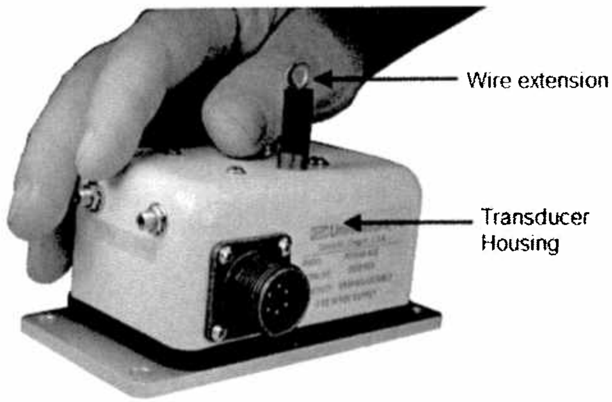

Figure 2-8: Linear Potentiometer (UniMeasure, 2007)

Three assumptions are made here that should be noted. First, it is assumed that the wire itself does not disrupt the wake of the test section. Since the wire is only 0.016 inches in diameter (compared to the 1.36 inch diameter cylinder), and the wire itself is not directly inside the wake of the cylinder—this assumption seems justified.

Second, it is assumed that the small amount of tension in the wire does not effect the cylinder vibrations. The high amount of tension in the Kevlar strings (supporting the test section) does not allow the test section to visibly deflect under its own weight. The high tension in the Kevlar is also what permits the claim that the test section vibrates with the same response when moving parallel to the surface of the water as if it were moving perpendicular to the surface of the water—as is the case with a marine riser. Even so, any amount of tension in the linear potentiometer wire only acts to counteract the off-balance in the negative buoyancy of the test section due to the specific gravity of rubber (1.38). Therefore this assumption is also justified.

Third, it is assumed that the potentiometer wire is only measuring transverse (perpendicular to the flow) cylinder motions. Since very large inline (same direction as the flow) motions are only on the order of 0.5 A/D, and since the test section was located further than 20 diameters from the transducer housing, very large inline motions would only produce an extension in the wire less than one percent of one diameter. Thus, wire extensions due to inline motions are neglected, and it is assumed that the linear potentiometer only measures transverse motions. The geometry behind this reasoning is shown in Figure 2-9, and utilizes the Pythagorean Theorem.

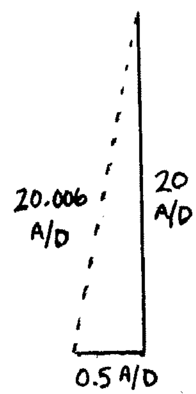

Figure 2-9: Transverse Oscillation Justification

As an aside, it is noted that the maximum amplitude of vibration of a cylinder subjected to a cross-flow is usually in the transverse (perpendicular to the flow) direction. While at low reduced velocities ($Vr < 3$) inline vibrations can dominate, transverse vibrations dominate at reduced velocities greater than 4. Transverse vibrations also tend to have the most significant impact on drag force measurements. For these reasons, the values for A/D ratio displayed in this report refer to transverse oscillations. Because transverse oscillations dominate, it is justifiable to use a linear potentiometer (that is only capable of measuring transverse oscillations) instead of a triaxial accelerometer.

2.3.3 Force Sensor

A three-axis, piezoelectric force sensor was used in these tests to measure the forces in the drag, lift, and tension directions. Only the drag force measurement was analyzed in

these tests. Figure 2-10 shows a picture of the force sensor (made by Kistler Instruments).

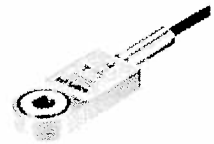

Figure 2-10: Three-Axis Force Sensor (Kistler, 2007)

The circular hole near the bottom left of the instrument contains the sensing element and the wire leading out of the upper right contains the power and data acquisition wiring.

Figure 2-11 shows a typical drag time series during a testing run. The average value of the "steady drag" component is the part used to calculate the coefficient of drag for each run. "Transient" refers to the times when the carriage is accelerating or decelerating.

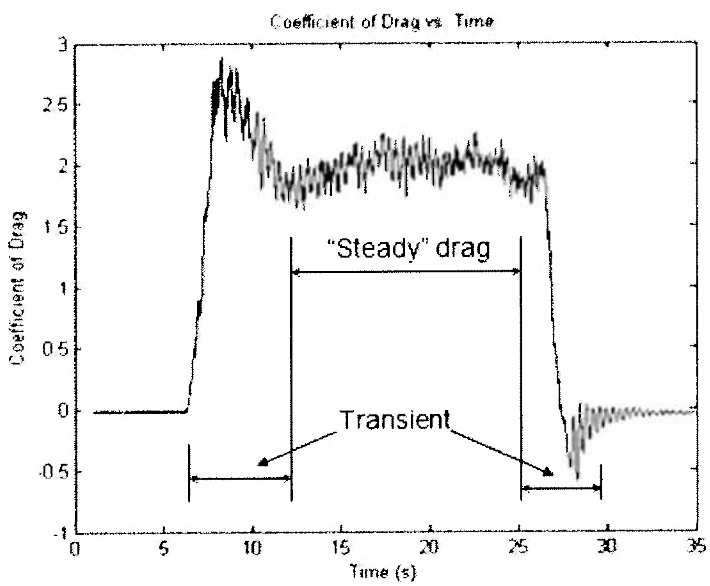

Figure 2-11: Drag Time Series Example

2.4 Pictures and Results

Each section that follows presents the experimental results for an individual testing configuration. Skip to section 2.5 for a summary of the results for all the flexible experiment tests.

2.4.1 Configuration 0

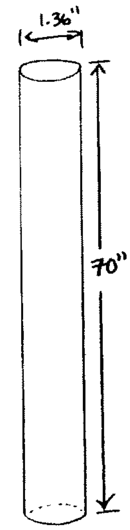

Configuration 0 was tested extensively so that a fully populated baseline could be established for the other tests. Figure 2-12 shows the cylinder vibration amplitude as a function of reduced velocity. Notice that at reduced velocity greater than nine, the amplitude of vibration begins to drop. This occurs because the vortex shedding frequency (the excitation frequency of the system) is becoming further away from the cylinder natural frequency—hence the two are no longer "locked" together, and vibrations decrease.

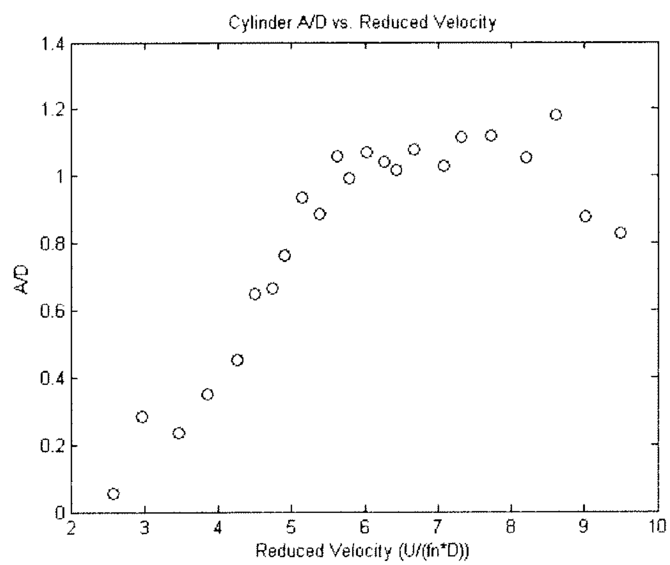

Figure 2-12: Cylinder A/D vs. Vr

Figure 2-13 shows the drag coefficient as a function of reduced velocity. Notice that the first data point (at reduced velocity ~2.5), the drag coefficient equals 1.2. This corresponds to the nominal drag coefficient for a cylinder that is not oscillating in a flow.

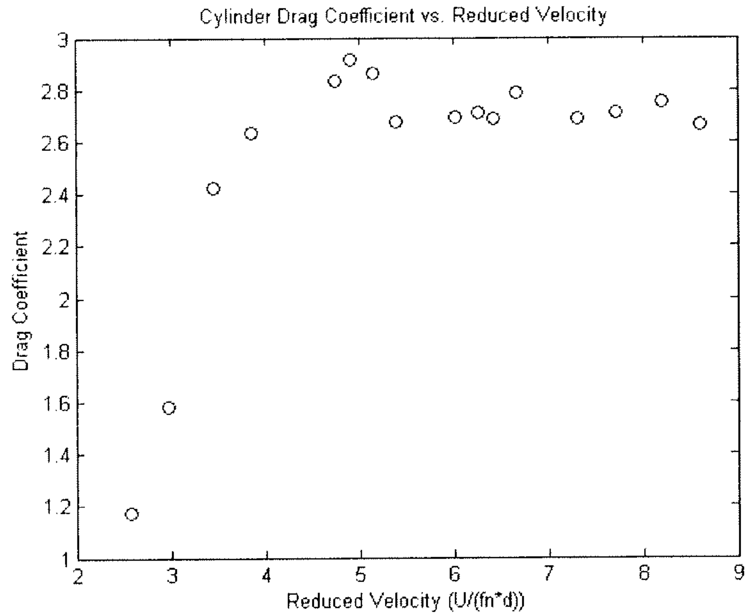

Figure 2-13: Cylinder Cd vs. Vr

Figure 2-14, shown below, is a plot of the cylinder transverse vibration frequency as a function of reduced velocity. The linearity of the graph above reduced velocity 4 indicates that the Strouhal number remains constant (as predicted) during these tests. Below reduced velocity 4, relatively large inline motions (which occur at twice the frequency of transverse motions) dominate cylinder vibrations.

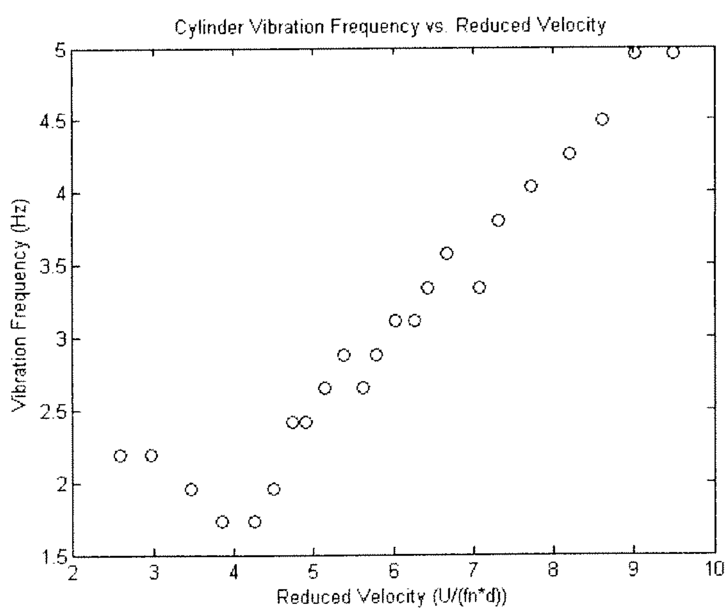

Figure 2-14: Cylinder Vibration Frequency vs. Vr

2.4.2 Configuration 1

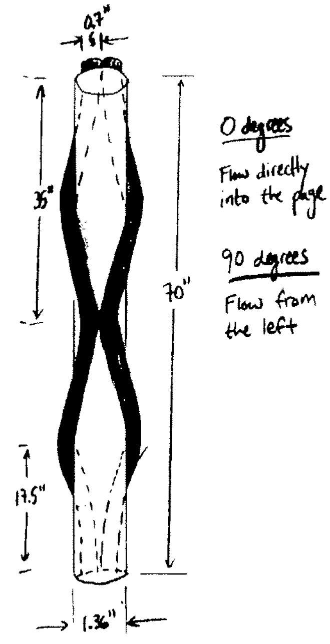

In this configuration, the smaller cylinders lie next to each other at the ends and the middle of the test section, but they lie directly opposite each other at the ¼ and ¾ location.

As is shown seen in Figure 2-15, this configuration yielded large amplitude oscillations. Because the viability of this configuration was ruled out early (due to the large oscillations), repeat experiments were not conducted to determine the drag coefficient.

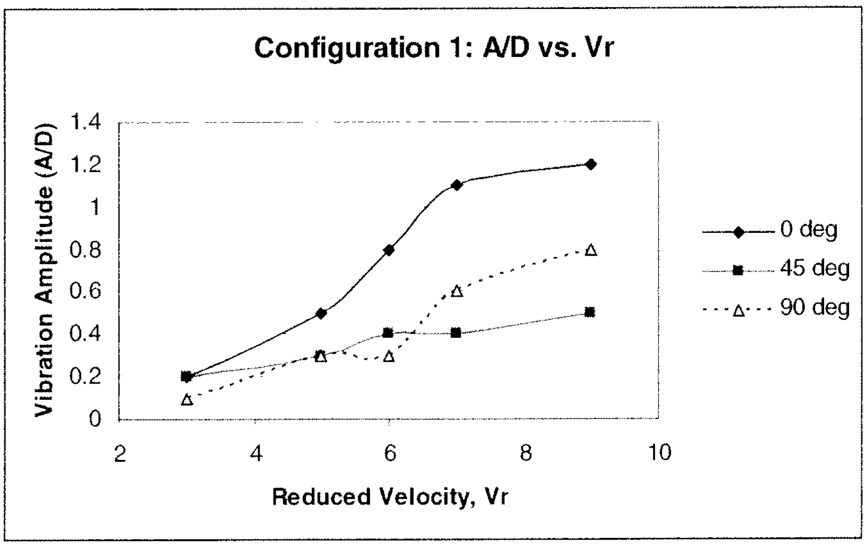

Figure 2-15: Configuration 1 A/D vs. Vr

2.4.3 Configuration 1b

Configuration 1b is similar in shape to Configuration 1, but it holds twice as many twists of the smaller cylinders over the same length. If "pitch ratio" is defined as the length of one full twist divided by the central cylinder diameter, then the pitch ratio of Configuration 1b is 35"/1.36", or 25.7. The pitch ratio of Configuration 1 is then 70"/1.36", or 51.5. The maximum vibration amplitude of Configuration 1 is 1.2 (A/D) and of Configuration 1b is 0.7 (A/D). Hence, it appears that reducing the pitch ratio reduces the vibration amplitude. As is discussed in the closing chapter, further work could be conducted for this shape at a smaller pitch ratio.

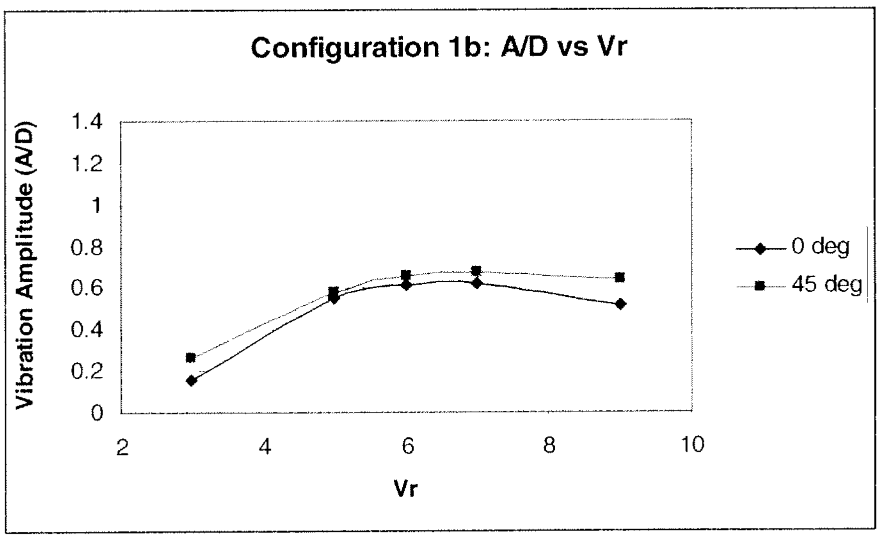

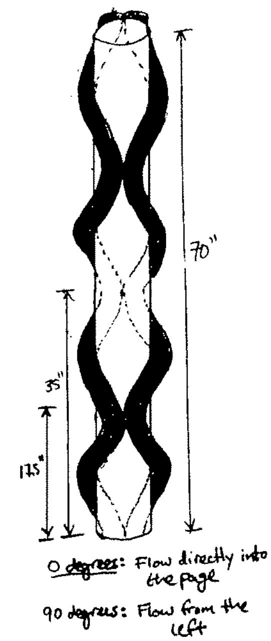

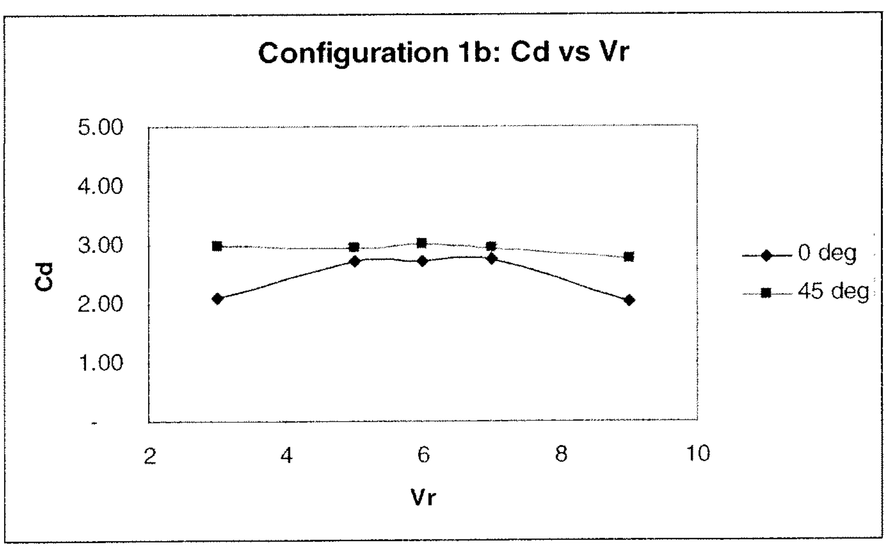

Figure 2-16: Configuration 1b A/D and Cd vs. Vr

2.4.4 Configuration 2

In this configuration the smaller cylinders always lie directly opposite of each other, and they zigzag down the length of the central cylinder. Significantly high vibration amplitudes (and correspondingly high drag coefficients) are observed in this configuration.

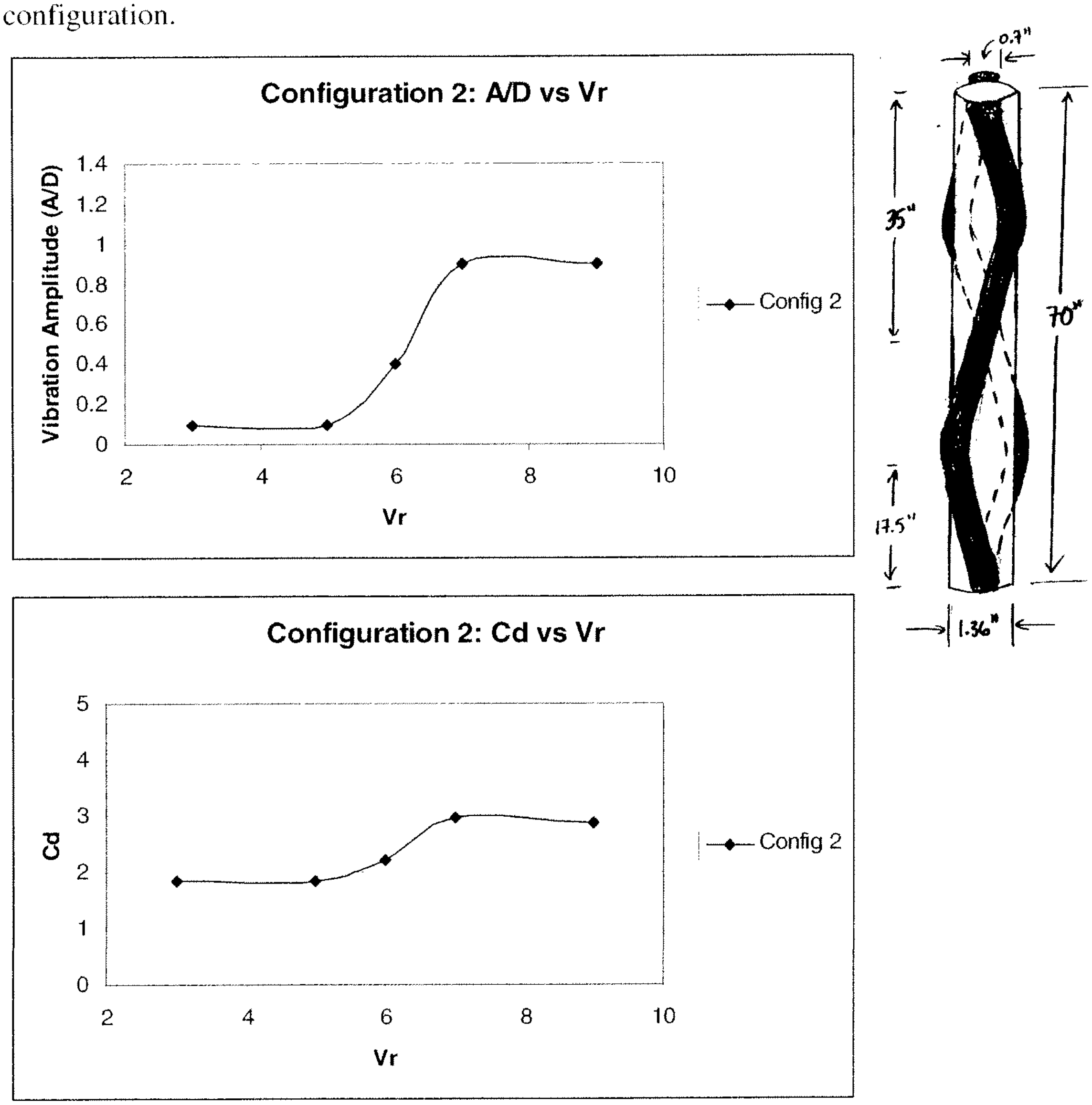

Figure 2-17: Configuration 2 A/D and Cd vs. Vr

2.4.5 Configuration 2a

Configuration 2a is similar in shape to Configuration 2, but twice as many "zigzags" occur down the length. More "zigzags" appear to decrease the vibration amplitude somewhat (~25%), but not significantly enough to show promise of complete VIV suppression.

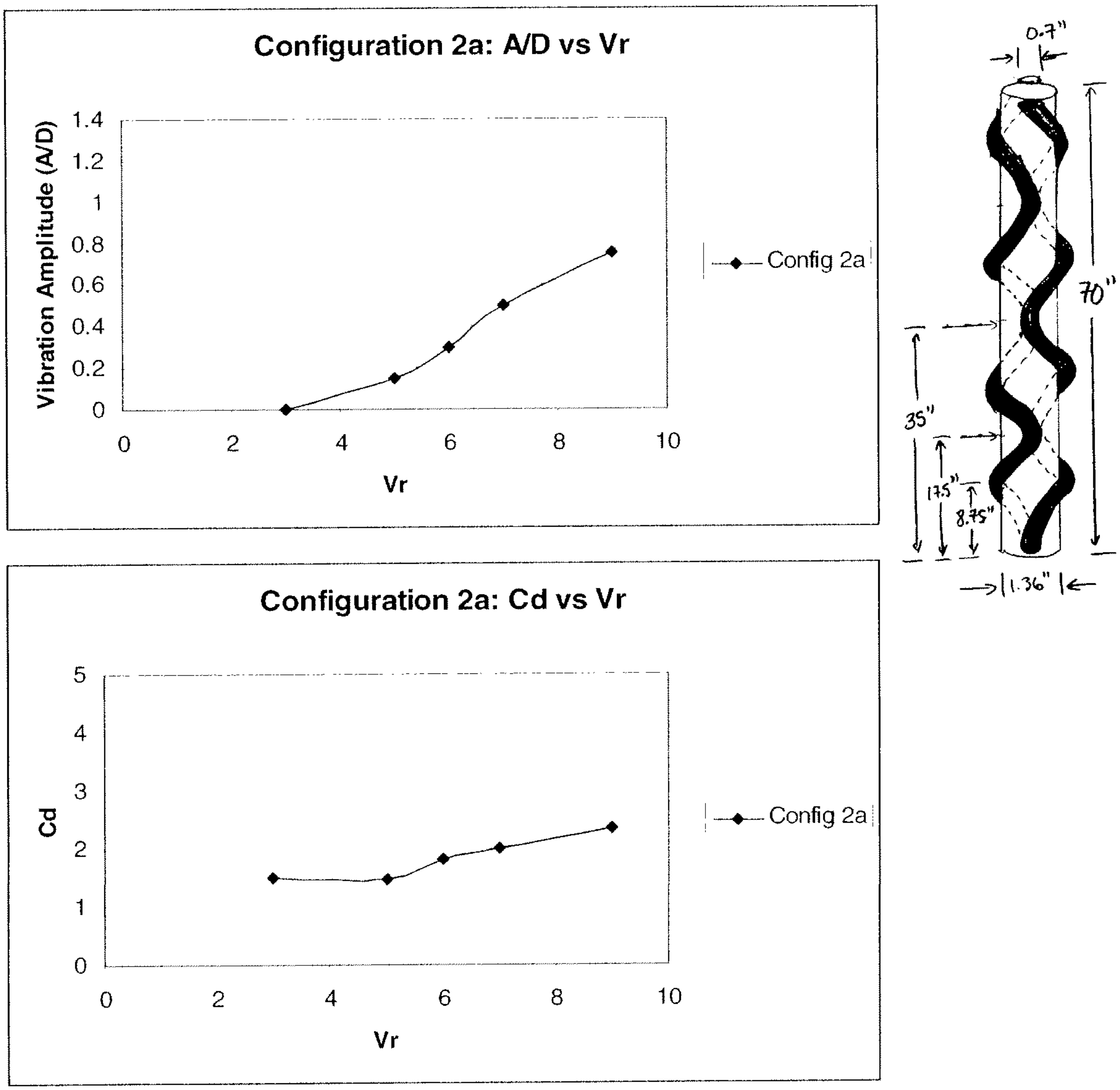

Figure 2-18: Configuration 2a A/D and Cd vs. Vr

2.4.6 Configuration 2d

Configuration 2d has the same number of "zigs and zags" as configuration 2a, but Configuration 2d utilizes three smaller cylinders (instead of two). The three cylinders are equally spaced away from each other around the central cylinder (120 degrees apart). The total angle from "zig to zag" is about 90 degrees. This configuration yields moderate size vibrations (0.6 A/D) and relatively low drag coefficients (less than 2 for most of cases).

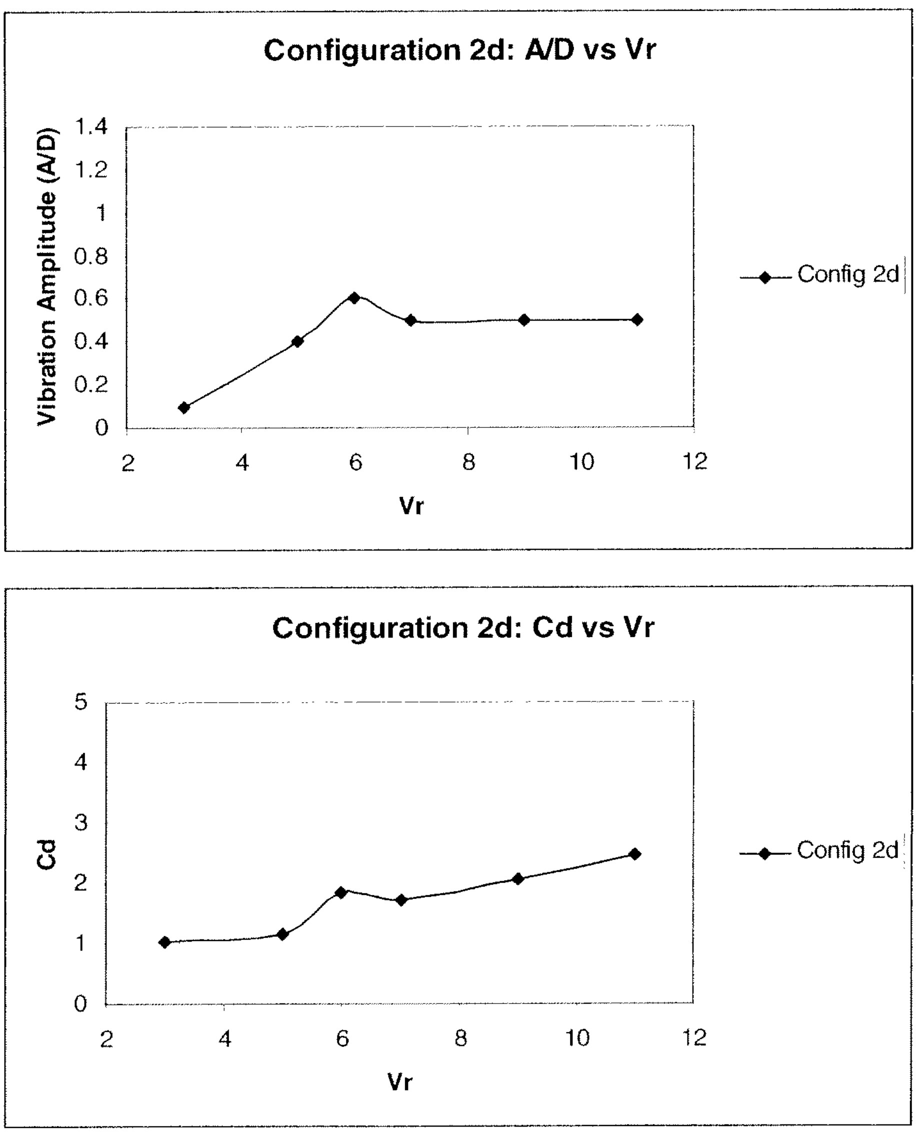

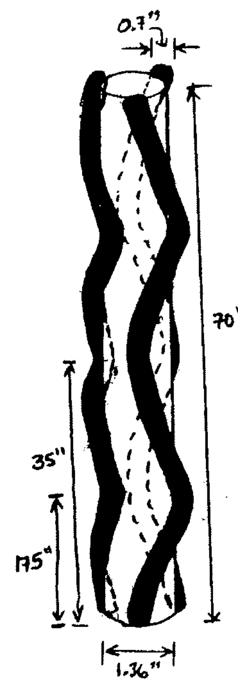

Figure 2-19: Configuration 2d A/D and Cd vs. Vr

2.4.7 Configuration 2s

Configuration 2s is exactly the same as Configuration 2a, but in Configuration 2s, a ¼ inch diameter rope is helically wound around the central cylinder (underneath the smaller cylinders). The ¼ diameter rope is wound tightly around the central cylinder (20 times over the 70" length) so that the small cylinders rest on top of the rope. It is seen that vibrations are suppressed up until Vr equal to 7, and then they jump up to 0.5 A/D.

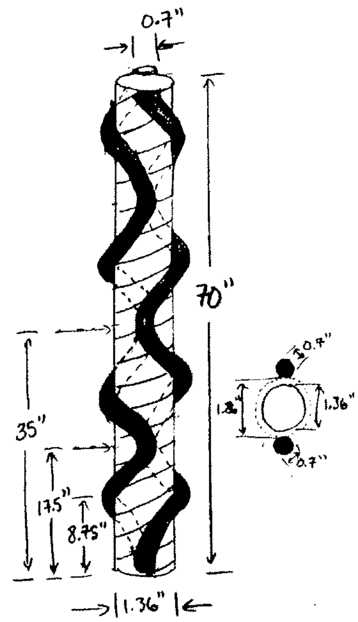

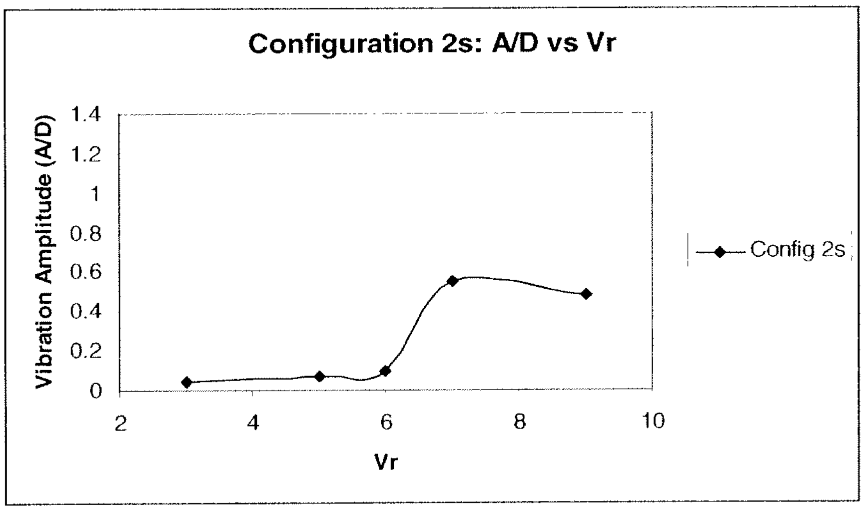

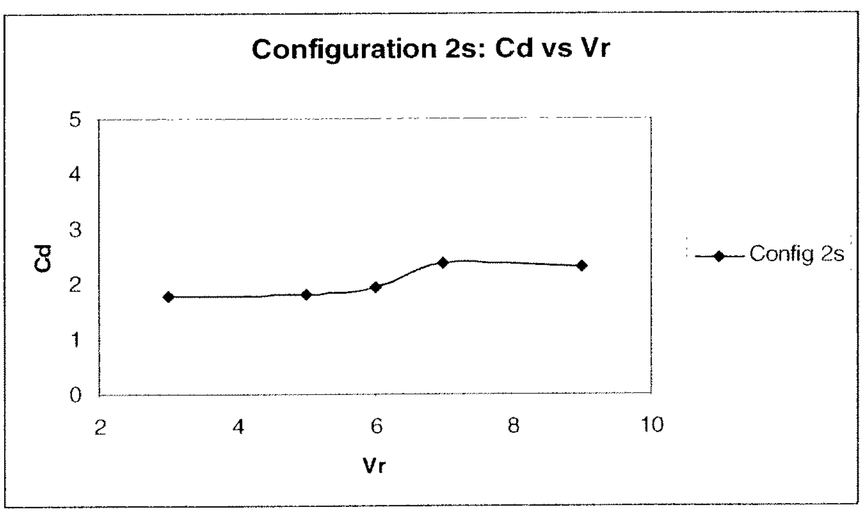

Figure 2-20: Configuration 2s A/D and Cd vs. Vr

2.4.8 Configuration 3

Configuration 3 is a classic example of a "helical strake". This shape is well known to suppress cylinder vibrations, and it does, as shown below, in Figure 2-21. The drag coefficient remains near 2 throughout the range of speeds.

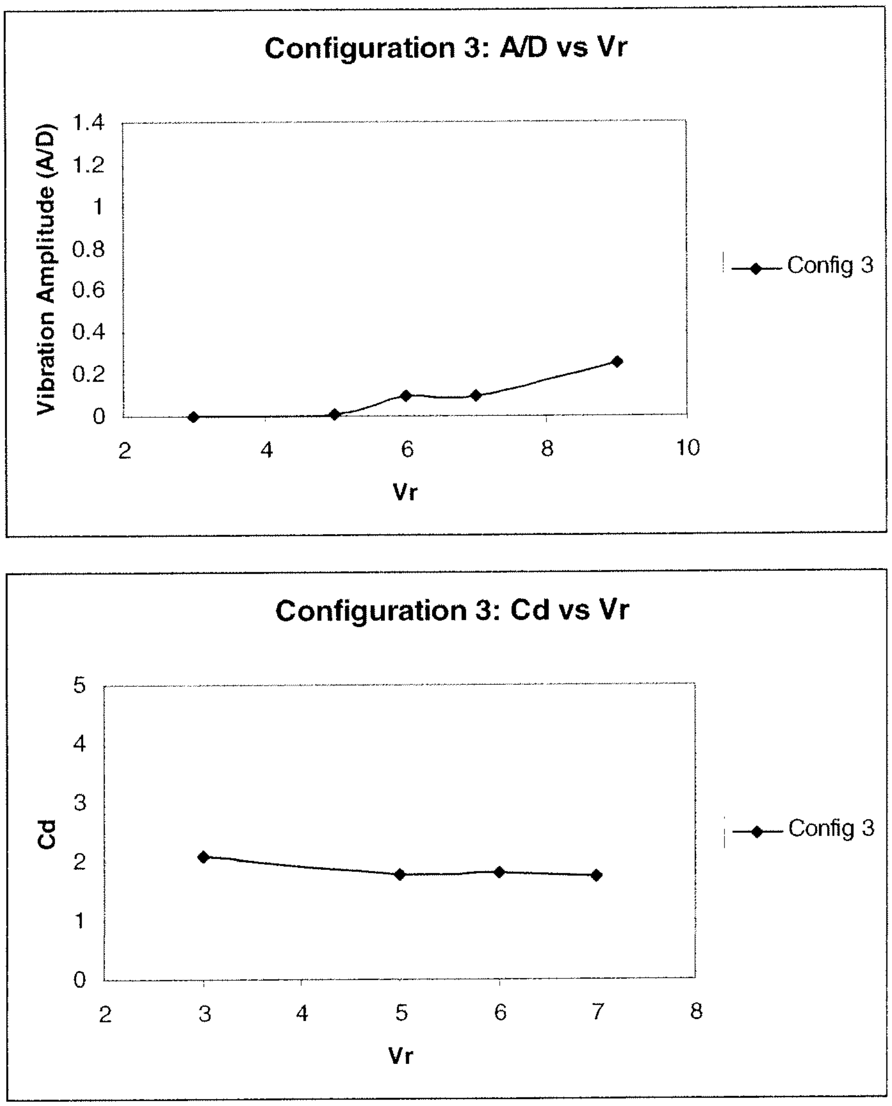

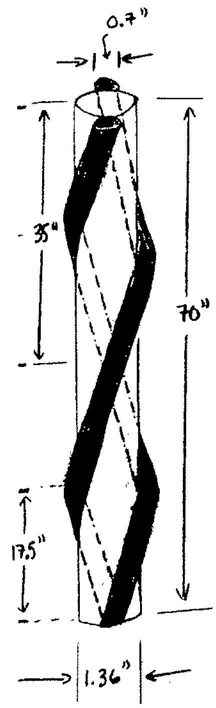

Figure 2-21: Configuration 3 A/D and Cd vs. Vr

2.4.9 Configuration 3f

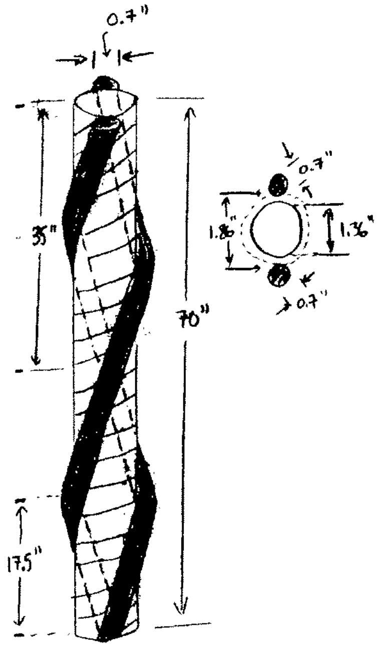

Configuration 3f is a modification on Configuration 3 with the addition of an inner helically wound rope (¼ inch diameter). The helically wound rope revolves completely around the cylinder 20 times over the 70 inch length. Both the rope and the cylinder are wound in the same direction. Configuration 3f suppresses cylinder vibrations even more effectively than Configuration 3. Drag coefficients are about 10% higher, however.

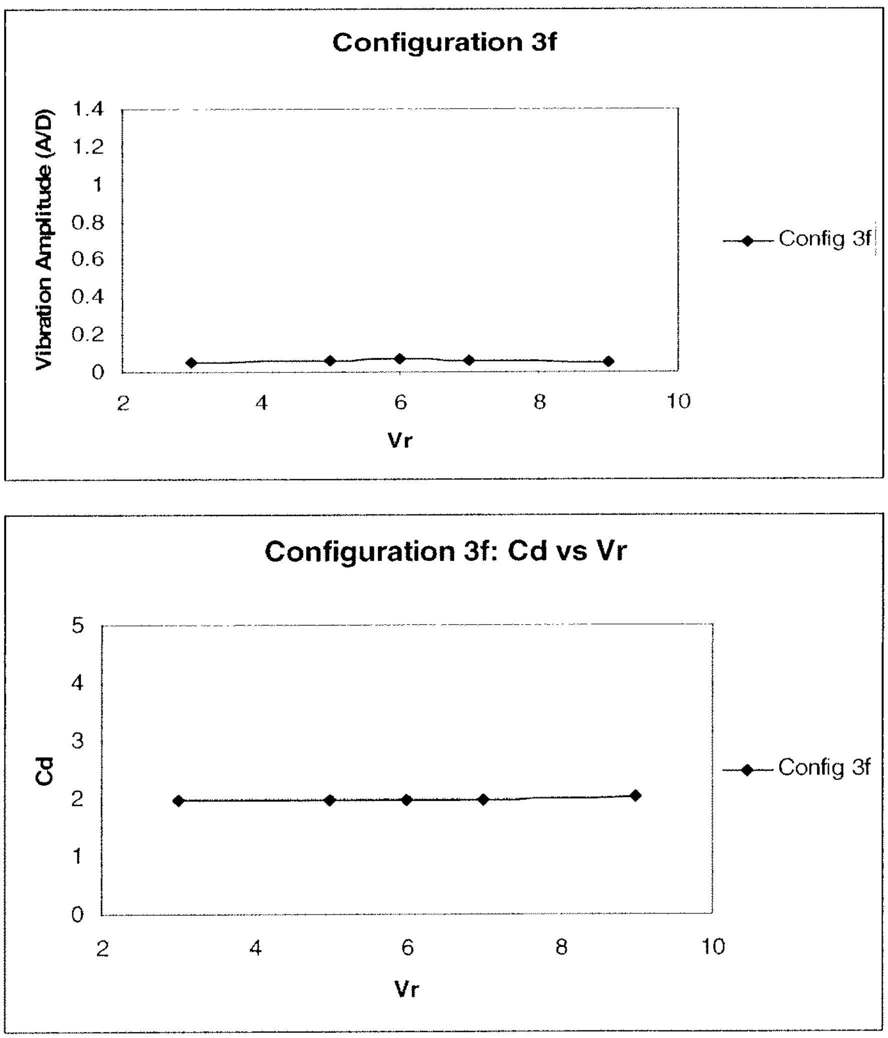

Figure 2-22: Configuration 3f A/D and Cd vs. Vr

2.4.10 Configuration 4

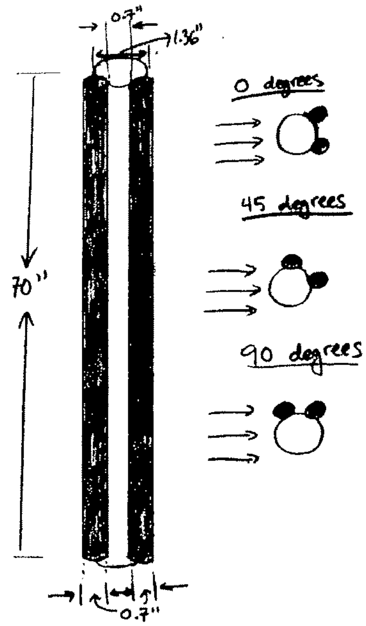

Configuration 4 tests the response of the central cylinder when the smaller cylinders lie straight down the length of the central cylinder. The smaller cylinders in this case are spaced about 90 degrees apart from each other. Significant vibration amplitudes exist in this configuration and the drag coefficients are correspondingly high.

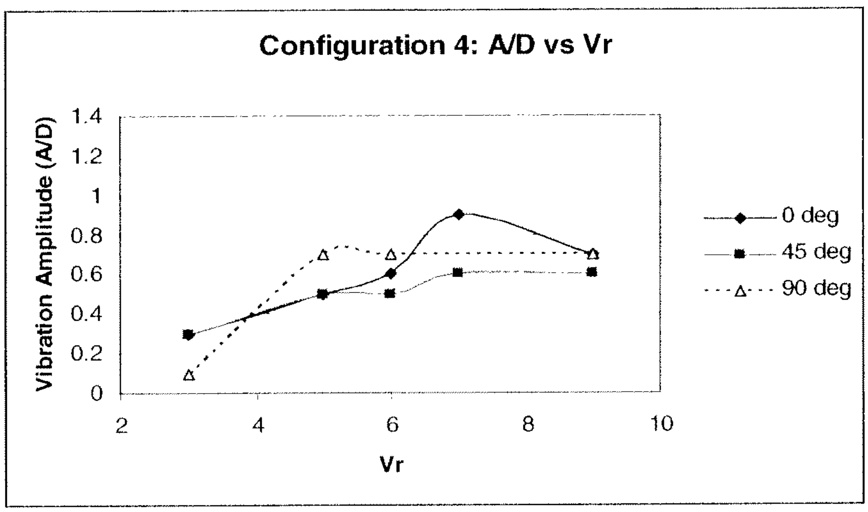

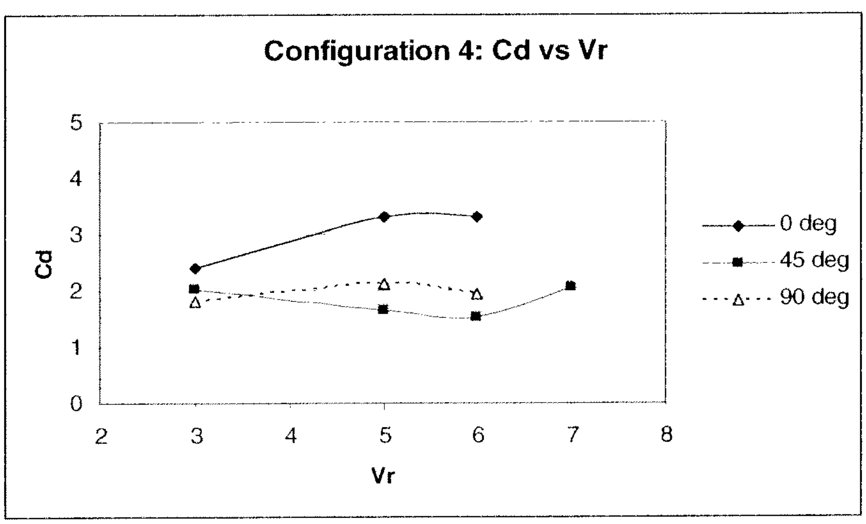

Figure 2-23: Configuration 4 A/D and Cd vs. Vr

2.4.11 Configuration 5

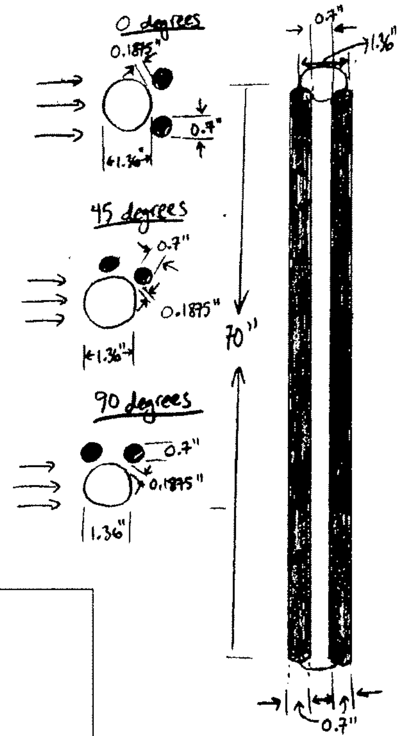

Configuration 5 is the same as configuration 4, except that the smaller cylinders are spaced off of the central cylinder by about 14% of the central cylinder diameter.

For the 0 degree configuration, a sizable decrease in vibration amplitude and drag coefficient is observed when comparing Configuration 5 to Configuration 4. However, Configuration 5 still shows significant vibration amplitudes at 45 and 90 degrees.

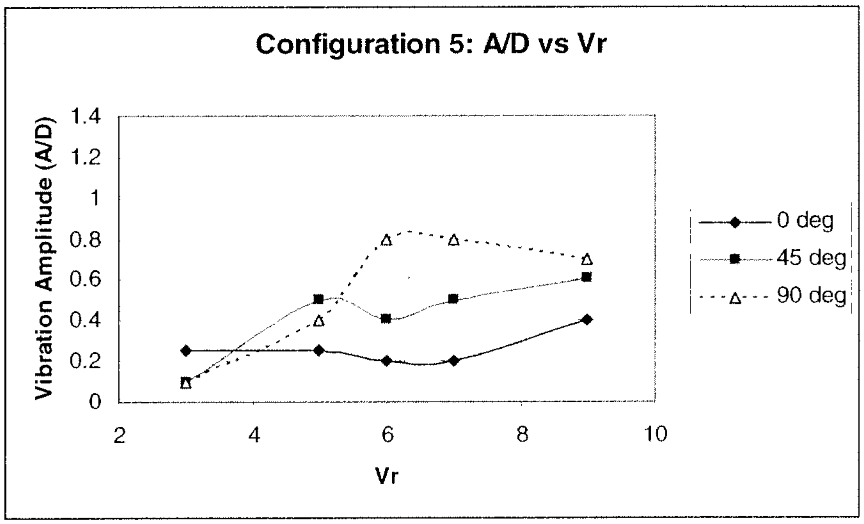

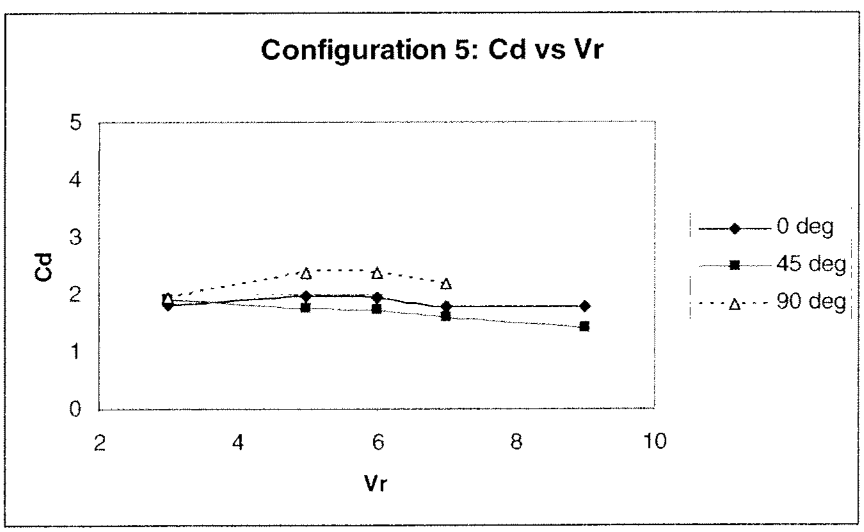

Figure 2-24: Configuration 5 A/D and Cd vs. Vr

2.4.12 Configuration 5e

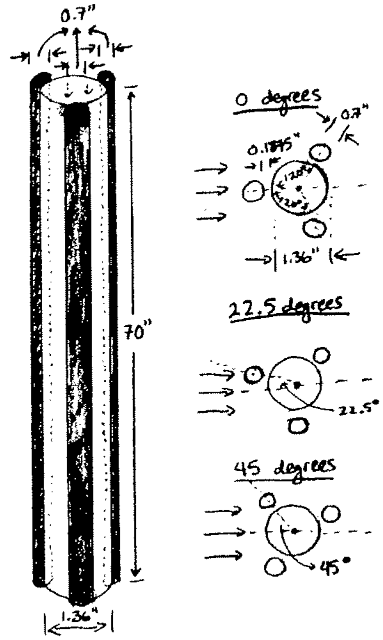

Configuration 5e is similar to Configuration 5, except that three small cylinders are utilized (spaced 120 degrees apart from each other), instead of two. The vibration amplitude data was lost for the zero degree case, but the significantly high vibration amplitudes for 45 and 90 degrees, and the high drag coefficients for all cases (well over 2) indicate that this configuration does not successfully suppress VIV.

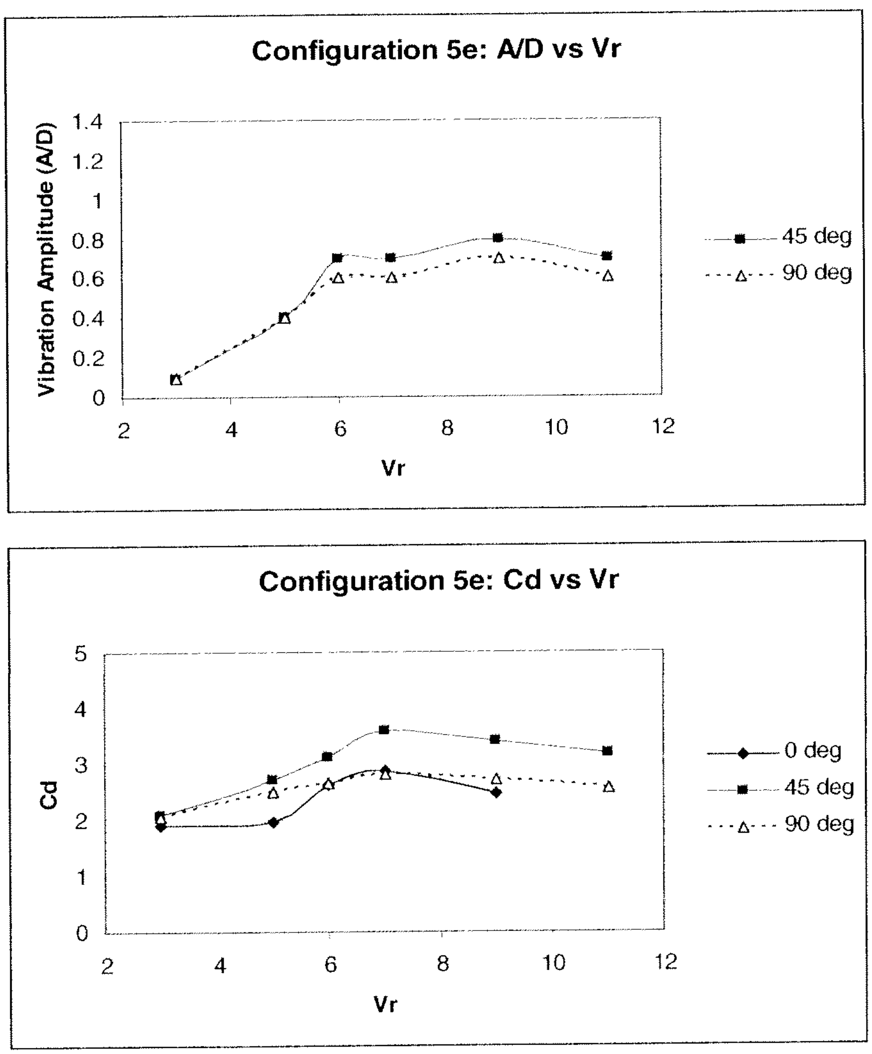

Figure 2-25: Configuration 5e A/D and Cd vs. Vr

2.4.13 Configuration 5g

Configuration 5g is similar to Configuration 5, except that a ¼" diameter helically wound rope spirals down the length of the cylinder. The vibration amplitudes remain small for the 0 and 45 degree cases (< 0.4 A/D), but they become large for the 90 degree case (0.8 A/D). Also notice that the drag coefficient remains below 2.0 for the 0 and 45 degree case, but then increases to over 4 for the 90 degree case.

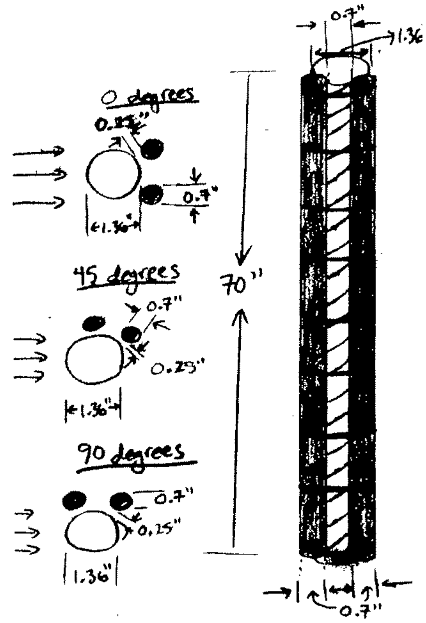

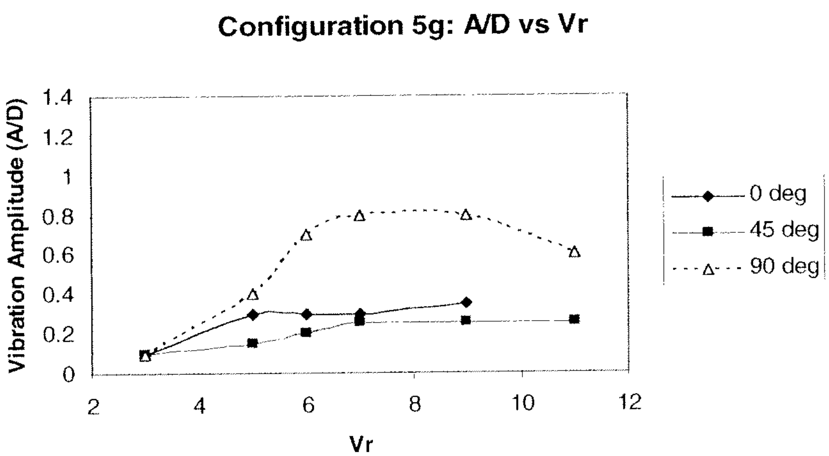

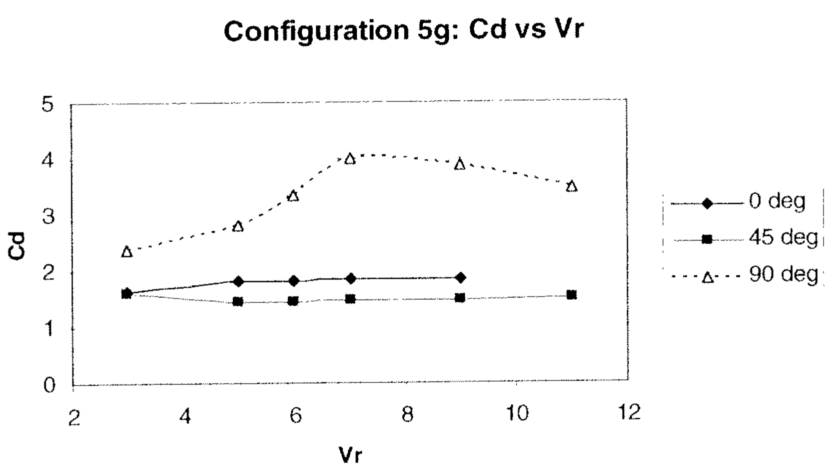

Figure 2-26: Configuration 5g A/D and Cd vs. Vr

2.4.14 Configuration 5j

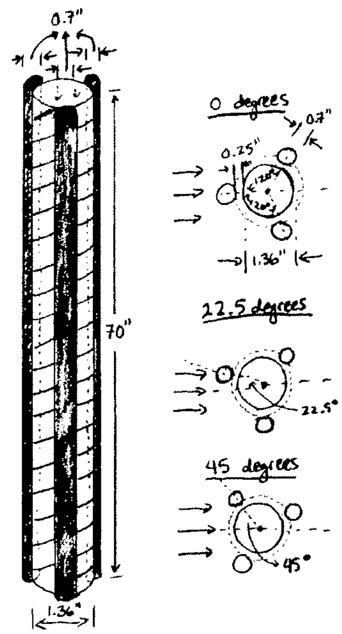

Configuration 5j is similar to Configuration 5e, except that a ¼" diameter helically wound rope spirals down the length of the cylinder (instead of a 0.1875" spacing of each of the three small cylinders off of the central cylinder). Vibration amplitude and drag are surprisingly low (0.1 A/D, and 2.0 Cd) for the 0 degree case, but they rise quickly (0.9 A/D and 4.6 Cd) for the 45 degree case.

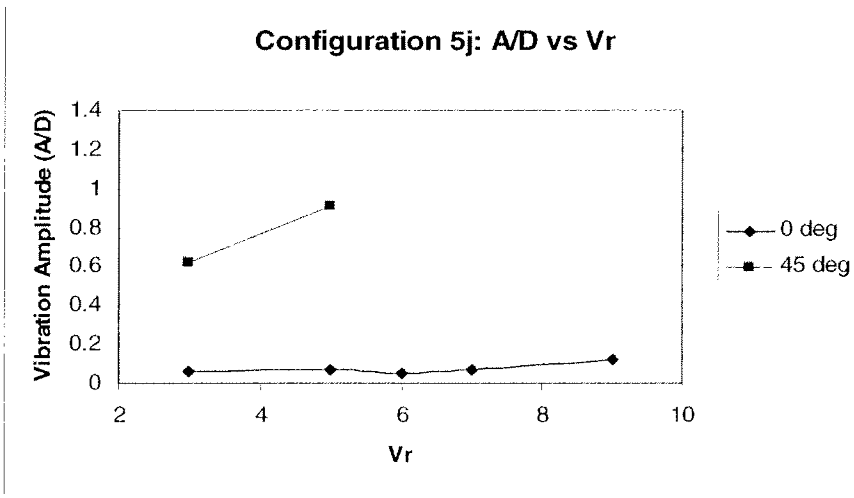

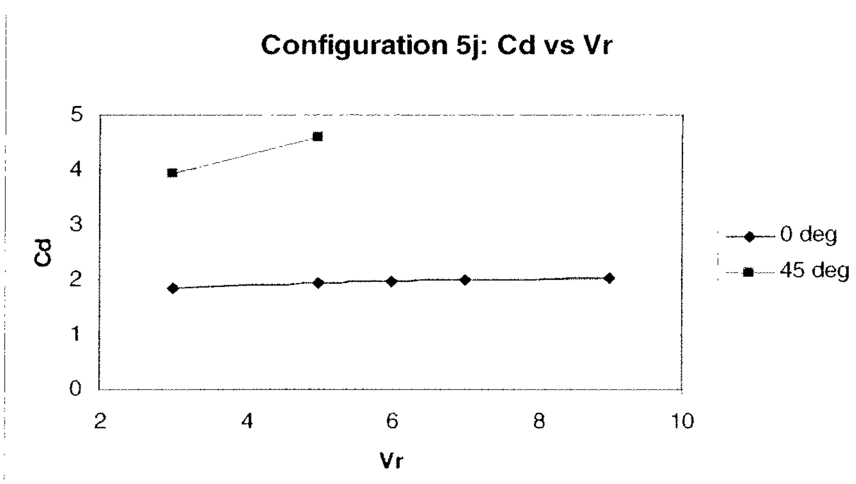

Figure 2-27: Configuration 5j A/D and Cd vs. Vr

2.4.15 Elliptical Cross-Section Spiral

This configuration is the elliptical cross-section spiral discussed in Section 1.4. The ratio of major axis diameter to minor axis diameter of the ellipse is approximately 1.25. Shown below is the vibration amplitude over a densely populated range of reduced velocities. The major axis diameter was used to define A/D for this graph (the A/D ratio would be even larger if the minor axis diameter was used). Note that the amplitude of the elliptical cross-section spiral is larger than the amplitude of the bare cylinder tests (configuration 0).

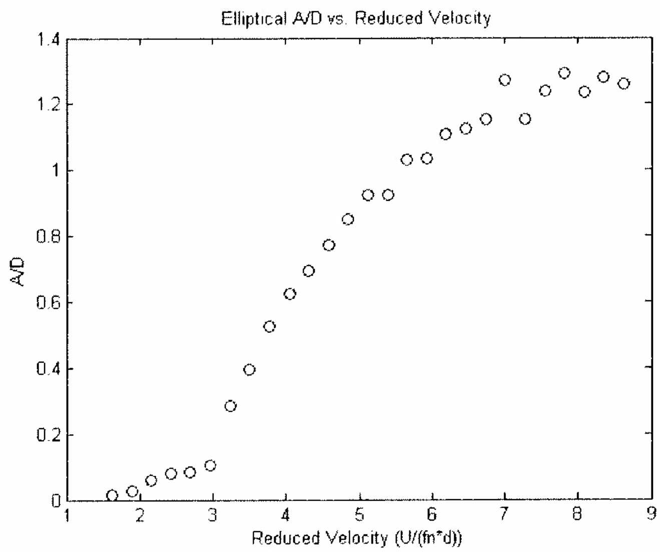

Figure 2-28: Elliptical A/D vs. Vr

Shown to the right is the vibration frequency as a function of reduced velocity. The linearity of this graph indicates that the Strouhal number remains constant during these tests. No drag force data was recorded.

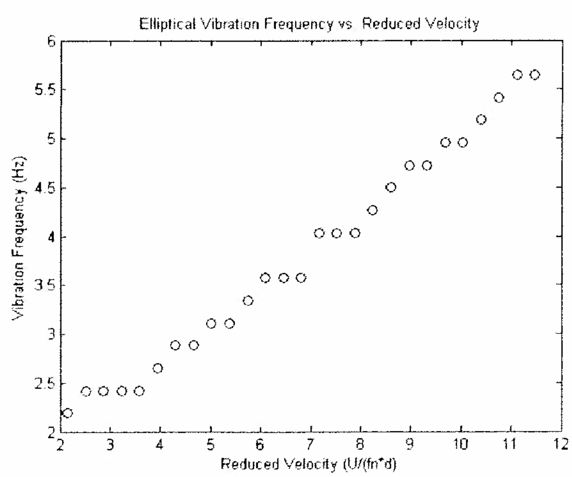

Figure 2-29: Elliptical Vibration Frequency vs. Vr

2.5 Comparison Chart

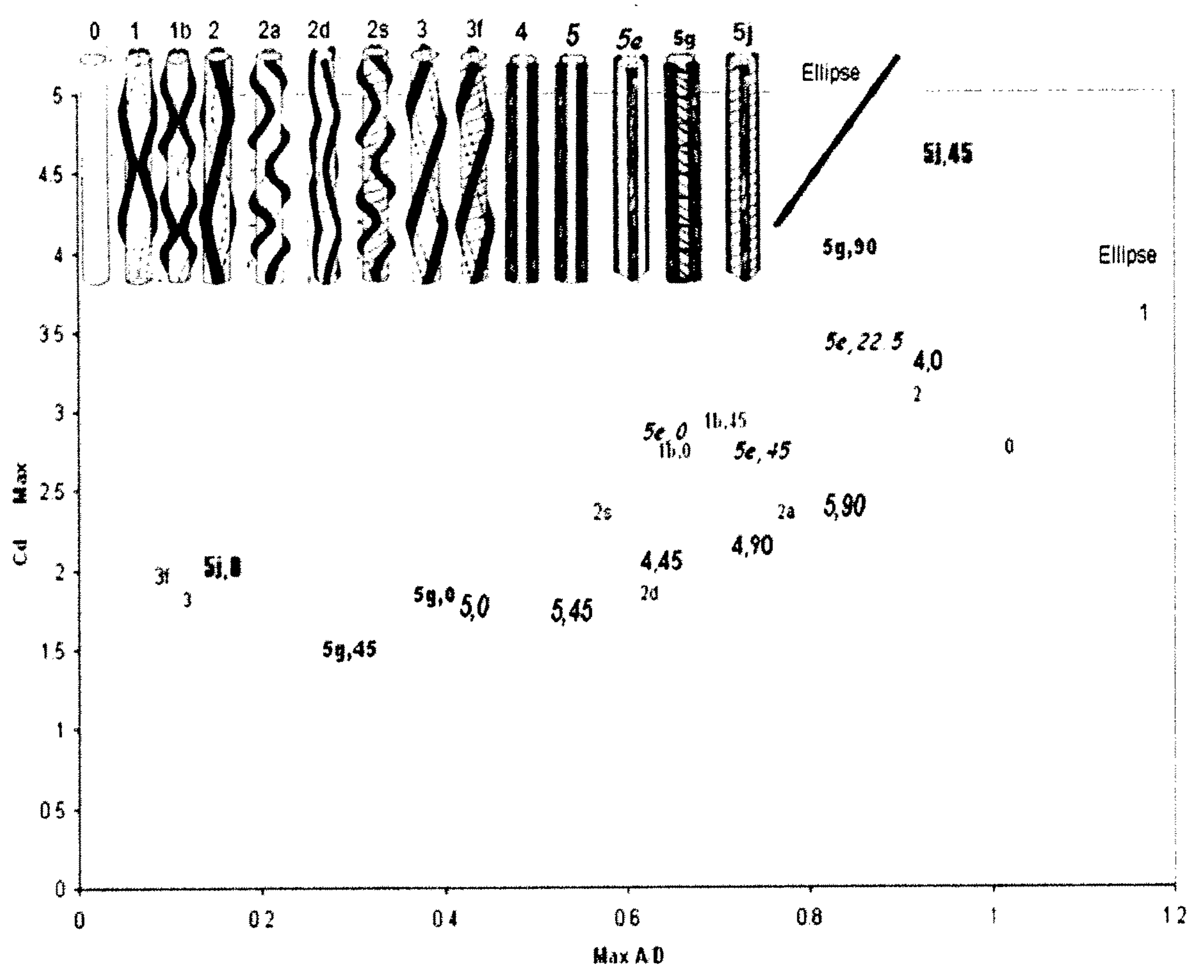

Figure 2-30: Flexible Cylinder Experiments Comparison Chart

Figure 2-30 is an attempt to display the most important data from this chapter onto one chart. Keeping with good engineering practice, the "worst case" Cd and A/D measurement is chosen to represent each configuration on this graph. The best configurations are closest to the bottom left corner (minimum Cd and A/D) of the graph, and the worst performing configurations are near the upper right (maximum Cd and A/D).

Testing configurations that have been tested at only one angle with respect to the flow (for the most part these are the "omnidirectional" orientations) are identified with black,

plain lettering. Colored fonts signify "unidirectional" configurations (and two or three angles are tested). Whenever a test configuration is unidirectional, the configuration reference contains a comma (i.e. 5e,0 or 4,45) to indicate the direction of testing. Only vibration data (i.e. no drag data) is available for Configuration 1 and the elliptical cross-section, so a "best guess" of drag coefficient is made in order to include these tests on the chart. Due to their high vibration amplitude, these two cases are furthest to the right on the chart, and thus precise drag measurements do not seem of vital importance.

2.6 Summary

The diversity of the flexible cylinder tests yielded a wide range of results. Configurations 1, 1b, 2, 2a, 2d, 2s, and 4 did not show potential towards suppressing VIV because all of these tests oscillated larger than 0.5 A/D; and it is interesting to note that with the exception of Configuration 2s, all of the configurations mentioned above had the small cylinders directly attached to the central cylinder (with no spacing). This suggests that spacing the small cylinders away from the central cylinder is important in suppressing VIV. However, it is also important to note that the small cylinders in Configuration 3 (the classic "helical strake" configuration) *were* directly attached to the central cylinder, but even so only small oscillations were measured.

The best configurations tested (those with a maximum amplitude of less than 0.5 A/D) include 3f, 3, 5j(0), 5g(45), 5g(0), and 5(0). These six configurations are shown below in Figure 2-31.

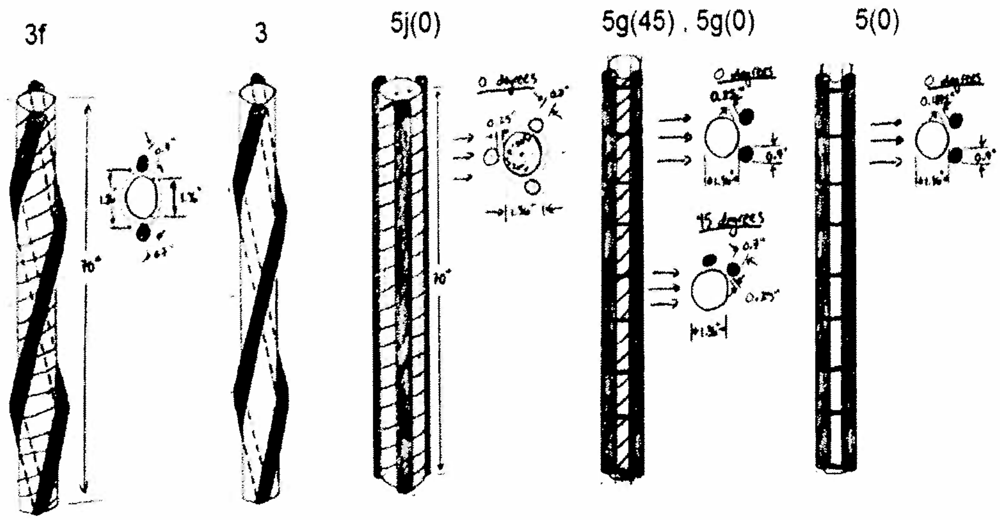

Figure 2-31: Flexible Cylinder "Best Orientations" Picture

Three trends exist in these configurations. First, and most obvious, is that a helical winding works well in suppressing vibrations. Second, smaller cylinders most successfully suppress vibrations if they are spaced off of the central cylinder (to allow flow to pass between the small cylinders and the central cylinder).

Third, the small cylinders perform best when they are located on the downstream portion of the central cylinder near the point of flow separation/vortex formation (shown in Figure 2-32; usually about 60 degrees above/below the rear stagnation point). Based upon the 5g(45) case, this even appears to hold true when only one of the small cylinders is near the flow separation/vortex formation point.

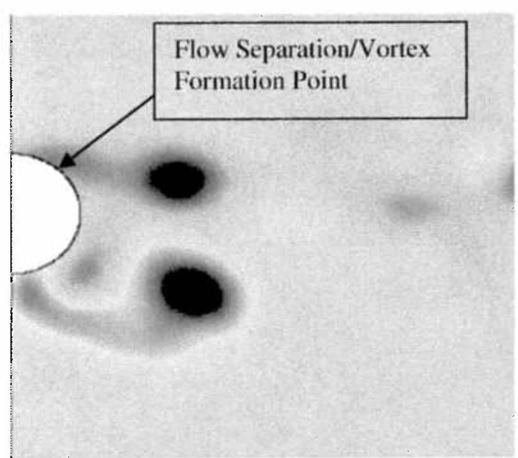

Figure 2-32: Flow Separation Picture

The small cylinders can be thought of as "near-wake stabilizers" (discussed in 1.4), when they are located on the downstream portion of the central cylinder. In the following chapter, additional work with near-wake stabilizers is completed, and flow visualization

(in addition to force measurement) is incorporated when analyzing the performance of each configuration.

Chapter 3

Rigid Cylinder, PIV Experiments

3.1 Introduction to Particle Image Velocimetry (PIV)

Particle Image Velocimetry, or PIV, is a technique commonly used to visualize two-dimensional fluid flow patterns. The basic idea is as follows: First, the fluid flow is "seeded" with tiny particles that have nearly the same density as the fluid and are assumed to move with the same velocity as the fluid. Next, a high powered laser illuminates a "sheet" of laser light in the two-dimensional plane of interest. Finally, a high-speed video camera (stationed perpendicular to the plane of interest) captures images of the illuminated particles as they move within the sheet of laser light.

The images from the camera are then transferred to a computer which carries out the basic data processing steps: First, the camera images are divided into square grids—each small square of which contains several illuminated particles. Then the cross-correlation of the light intensity in successive images is calculated for each small square. Next, the magnitude and direction of the cross-correlation shift is used, along with the elapsed time between camera images, to determine an average velocity vector for each square. Note that the velocity vector is averaged over both the area of the square and the time elapsed between each image pair. In this way, a velocity vector field is created over the entire camera image and is updated at the camera speed rate. Figure 3-1 shows one instance of a velocity vector field in the wake behind a cylinder. Flow is from bottom to top. Notice that both the magnitude and the direction of the flow are displayed for each square.

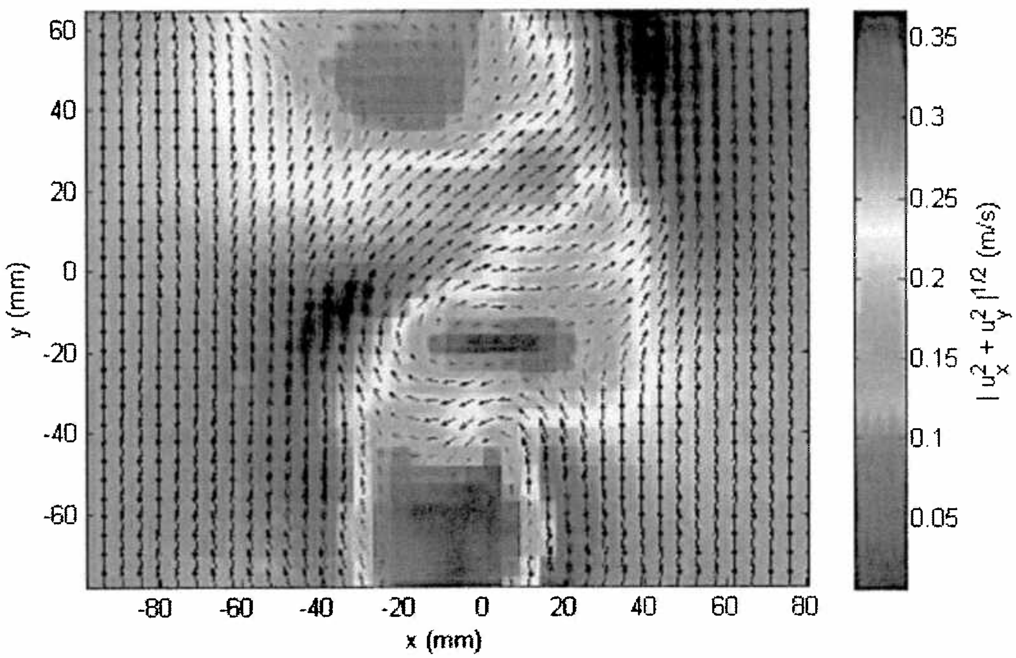

Figure 3-1: Velocity Vector Field Example

The assumption is made that the particles do not move into or out of the plane of the laser light sheets during these tests. If particles were to move in/out of the plane of the laser sheet, then the cross-correlation of light intensity between successive camera images would not be an effective method to measure flow velocity—because correlation would not exist between successive frames. Thus, in the case of the experiments in this chapter and other PIV experiments, care is taken to ensure that the flow phenomena observed is two-dimensional in nature. PIV systems capable of measuring three-dimensional velocities do exist, but they are not discussed in this report.

Of particular interest to the experiments of this chapter is the calculation and visualization of the vorticity field—because it is the development of regular vortex shedding into the wake of an object (not steady portion of the velocity field) that is the cause of VIV. The equation for vorticity, ω, is defined as the curl of the velocity vector V, and is shown here.

$$\vec{\omega} = \vec{\nabla} \times \vec{V} \tag{3.1}$$

Using this equation, the velocity vector field is used to calculate the vorticity field as it changes between each set of camera images. A "movie" of the vorticity field changing over time can then be displayed by playing successive camera images. From the standpoint of the design of VIV suppression devices—a visual tool such as this movie is invaluable because it gives the engineer a visual picture and thus a more intuitive sense of the problem at hand.

3.2 Motivation

This chapter details the results of tests conducted with a rigid cylinder, vertically-mounted above a tank of water, and pulled along the length of the tank. Forces on the cylinder are measured, and PIV images are recorded of the cylinder wake. In most of the tests, near wake stabilizers are added to the cylinder in an effort to disrupt vortex shedding and reduce the cylinder drag force.

Particular to this set of tests, it is hypothesized that if the flow field around a cylinder were able to resemble the "potential flow" field (shown below), then drag force and vortex shedding would both be minimized. Thus, the goal of these tests is to force the flow to resemble the potential flow picture (shown in Figure 3-2).

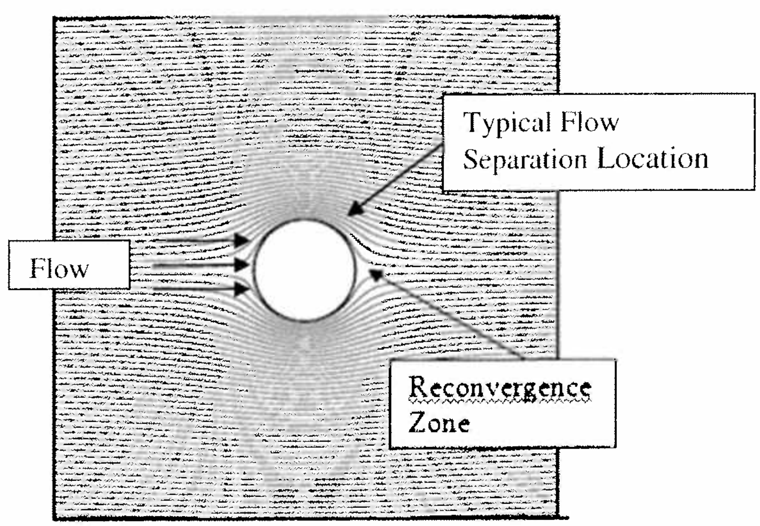

Figure 3-2: Streamlines of "Potential Flow" around a Cylinder

It is hypothesized that a pair of airfoil shapes will be able to effectively "steer" the flow into looking like the potential flow picture by pushing the flow back towards the cylinder where the flow would typically separate.

Furthermore, it is suspected that a triangle shape, positioned at the rear of the cylinder, will help the wake reconverge behind the cylinder. Similar experiments have been attempted before in other laboratories with airfoils, and with triangles, but not simultaneously.

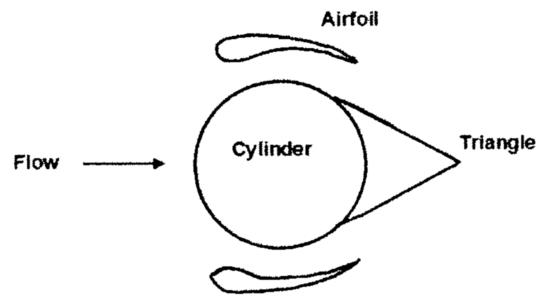

Figure 3-3: Cylinder w/ Triangle and Airfoil Pair

3.3 Previous Work

3.3.1 Cylinder with Triangle

Figure 3-4, shown below, is a helpful chart taken from Fluid Dynamic Drag (Hoerner, 1992). The chart displays the drag coefficient (as a function of Reynolds number regime) for a cylinder with different size triangle shapes attached to the downstream portion of the cylinder.

The PIV tests conducted in this report are all with Reynolds number below 10,000 (an order of magnitude below the "critical" Reynolds number regime) so the first column of drag coefficients (in the chart below) is a direct comparison.

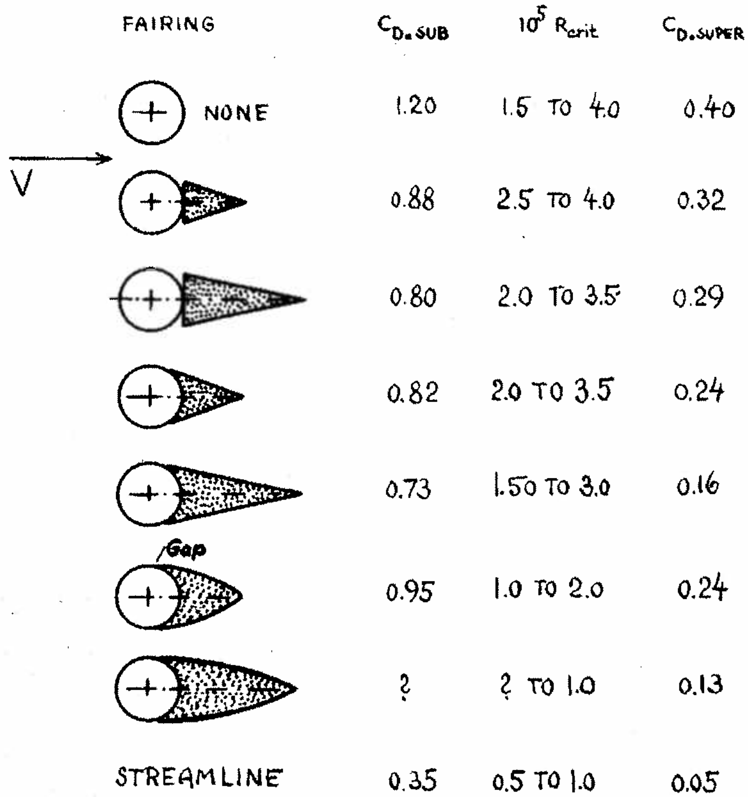

Figure 3-4: Drag Coefficient of Triangle Shapes vs. Reynolds Number Regime (Hoerner, 1992)

As is shown in the figure, the coefficient of drag decreases substantially for a cylinder with a triangle (when compared to a cylinder without a triangle). It also appears that a triangle ~2 diameters in length has a smaller drag coefficient than a triangle only ~1 diameter in length. However, one should always keep in mind that a distinct preference towards a smaller triangle would be given in the implementation of a full scale system (due to manufacturing cost, ease of deployment, storage volume, etc.)

3.3.2 Cylinder with Rigid Guide Vanes

Over sixty years ago, tests were conducted with "rigid guide vanes" attached to a cylinder by Grimminger (1945) in the David Taylor Model Basin. Similar to the testing completed in this thesis chapter, a cylinder was mounted vertically, towed along the length of a tank, and the forces on the cylinder measured. "Rigid guide vanes" (as they

were called back then) look similar to airfoils. Shown in Figure 3-5 is a graph of the results of the rigid guide vane experiments. Although Cd values are not displayed on the graph, one can calculate the Cd values knowing that the cylinder diameter was 2.38 cm, and the length of cylinder was 60.96 cm. The best guide vane (shown below as configuration "D") has a Cd in the range of 0.5 – 0.7 over its series of test speeds.

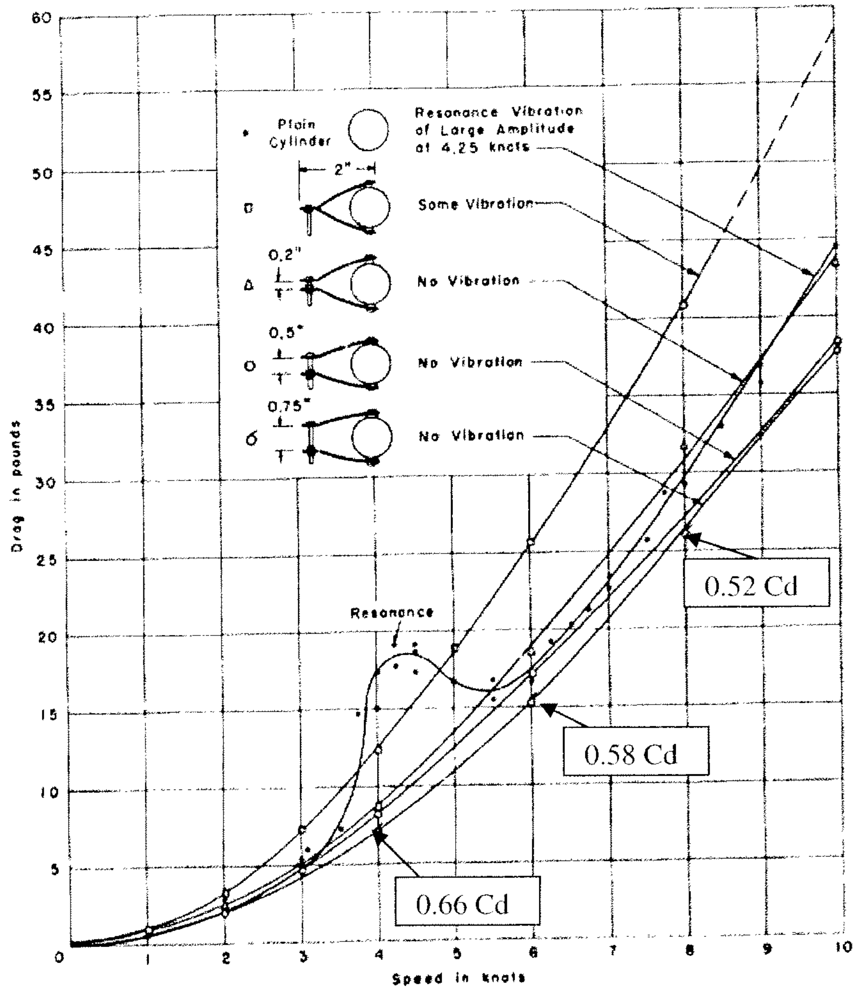

Figure 3-5: The Effect of Rigid Guide Vanes on Drag of Towed Cylinder (Grimminger, 1945)

Clearly, guide vanes successfully reduce the drag coefficient of a cylinder, and a triangle (as discussed in 3.3.1) does as well. This bulk of the remainder of this chapter explores a combination of these two techniques in an attempt to reduce the drag coefficient even further. This chapter also contributes vorticity images and movies that help with understanding the vortex shedding phenomenon.

3.4 Apparatus

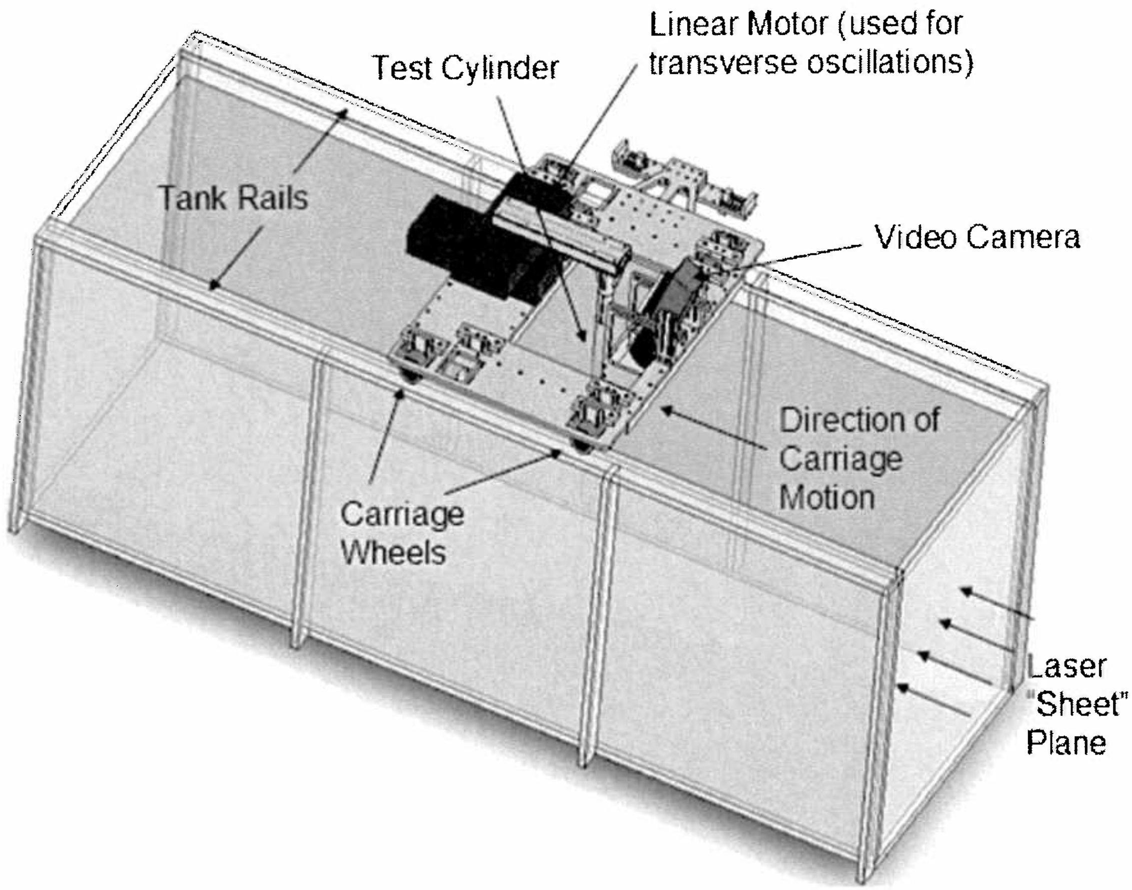

Figure 3-6: Rigid Cylinder, PIV Experiments Apparatus

Figure 3-6 shows a computer image of the testing apparatus. The test cylinder is connected via a rectangular bar to a linear motor (which provides the transverse oscillations). The video camera follows behind the cylinder and records high-speed images of the particles illuminated in the wake. Not shown in this picture is the motor, belt, and pulley system that moves the carriage along the tank rails.

Here are some specifics about the equipment used for the tests. The flow seeding particles used were 61-133 μm in size with an average size of 93 μm. The density of these particles was 1.01 g/cm^3. The laser was a Quantronix Darwin 527 Series Diode Pumped Q-Switched Second Harmonic Nd: YLF Laser. The high-speed camera was a

LaVision Imager Pro and took images near 500 Hz. The cylinder diameter was 0.0381 m, and the submerged length was 0.6858 m.

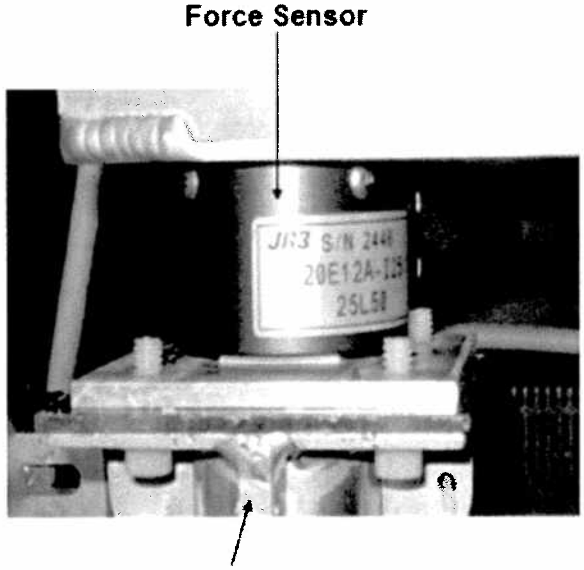

Figure 3-7: JR3 Six-Axis Force Sensor

The forces were measured using a JR3 six-axis force sensor (shown above in Figure 3-7). Because the force sensor was mounted onto only one end of the cylinder (making a "cantilever beam"), the measured moments on the cylinder were often quite large in comparison to the measured forces (i.e. the drag and lift forces). Also, due to the small cylinder diameter (3.81 cm) and slow towing speed (0.25 m/s), the expected drag force was often very small (less than one Newton of force for Cd equal to 1.2). Additionally, the calibration provided by the manufacturer only included calibration weights of 0, 5, 10, 15, 20, and 25 lbs—with no information for small forces less than 5 lbs.

Using the calibration matrix provided by the manufacturer, a drag coefficient of 0.9 was measured for the bare cylinder (towed without transverse oscillations)—a departure from the 1.2 value nominally accepted for a cylinder without oscillations. Thus, it was decided to recalibrate the sensor in-situ, with calibration forces/moments on the same order of magnitude as those expected during a test.

The following procedure was used for the in-situ calibration: known combinations of "forces" (100 g, 200 g, 500 g, and 1 kg), were applied at two separate locations along the cylinder length, and at two different radial orientations. Also, a concentric weight was hung from the cylinder to excite a longitudinal force, and several "yaw" torques were also imposed (roll, pitch, and yaw are defined in this section as if the cylinder were a ship traveling down the length of the tank). Each imposed force/moment orientation was then placed into a force matrix, F, corresponding to its measured voltage matrix, V. A total of fifty-two force/moment orientations were completed. The calibration matrix, C, was calculated in MATLAB using the following equation:

$$C_{6x6} = F_{6x52} \cdot pinv(V_{6x52}) \tag{3.2}$$

where pinv is the "pseudo-inverse" (a pseudo-inverse is required here because V_{6x52} is not a square matrix). Shown below are both the factory, and the in-situ calibration matrices:

Factory (Metric)

13.06881	-0.31805	-0.07428	-0.97193	-0.2322	1.015969
0.21129	13.13287	-0.27179	0.215293	-1.56354	0.766425
0.517326	-0.004	25.55713	0.848717	-0.59917	-1.07024
0.011843	-0.00648	0.019498	0.659257	-0.00114	-0.01681
-0.00019	-0.00119	-0.01477	0.000316	0.687967	0.009292
-0.00823	-0.00138	0.0105	0.003229	0.010003	0.682243

Calculated, C (Metric)

13.06211	-0.19584	-0.14964	-0.98105	-0.22448	1.622657
0.549133	12.15885	-0.23569	0.49923	-1.3349	0.517279
0.766554	-0.59168	25.54285	1.040719	-0.42701	-0.76962
-0.41682	1.22711	-0.06116	0.29836	-0.2898	0.314201
0.001088	-0.04286	-0.03663	0.003734	0.688479	-0.15912
-0.01001	-0.01059	0.011597	0.002841	0.008061	0.617572

Table 3-1: Force Sensor Calibration Matrices

Use of this calculated calibration, C, yielded a drag coefficient of 1.19 for a bare cylinder (nominally equal to 1.2 for this Reynolds number), so initially it was assumed that this calibration was correct. However, since the original calibration (described above) was completed, further calibration testing (not in-situ) was completed that indicated that forces applied at different lengths down the cylinder did not always yield the expected

voltage output. As a check of the two calibration matrices, the fifty-two force/moment orientations described above were used to determine the percent error between the actual force/moment applied, and the force/moment voltage output (after the force/moment voltage output has been multiplied by the respective calibration matrix). The equation for percent error is shown below:

$$\%error = \frac{C_{6x6} \cdot (V_i) - F_i}{F_i} \tag{3.3}$$

where i represents the forces/moments from one loading orientation. The standard deviation of the percent error for each sensor axis was then calculated to compare the two calibration matrices. Results are shown below. These standard deviations give an indication of the expected percent error for a random loading application.

Factory Calibration		In-situ Calibration, C	
% Error	Std	% Error	Std
Fx	2.7649	Fx	5.930
Fy	3.0264	Fy	4.0433
Fz	2.1992	Fz	2.0207
Mx	2.2707	Mx	2.2872
My	3.4914	My	14.812
Mz	0.8421	Mz	0.7758

Table 3-2: Standard Deviation of Percent Error Comparison

Table 3-2 does not indicate that the in-situ calibration was better than the factory calibration. In most cases, as a matter of fact, the factory calibration is actually better. However, the in-situ calibration does yield a drag coefficient much closer to the nominally accepted value for a bare cylinder, thus the in-situ calibration is used in the remainder of this chapter.

Based upon the uncertainties above, the drag values listed in this chapter should not be considered accurate on absolute scale, until this calibration issue is resolved. As an example, in the case of Fy (the drag force axis) shown in Table 3-2, the standard deviation of the percent error is as high over four percent. Thus, errors on this order of magnitude should be expected for this direction. Regardless of the absolute measurement, however, some precision can still be expected between differing

orientations (the ability to compare the relative magnitude of one drag value with respect to another).

An example of the measured force/moment output from a run with the bare cylinder is shown below in Figure 3-8. Notice the steady portion of the drag force (and the corresponding steady portion of the pitch moment) and the oscillating component of the lift force due to vortex shedding (and the corresponding oscillating component of the roll moment).

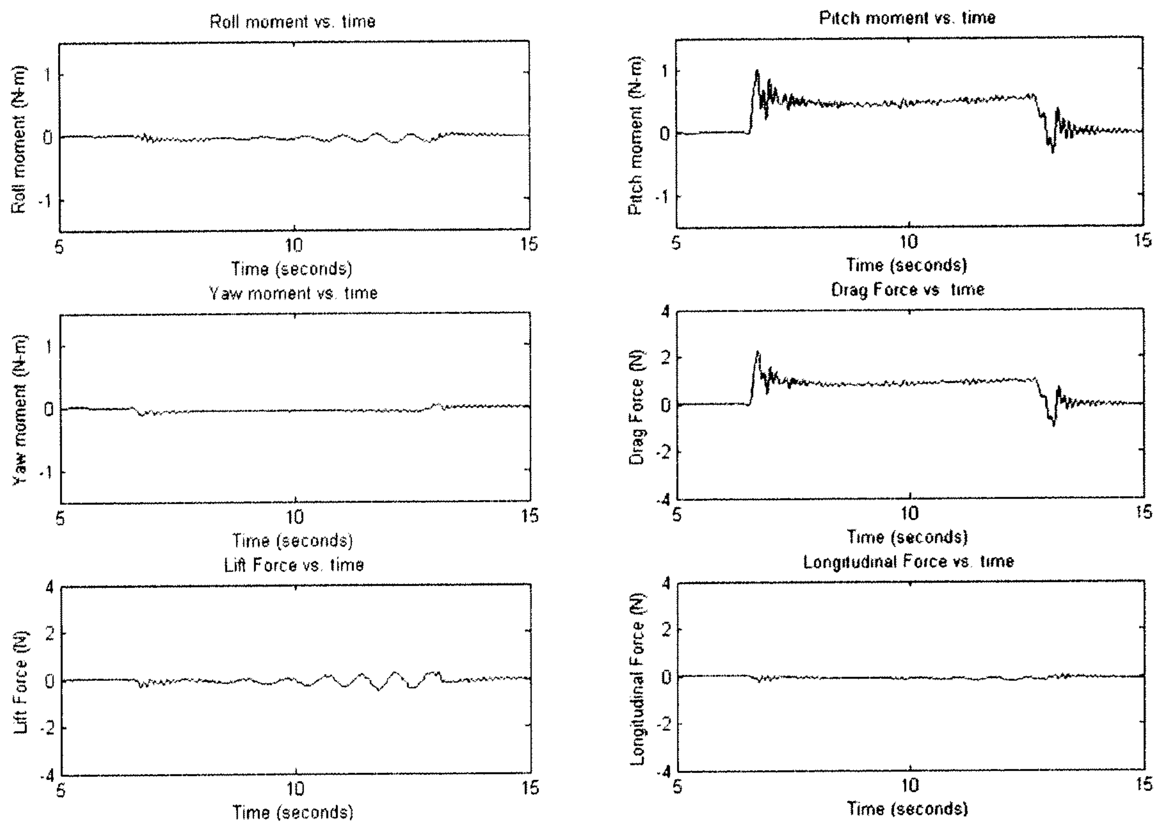

Figure 3-8: Six-Axis Force Output (Bare Cylinder Example)

Before proceeding with the results of this chapter, another limitation of this system must be discussed. The effective length of travel of the cylinder along the tank rails during an experiment is only about 1.25 meters. Traveling at 0.25 m/s, this means that the cylinder will only move for about 5 seconds, and oftentimes, the mean component of the drag force will fluctuate significantly during this short period of time. It is hypothesized that

this fluctuation is a result of the wake pattern not having the opportunity to fully stabilize over the length of the run. Whenever possible, however, a conservative estimate of the drag coefficient is made by selecting the higher portion of the drag force for the calculation. A typical run with an unsteady drag force is shown below in Figure 3-9.

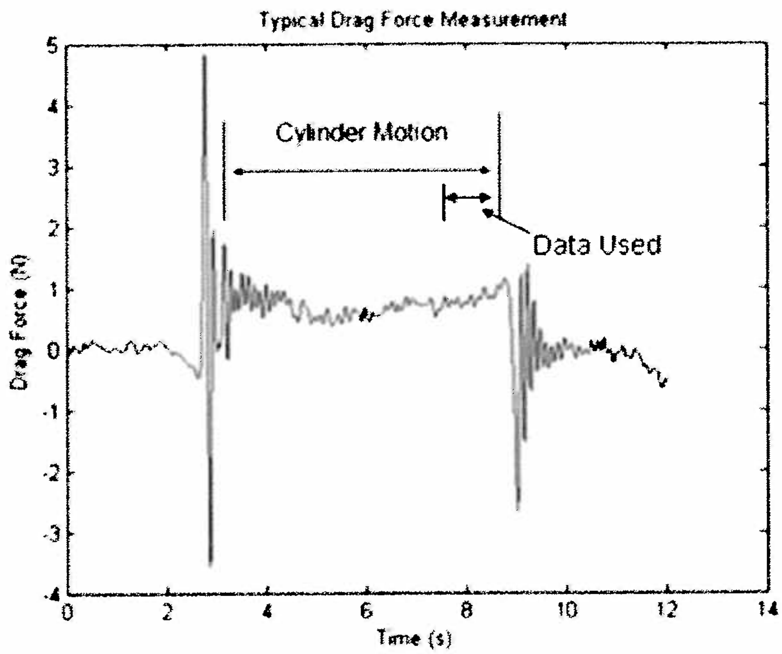

Figure 3-9: Typical Drag Force Time Series During 0.25 m/s Tow (0 A/D)

Notice that the drag force appears to be larger during the beginning and the end of the cylinder motion, but it lower in the mid-section. In a run such as this, the portion of the run used to calculate drag coefficient would be the very end of the run (to estimate a conservatively high drag coefficient). Thus, it should be noted that the precision between drag coefficients of different configurations is no greater than two significant figures, although three significant figures are often displayed in the results section. During future testing, in order to increase the certainty between configurations, multiple tests per configuration must be conducted, and an average drag value calculated.

3.5 Pictures and Results

The results are broken up into three categories: Bare cylinder, Cylinder with triangle, and Cylinder with triangle and airfoil pair.

3.5.1 Bare cylinder

Figure 3-10 shows a one-frame snap-shot of the vorticity forming behind the bare cylinder. Notice the alternating vortex wake. See BC_SP5_AD000.wmv for the video. The flow direction in all pictures and videos from this chapter is from bottom to top.

Bare Cylinder (0.25 m/s)	
Transverse Oscillation	
Amplitude (x/D)	Cd
0 A/D	1.19
0.05 A/D	1.23
0.1 A/D	1.77
0.5 A/D	2.32
1 A/D	2.34

Table 3-3: Bare Cylinder Drag Values

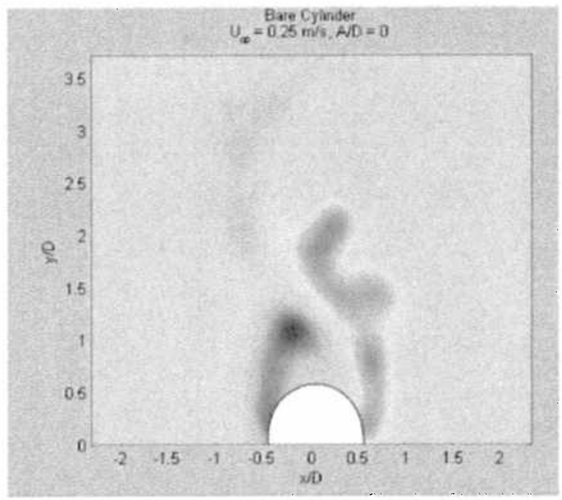

Figure 3-10: Bare Cylinder Vorticity Field

The data in Table 3-3 looks normal, i.e. Cd values increase as the transverse oscillation amplitude increases. Sinusoidal transverse oscillations were forced in these tests at the Strouhal frequency and the amplitude of oscillation specified in the table.

Shown below, in Figure 3-11 is a (frequency domain) power spectra plot of the lift force data for the 0 A/D case. Lift force oscillations (caused by vortex shedding) should occur near the Strouhal frequency, and they do. Strouhal frequency, f_s, equals the Strouhal number (~0.2 for this Reynolds number) times the flow speed (0.25 m/s), divided by the cylinder diameter (0.0381 m). The predicted shedding (Strouhal) frequency is 1.31 Hz, and the actual frequency of oscillations measured is 1.343 Hz.

Throughout this chapter, lift force power spectra are considered only when the cylinder is not forced to oscillate—otherwise it could be expected that the lift force power spectra would be dominated by the oscillation frequency. Looking at the power spectra from the 0 A/D case guarantees that peaks in the power spectra are caused by vortex formation.

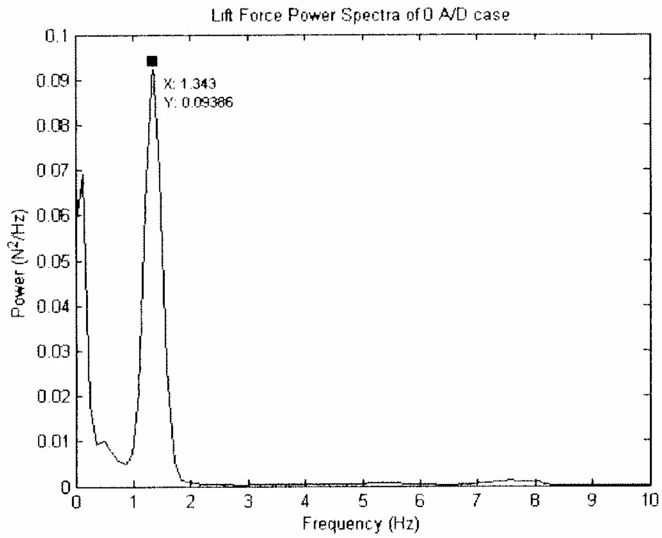

Figure 3-11: Bare Cylinder Lift Force Power Spectra

3.5.2 Cylinder with triangle

This is a one-frame snap-shot of the vorticity forming behind the cylinder with triangle. The height of triangle used in this test, and the tests to follow, is approximately one diameter. It is less clear from this picture if the vortices in the wake are alternately shed from top and bottom. See CylT_SP5_AD000.wmv for the video.

Cylinder w/ Triangle(0.25 m/s)	
Transverse Oscillation Amplitude	Cd
0 A/D	0.83
0.05 A/D	1.05
0.1 A/D	1.15
0.5 A/D	0.50

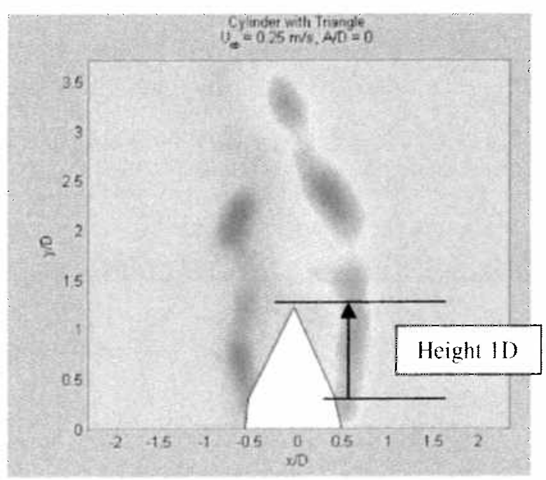

Table 3-4: Cyl w/ Triangle Drag Values **Figure 3-12: Cyl w/ Triangle Vorticity Field**

The drag force of cylinder with triangle is significantly lower than the drag coefficient of the bare cylinder. The Cd data collected (Cd equal to 0.83) corresponds well with the previous work (Cd equal to 0.82) shown in 3.3.1, and here (below) for convenience.

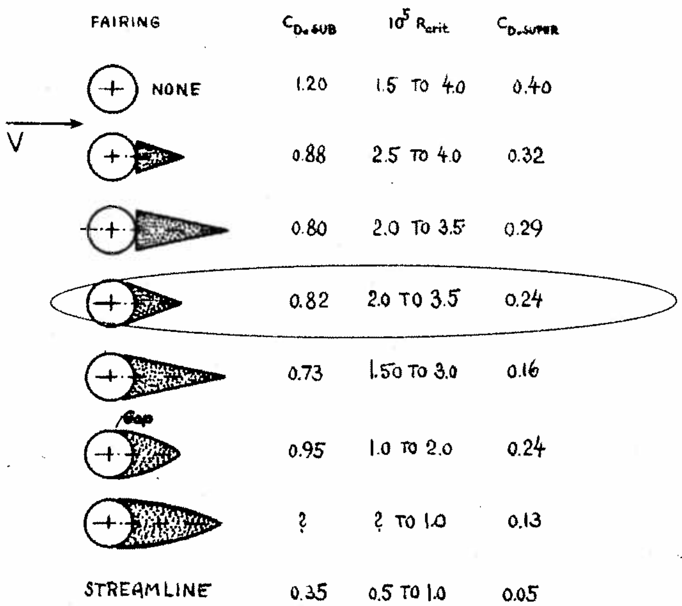

Figure 3-13: Drag Coefficient of Triangle Shapes (same as Figure 3-4) (Hoerner, 1992)

Also, notice the unusually low drag coefficient for the 0.5 A/D test case (when Cd is equal to 0.5). One likely explanation for this decrease in drag force (at the large transverse amplitudes of motion) is that the forced oscillations of the cylinder with triangle are producing a thrust force (opposite the direction of the drag force)—similar to the force that a bird exerts when flapping its wings. The implications of this thrust force on future testing and real-world application is not immediately evident, however.

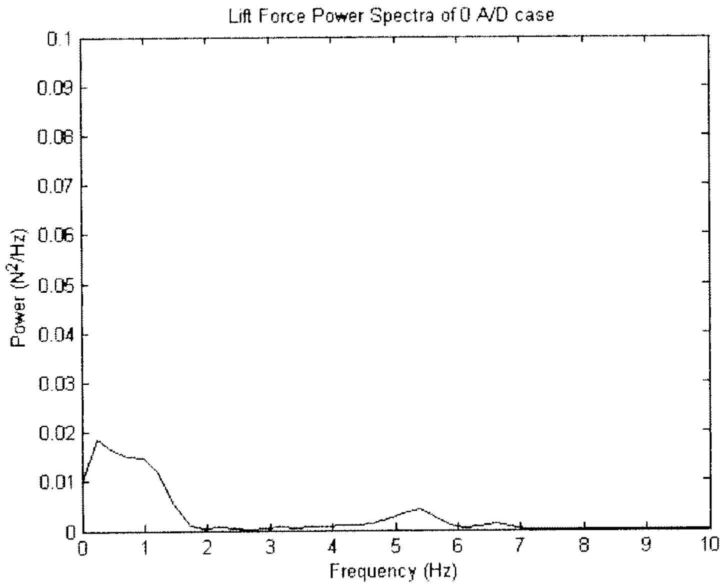

Figure 3-14: Cylinder w/ Triangle Lift Force Power Spectra

Figure 3-14 shows the power spectra of the lift force of the cylinder with triangle. Notice that there is not a peak in the power spectra at the Strouhal frequency (1.31 Hz).

It is noted that the natural frequency of the test cylinder (in bending) throughout this chapter of tests is approximately 4.7 Hz. Thus, a response at this frequency is present in the lift force power spectra for many of the tests in this chapter. A plot of the lift force time series of the cylinder in response to an impulse is shown below in Figure 3-15. The natural frequency can be calculated from this graph.

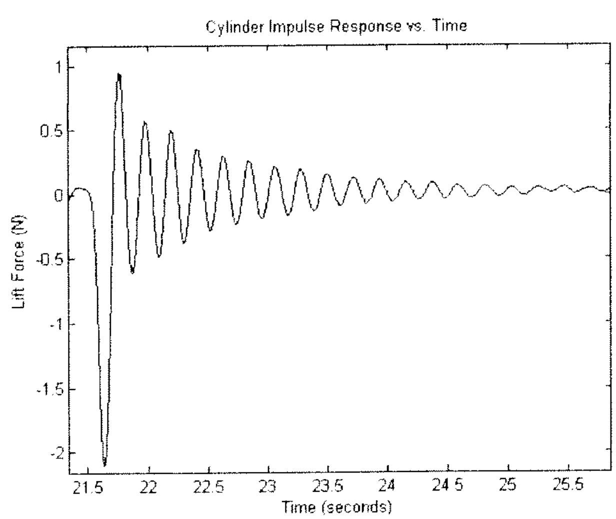

Figure 3-15: Cylinder Impulse Response (Natural Frequency Test)

3.5.3 Cylinder with Triangle and Airfoil Pair

For the cylinder with triangle and airfoil pair experiments, an initial testing matrix was developed (Table 3-3) that specifies the precise location of the airfoil pair (three degrees of freedom). This matrix consists of $2^3 = 8$ tests.

Swivel (degrees, downstream)	0	20
Height (diameters)	1/6	1/3
AoA (degrees)	10	20

Table 3-5: Rigid Cylinder Experiments Testing Matrix

Here, the degrees of freedom (DOF) are defined:

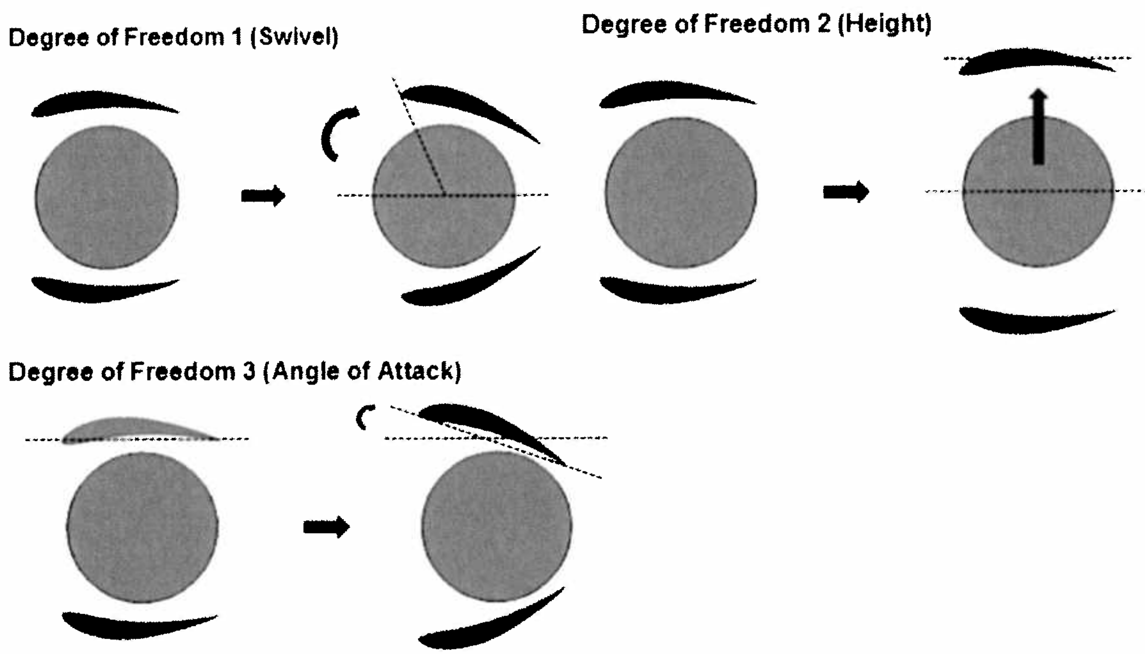

Figure 3-16: Degree of Freedom Pictures

Results of each configuration follow. Skip to 3.6 for a summary.

Height 1/6 D, Swivel 0, AoA 10

Figure 3-17 is a one-frame snap-shot of the vorticity forming behind the cylinder with triangle and airfoil pair with airfoil height 1/6 D, swivel angle 0, and angle of attack 10. It is not clear from this picture if the vortices in the wake are alternately shed from top and bottom. See BCP_SP5_H1_S0_A10_AD000.wmv for the video.

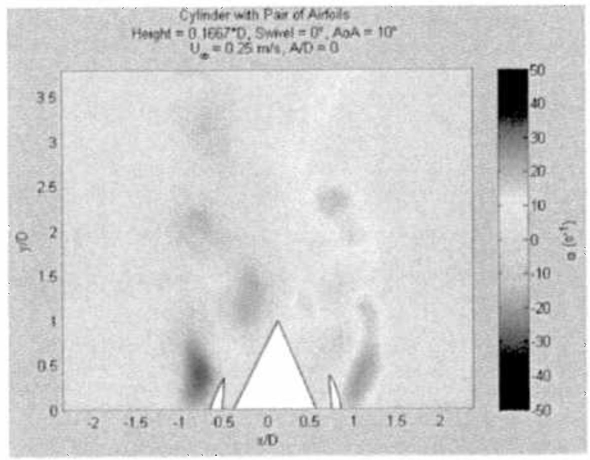

Figure 3-17: H 1/6, S 0, AoA 10 Picture

Height 1/6 D, Swivel 0, AoA 10	
Transverse Oscillation Amplitude (x/D)	Cd
0 A/D	1.74
0.05 A/D	1.81
0.1 A/D	1.12
0.5 A/D	1.19

Table 3-6: H 1/6, S 0, AoA 10 Table

The drag coefficient value at 0 A/D is higher than that of a bare cylinder (1.74 vs. 1.19 respectively), but at 0.5 A/D is much lower than the bare cylinder (1.19 vs. 2.32 respectively). Again, the 0.5 A/D result is likely due to the thrust force generated by the triangle.

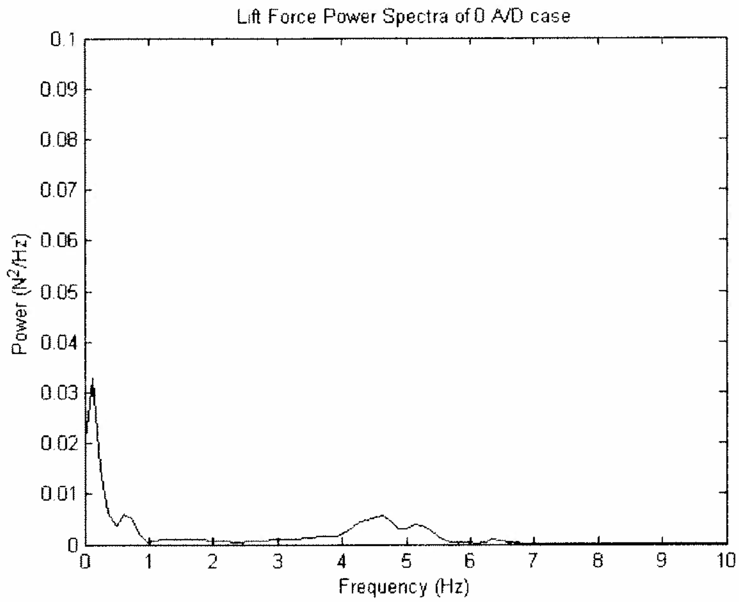

Figure 3-18: Lift Power Spectra, Height 1/6D, Swivel 0, AoA 10

In Figure 3-18, notice that a peak in power does not exist near the Strouhal frequency (1.31 Hz). Thus it can be said that this cylinder with triangle and airfoil pair configuration, as well as the rest of the tests to follow in this chapter, disrupt the usual vortex shedding pattern behind a cylinder.

Height 1/6 D, Swivel 0, AoA 20

Figure 3-19 is a one-frame snap-shot of the vorticity forming behind the cylinder with triangle and airfoil pair with the DOF described above. See BCP_SP5_H1_S0_A20_AD000.wmv for the video.

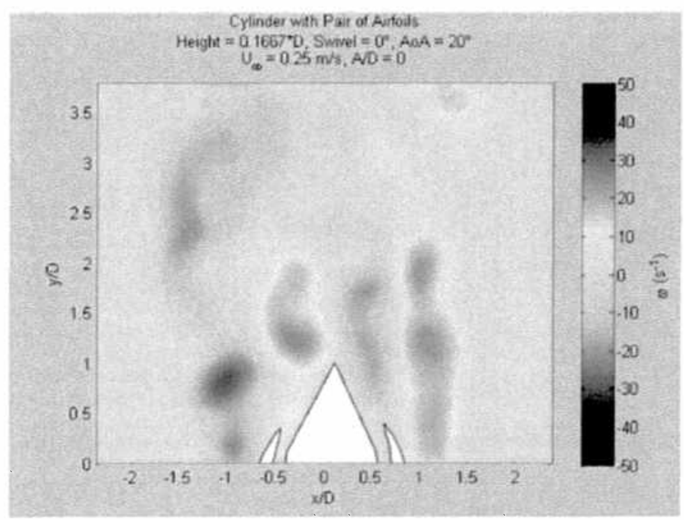

Figure 3-19: H 1/6, S 0, AoA 20 Picture

Height 1/6 D, Swivel 0, AoA 20	
Transverse Oscillation Amplitude (x/D)	Cd
0 A/D	2.33
0.05 A/D	2.27
0.1 A/D	2.12
0.5 A/D	1.88

Table 3-7: H 1/6, S 0, AoA 20 Cd Table

The increased angle of attack of this configuration yields an even higher drag coefficient than the previous configuration. The same trend exists, however, of smaller drag coefficient at larger transverse oscillation amplitudes.

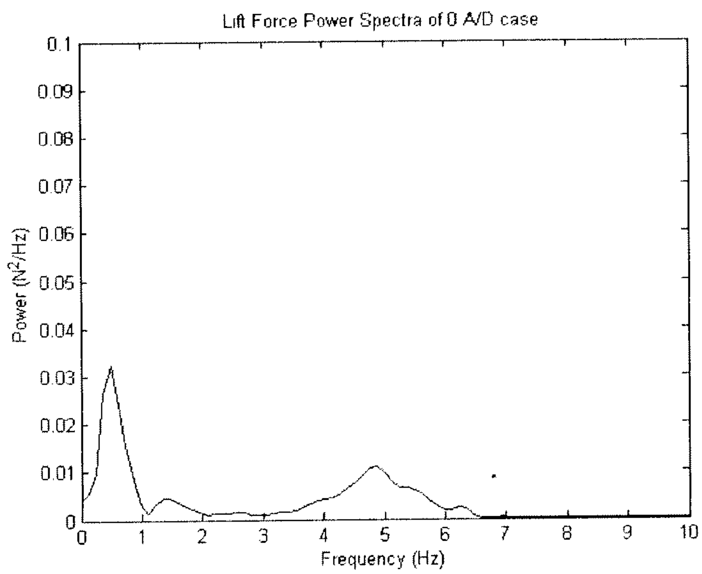

Figure 3-20: Lift Power Spectra, Height 1/6D, Swivel 0, AoA 20

In Figure 3-20, a peak in power does not exist near the Strouhal frequency (1.31 Hz).

Height 1/6 D, Swivel 20, AoA 10

Figure 3-21 is a one-frame snap-shot of the vorticity forming behind the cylinder with triangle and airfoil pair with the DOF above. See BCP_SP5_H1_S20_A10_AD000.wmv for the video.

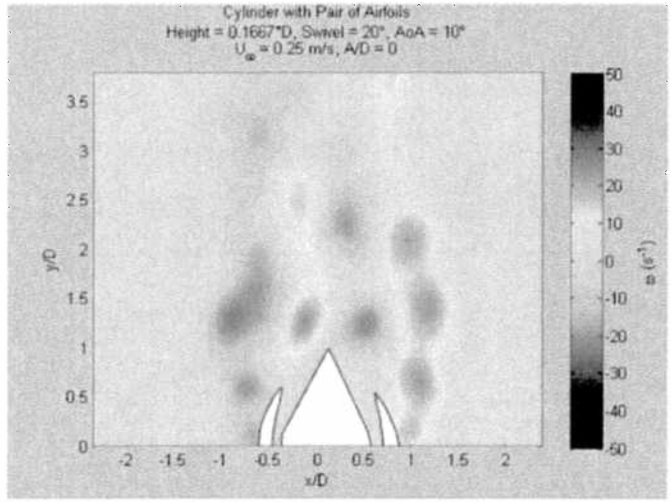

Figure 3-21: H 1/6, S20, AoA 10 Picture

Height 1/6 D, Swivel 20, AoA 10	
Transverse Oscillation Amplitude (x/D)	Cd
0 A/D	1.94
0.05 A/D	1.74
0.1 A/D	1.66
0.5 A/D	1.61

Table 3-8: H 1/6, S 20, AoA 10 Cd Table

The drag coefficient value at 0 A/D is much higher than that of a bare cylinder (1.94 vs. 1.19 respectively). In the next five configurations that follow, the same holds true—drag coefficients are higher than that of the bare cylinder (at least at the 0 A/D transverse oscillation amplitude)—thus they are negative results. The remainder of the tests are merely shown for completeness. Skip to section 3.6 for a summary of the results.

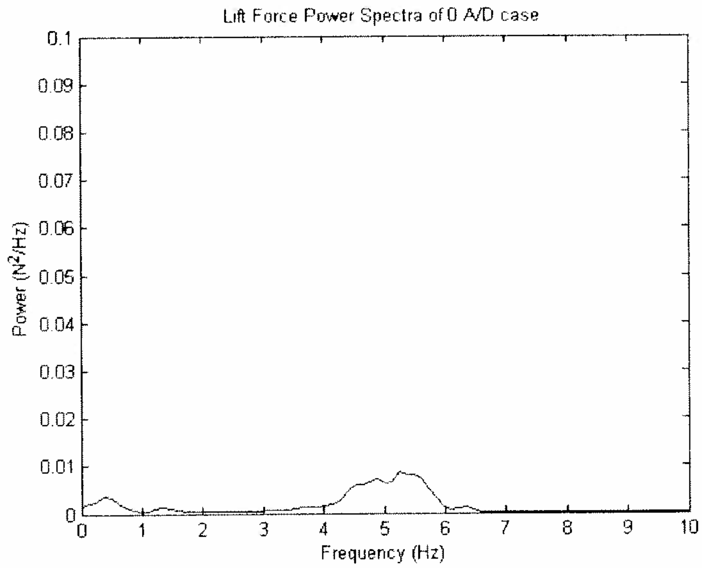

Figure 3-22: Lift Power Spectra, Height 1/6D, Swivel 20, AoA 10

Height 1/6 D, Swivel 20, AoA 20

Figure 3-23 is a one-frame snap-shot of the vorticity forming behind the cylinder with triangle and airfoil pair with the DOF above. See BCP_SP5_H1_S20_A20_AD000.wmv for the video.

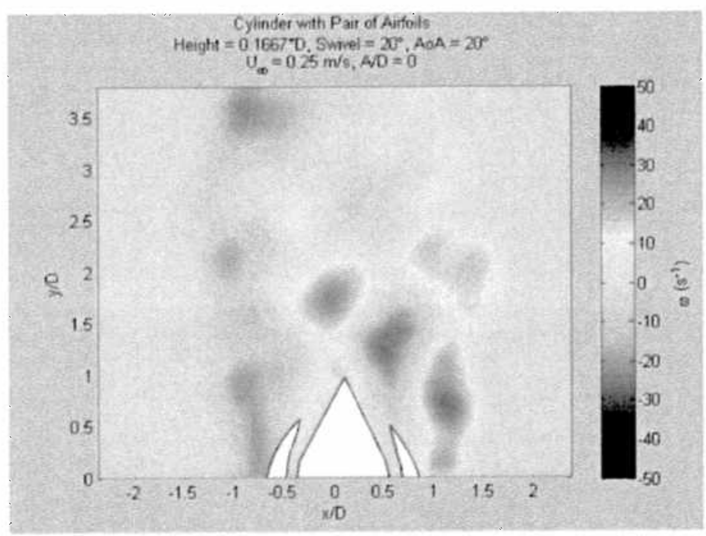

Figure 3-23: H 1/6, S 20, AoA 20 Picture

Height 1/6 D, Swivel 20, AoA 20	
Transverse Oscillation Amplitude (x/D)	Cd
0 A/D	2.14
0.05 A/D	1.83
0.1 A/D	1.91
0.5 A/D	1.95

Table 3-9: H 1/6, S 20, AoA 20 Cd Table

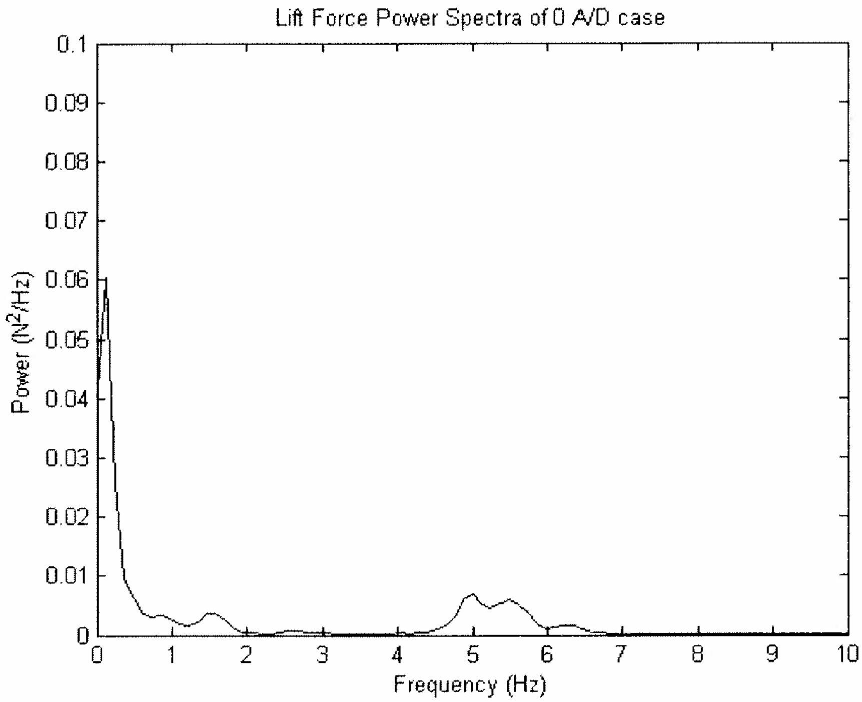

Figure 3-24: Lift Power Spectra, Height 1/6D, Swivel 20, AoA 20

Height 1/3 D, Swivel 0, AoA 10

Figure 3-25 is a one-frame snap-shot of the vorticity forming behind the cylinder with triangle and airfoil pair with the DOF above. See BCP_SP5_H3_S0_A10_AD000.wmv for the video.

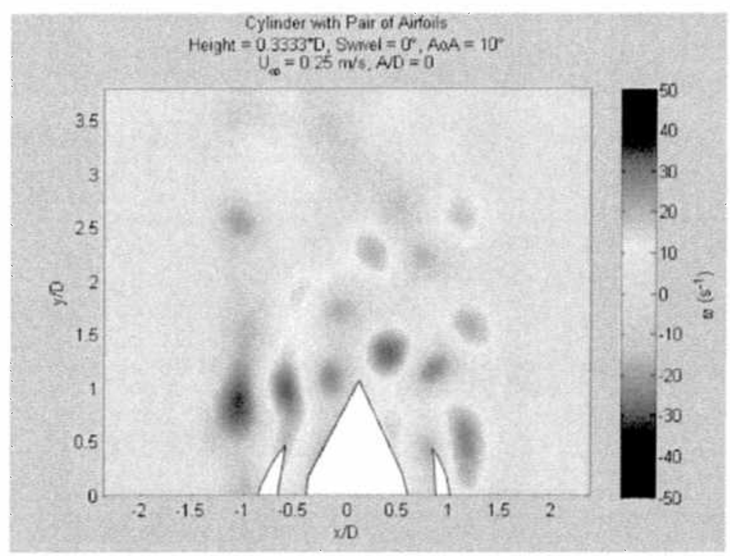

Figure 3-25: H 1/3, S 0, AoA 10 Picture

Height 1/3 D, Swivel 0, AoA 10	
Transverse Oscillation Amplitude (x/D)	Cd
0 A/D	1.69
0.05 A/D	1.61
0.1 A/D	1.72
0.5 A/D	1.26

Table 3-10: H 1/3, S 0, AoA 10 Cd Table

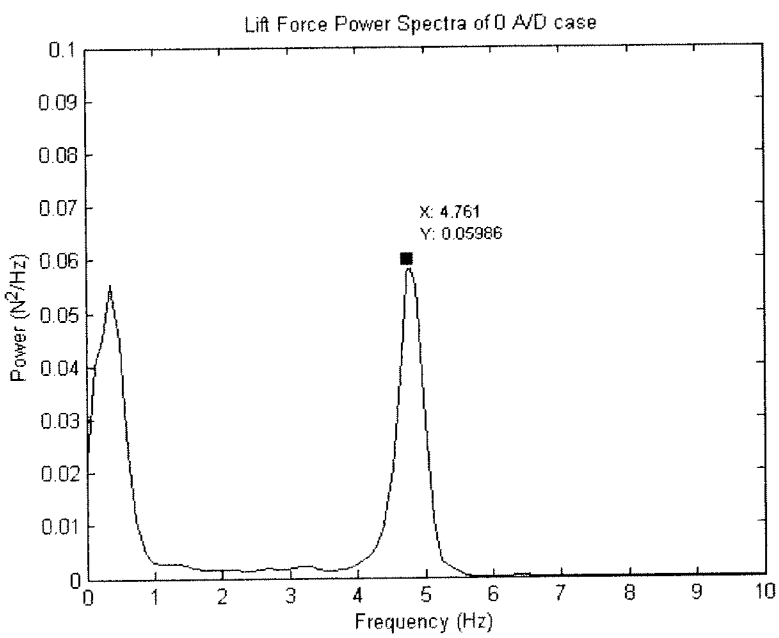

Figure 3-26: Lift Power Spectra, Height 1/3D, Swivel 0, AoA 10

In Figure 3-26, a peak in power does not exist near the Strouhal frequency (1.31 Hz). However, a peak in the power spectra does exist near the natural frequency of the cylinder in bending (~4.7 Hz). Vortex shedding is probably occurring near this frequency that is exciting the left spectra peak.

Height 1/3 D, Swivel 0, AoA 20

Figure 3-27 is a one-frame snap-shot of the vorticity forming behind the cylinder with triangle and airfoil pair with the DOF above. See BCP_SP5_H3_S0_A20_AD000.wmv for the video.

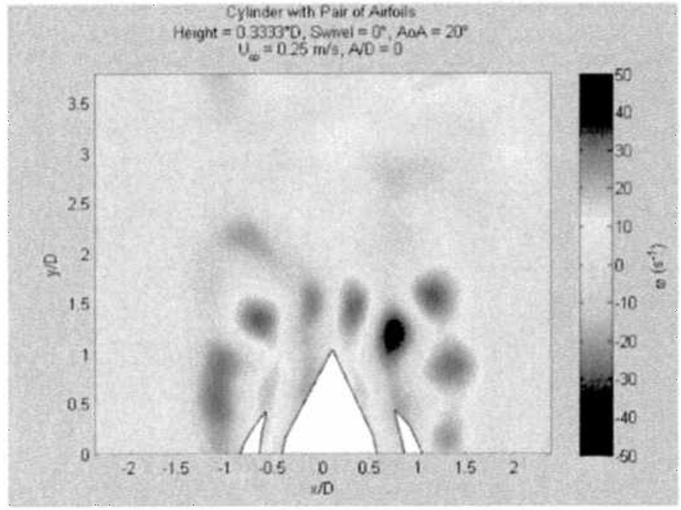

Figure 3-27: H 1/3, S 0, AoA 20 Picture

Height 1/3 D, Swivel 0, AoA 20	
Transverse Oscillation Amplitude (x/D)	Cd
0 A/D	2.09
0.05 A/D	2.12
0.1 A/D	2.32
0.5 A/D	2.10

Table 3-11: H 1/3, S 0, AoA 20 Cd Table

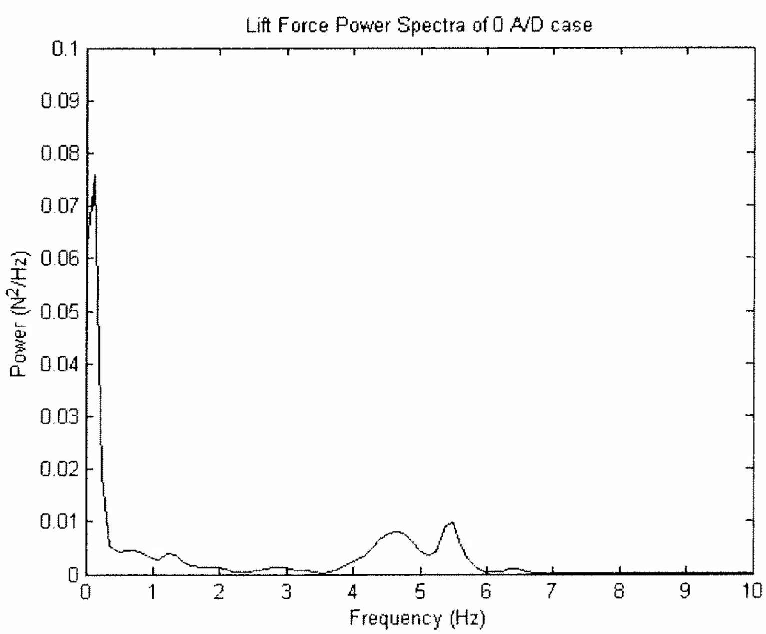

Figure 3-28: Lift Power Spectra, Height 1/3D, Swivel 0, AoA 20

Height 1/3 D, Swivel 20, AoA 10

Figure 3-29 is a one-frame snap-shot of the vorticity forming behind the cylinder with triangle and airfoil pair with the DOF above. See BCP_SP5_H3_S20_A10_AD000.wmv for the video.

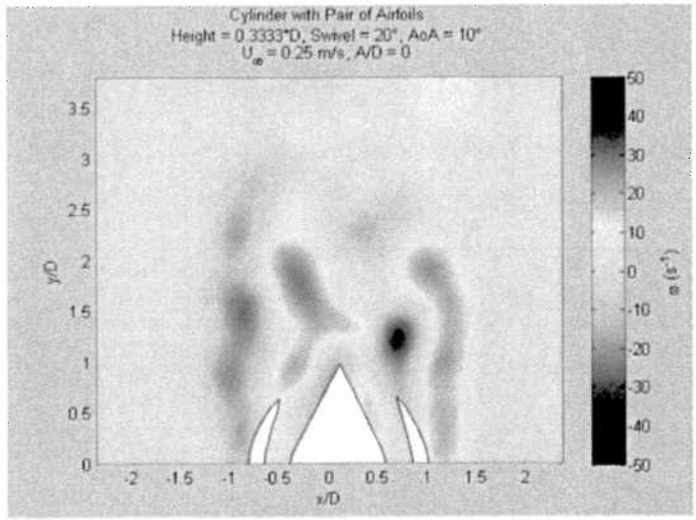

Figure 3-29: H 1/3, S 20, AoA 10 Picture

Height 1/3 D, Swivel 20, AoA 10	
Transverse Oscillation Amplitude (x/D)	Cd
0 A/D	1.75
0.05 A/D	1.72
0.1 A/D	1.87
0.5 A/D	1.52

Table 3-12: H 1/3, S 20, AoA 10 Cd Table

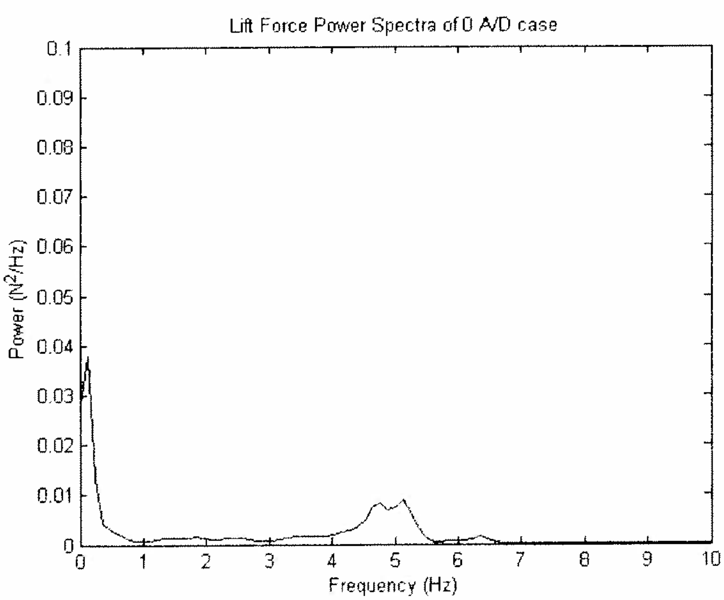

Figure 3-30: Lift Power Spectra, Height 1/3D, Swivel 20, AoA 10

Height 1/3 D, Swivel 20, AoA 20

Figure 3-31 is a one-frame snap-shot of the vorticity forming behind the cylinder with triangle and airfoil pair with the DOF above. See BCP_SP5_H3_S20_A20_AD000.wmv for the video.

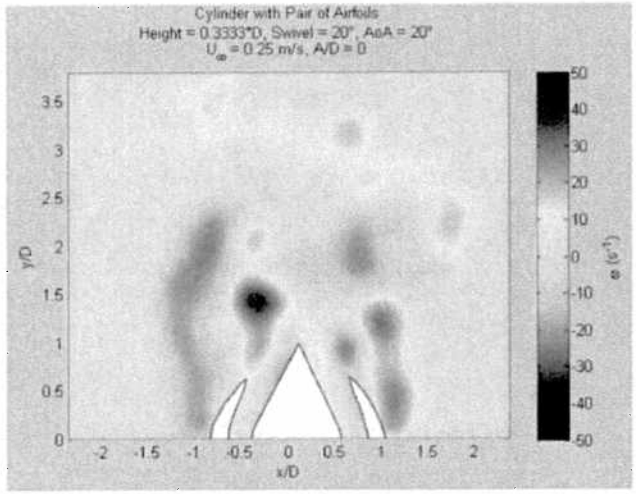

Figure 3-31: H 1/3, S 20, AoA 20 Picture

Height 1/3 D, Swivel 20, AoA 20	
Transverse Oscillation Amplitude (x/D)	Cd
0 A/D	2.00
0.05 A/D	1.96
0.1 A/D	2.18
0.5 A/D	1.57

Table 3-13: H 1/3, S 20, AoA 20 Cd Table

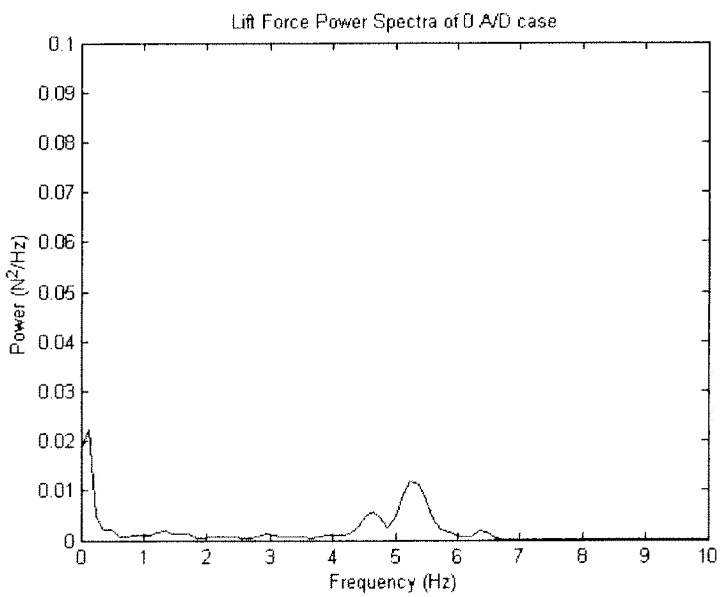

Figure 3-32: Lift Power Spectra, Height 1/3D, Swivel 20, AoA 20

This configuration completes the initial testing matrix.

3.6 Summary of Initial Testing Matrix

The coefficient of drag (Cd) data for all three testing categories are displayed below in Table 3-14. The top four rows identify the cylinder configuration. The last four rows contain the Cd values over a range of vibration amplitudes. All of the tests are conducted with a free stream velocity of 0.25 m/s, which corresponds to Reynolds number ~9,500.

Cat.	I	II	III							
			H1				H3			
	Bare	Cyl. w/	S0		S20		S0		S20	
	Cyl.	Triangle	AoA 10	AoA 20	AoA 10	AoA 20	AoA 10	AoA 20	AoA 10	AoA 20
0 A/D	1.19	0.83	1.74	2.33	1.94	2.14	1.69	2.09	1.75	2.00
0.05 A/D	1.23	1.05	1.81	2.27	1.74	1.83	1.61	2.12	1.72	1.96
0.1 A/D	1.77	1.15	1.12	2.12	1.66	1.91	1.72	2.32	1.87	2.18
0.5 A/D	2.32	0.50	1.19	1.88	1.61	1.95	1.26	2.10	1.52	1.57

Table 3-14: Rigid Cylinder, PIV Initial Test Matrix Summary

A couple of interesting points follow: The cylinder with triangle (Category II) produces the lowest overall drag results. Also, interestingly enough, the cylinder with triangle at 0.5 A/D produces the lowest overall Cd for any of the runs. This seems counter-intuitive when compared to the case of a bare cylinder—where the Cd continues to rise with increasing A/D. However, a lower Cd value with increasing A/D also occurs in many of the other Category III configurations. Generation of thrust force (opposite the direction of drag force) by the triangle during the oscillations is probably the cause of the decreased drag force.

Also, several noteworthy trends exist in the swivel angle and angle of attack variations. All AoA10 cases yield smaller drag coefficients than all of the AoA20 cases (when the other two DOF are held constant). Also, with only one exception, all S0 cases produce smaller drag coefficients than S20 cases (again with the other two DOF held constant).

No correlation seems to exist, however, between the height of the foils off of the cylinder (H1, H3) and the drag coefficient.

Another major discovery should not go unmentioned. In all Category II and III cases, a significant peak does not exist in the power spectra of the lift force near the Strouhal frequency. This indicates that these configurations successfully disrupt the occurrence of the usual vortex shedding off of a cylinder. It is noted, however, that a small amount of power tends to exist near 4.7 Hz for most of the Category III runs, and a significant amount of power exists for one of the cases in particular (height = 1/3D, swivel angle 0, and angle of attack 10). A small peak in the power spectra near the natural frequency of the cylinder is most likely the result of turbulence in the wake of the cylinder exciting small vibrations at the natural frequency of the cylinder, while the significant power spectra peak indicates that some type of regular forcing (probably vortex shedding) is occurring near the natural frequency of the cylinder. However, it is concluded that the strength of this vortex shedding is small in magnitude (compared to the "traditional" shedding strength at the Strouhal frequency) since the power spectra peak is less than the bare cylinder (0.060 N^2/Hz compared with 0.094 N^2/Hz, respectively) despite the fact that excitation is occurring near the natural frequency of the cylinder.

3.7 A New Positive Result

At the time of publication of this report, one other configuration (based upon the trends learned from the initial testing matrix) was also tested. A height of 1/6 diameter, swivel angle of 0 degrees, and angle of attack of 0 degrees was prescribed. The lower angle of attack, it was hypothesized, would lower the drag force on the cylinder. Results are shown here.

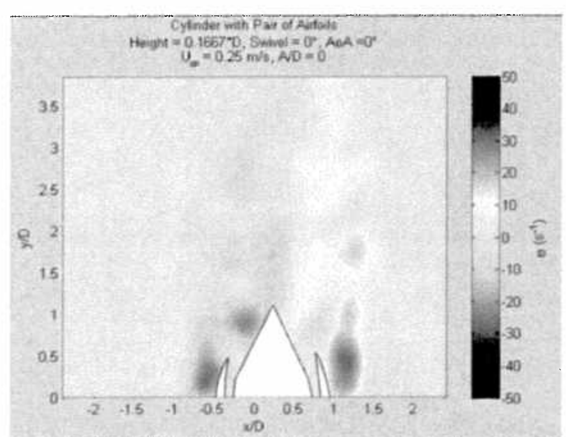

Figure 3-33: H 1/6, S 0, AoA 0 Picture

Height 1/6 D, Swivel 0, AoA 0

Figure 3-33 is a one-frame snap-shot of the vorticity forming behind the cylinder with triangle and airfoil pair with the DOF above. See BCP_SP5_H1_S0_A0_AD000.wmv for the video.

Height 1/6 D, Swivel 0, AoA 10	
Transverse Oscillation Amplitude (x/D)	Cd
0 A/D	0.71
0.05 A/D	1.11
0.1 A/D	0.94
0.5 A/D	0.93

Table 3-15: H 1/6, S 0, AoA 0 Cd Table

Table 3-15 shows that the drag coefficient at 0 A/D is lower than any of the other original tests from this report, and is almost half of the value for the bare cylinder. Clearly, lowering the angle of attack was a step in the right direction.

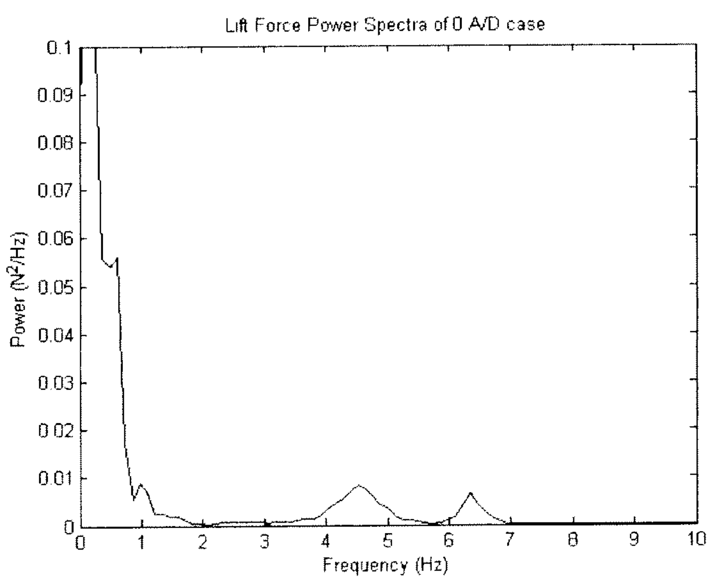

Figure 3-34: Lift Power Spectra, Height 1/6D, Swivel 0, AoA 0

Figure 3-34 shows that regular vortex shedding does not occur near the Strouhal frequency.

3.8 Summary of All Rigid Cylinder, PIV Tests

All of the zero transverse oscillation (0 A/D) configurations tested in this chapter successfully disrupt vortex shedding from occurring at the Strouhal frequency (with the exception of the bare cylinder) as evidenced by the lack of spectral peak at the Strouhal frequency. Thus, from a VIV suppression standpoint, it is difficult to distinguish between the testing configurations.

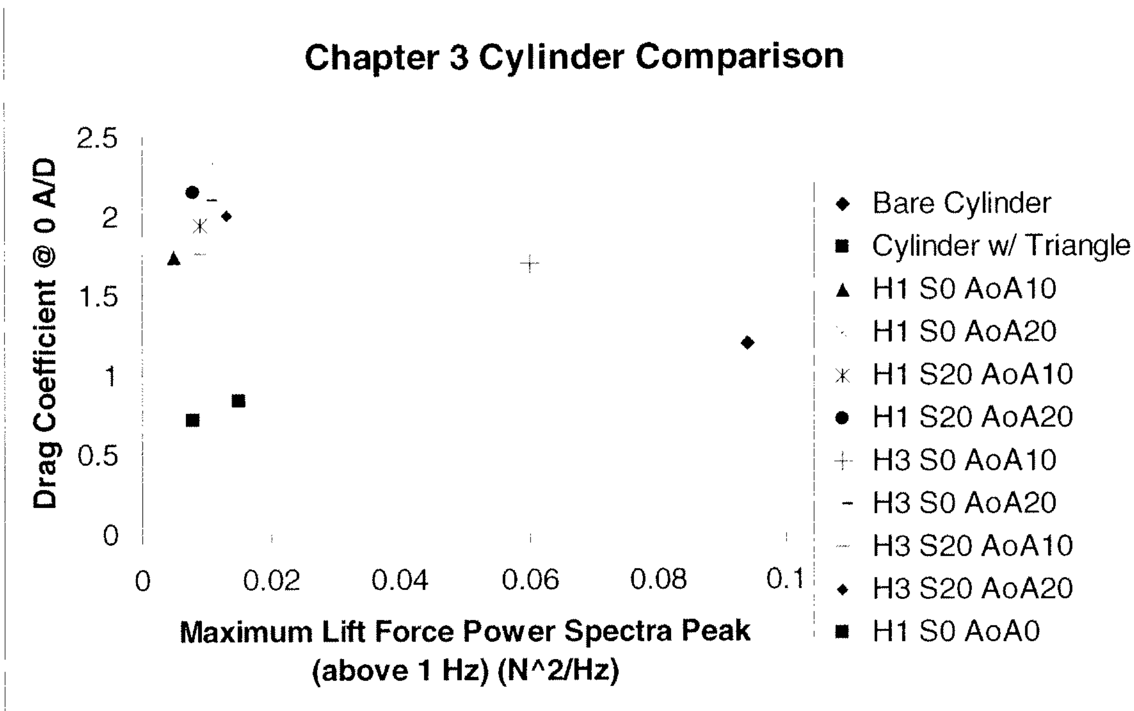

Figure 3-35: Chapter 3 Cylinder Comparison Chart

From a coefficient of drag standpoint, however, as shown in Figure 3-35, the configurations are clearly differentiated. In the legend of the chart above, H1 refers to the height degree of freedom (H1 is 1/6th diameter, while H3 is 1/3rd diameter), S0 refers to a zero swivel angle, and AoA10 refers to a ten degree angle of attack. The lowest coefficient of drag was the final configuration tested (H1 So AoA0 i.e. height 1/6th diameter, swivel angle 0, and angle of attack 0). This Cd value was 0.71. However the lowest overall coefficient of drag (0.5 at 0.5 A/D), and the second lowest drag coefficient

with zero transverse oscillation (0.83 at 0 A/D) was the cylinder with triangle. Clearly, both of these configurations are significant improvements upon the nominally accepted drag value for a cylinder which is 1.2.

One conclusion is as follows: In order to have the lowest drag coefficient during zero transverse oscillation tests, airfoils are a requirement because a cylinder with triangle (alone) does not yield as low of a drag coefficient as a cylinder with triangle and airfoil pair, or as the rigid guide vane test experiments. See Table 3-16.

	Cylinder	Cylinder w/ Triangle	Cylinder w/ Triangle and Airfoil Pair	Cylinder w/ Rigid Guide Vanes
Nominal Drag Coefficient at 0 A/D	1.2	0.83	0.71	0.5-0.7

Table 3-16: Drag Coefficient of Several VIV Suppression Devices

However, the question still remains if a combination of the cylinder with triangle and airfoil pair is an improvement upon the previously tested rigid-guide vane experiments. Further testing suggestions are discussed in the following chapter.

Chapter 4

Future Work and Conclusion

4.1 Future Work

Oftentimes during research, the success or failure of one test will give birth to an idea for future testing. Likewise, the tests conducted during this thesis have spurred ideas for future testing. Below are some of the foreseeable tests that the author thinks lie ahead with VIV suppression utilizing the MIT testing facilities.

4.1.1 PIV with Triangle and Airfoil Pair

The Chapter 3 tests produced several noteworthy trends (i.e. lowering the swivel angle or the angle of attack of the airfoil pair lowers the coefficient of drag). Thus, more testing should be completed with smaller angles of attack, and with smaller swivel angles in order to determine the configuration with the lowest coefficient of drag (at 0 A/D). Once further configurations have been tested, then the configuration with the lowest coefficient of drag should be tested at various Reynolds numbers. This data can then be compared graphically with the rigid guide vane experiment data (Grimminger, 1945), and a determination made if the cylinder with triangle and airfoil pair is indeed an improvement upon the cylinder with rigid guide vanes.

4.1.2 PIV with Rotating Fairing

All of the Chapter 3 tests were with unidirectional, near-wake stabilizers. However, one major concern when developing a unidirectional VIV suppression device is that the ability of the device to disrupt the shedding of vortices (and lower the drag force) changes depending on the angle of the flow with respect to the device. A commonly implemented solution to the problem is to make the suppression device capable of aligning itself with respect to the flow direction (similar to a weather vane that aligns itself in the direction of the wind).

However, during the tests conducted in Chapter 3 the test section was rigid in orientation. If a new design is implemented it should allow the free rotation of the test section during the tests. Free rotation would better simulate an actual marine riser because a unidirectional design (in the ocean) would almost certainly be mounted onto a rotating "fairing" in order to prevent VIV at variable incoming flow directions.

4.1.3 Current and Wave Measurement

As mentioned previously, this thesis only focuses on the effect of a steady current on VIV. The combined effect of current and waves is not explored. However, drag force in an ocean system is a result of both current and waves. Thus, more rigorous testing of a VIV suppression (and drag reduction) device would include testing the effectiveness of the device in a combination of both current and waves. The MIT wave tank with its moving carriage is an ideal setup for this type of test.

4.1.4 Smaller Pitch Ratio with Configuration 1b

As discovered in 2.4.3, decreasing the pitch ratio of this configuration seemed have a positive effect towards reducing the vibration amplitude of the test section. Another test might be completed with a further reduced pitch ratio in order to determine if the vibration amplitude will continue to drop.

4.2 Conclusion

Throughout this thesis, numerous original ideas for VIV suppression and drag reduction are tested. Some of the ideas tested do not yield favorable results in the sense that they do not reduce the vibration amplitude or the drag force of the test section. However, every data point proves valuable in the search for an ideal solution.

On the other hand many positive findings were discovered during this research. A vast majority of the tests were successful in suppressing the vibration and reducing the drag force of the test section—especially in comparison to a bare cylinder undergoing VIV.

A sampling of the results found during the flexible cylinder experiments of Chapter 2 include: the best of the omnidirectional suppression devices (configurations 3 and 3f) nearly eliminate vibration while keeping the drag coefficient around two. The best of the unidirectional configuration tests (configuration 5j(0), 5g(45), 5g(0), and 5(0)) reduce the vibration amplitude of the central cylinder to well below 0.5 A/D, and keep the drag coefficient at or below two.

Several noteworthy results were also found during the rigid cylinder, PIV tests of Chapter 3: the "cylinder with triangle" configuration yields a drag coefficient of 0.83, while the best of the "cylinder with triangle and airfoil pair" devices (shown in 3.7) achieves a drag coefficient as low as 0.71. Both of these are significant reductions when compared to the nominal value of the drag coefficient for a cylinder within this Reynolds number regime. In addition to a very low drag coefficient in a few of the cases, *all* of the Chapter 3 configurations successfully disrupt the shedding of vortices near the Strouhal frequency.

The author hopes that the results and thoughts presented throughout this thesis will help to point towards an optimal solution of the VIV suppression and drag reduction problem—which is of paramount importance in marine riser systems and other applications where cylinders are subjected to a cross flow.

Bibliography

Gopalkrishnan, Ramnarayan. "Vortex Induced Forces on Oscillating Bluff Cylinders" MIT PhD Thesis, 1993, page 76.

Grimminger, G. (1945). The Effect of Rigid Guide Vanes on the Vibration and Drag of a Towed Circular Cylinder. David Taylor Model Basin.

Gyory, Joanna, Arthur J. Mariano, Edward H. Ryan. "The Loop Current." Surface Currents in the Atlantic Ocean. The Cooperative Institute for Marine and Atmospheric Sciences. 09 May 2007 <http://oceancurrents.rsmas.miami.edu/atlantic/loop-current.html>.

Hoerner, Sighard F. Fluid Dynamic Drag. California: Hoerner Fluid Dynamics, 1992. Page 13-19.

Juvinall, Robert C., Marshek, Kurt M. Fundamentals of Machine Component Design: Third Edition. New York: John Wiley & Sons, Inc., 2000.

Kistler Instruments. "PiezoBeam Triaxial Accelerometer, 50g." 9 May 2007. <http://www.kistler.com>.

Kistler Instruments. "Force Sensor with Integrated Electronic Circuitry, 3-comp., Straight Plug Connector." 9 May 2007. <http://www.kistler.com>.

Morgan, Nina. Marine Technology Reference Book. London: Butterworth & Co. Ltd, 1990.

Munson, Bruce R. Young, Donald F. Young, Okiishi, Theodore H. Fundamentals of Fluid Mechanics: Fourth Edition. Hoboken, NJ: John Wiley & Sons, 2002.

Techet, Alex. "13.42 Lecture Vortex Induced Vibrations." MIT-OCW. 21 Apr. 2005. 09 May 2007 <http://ocw.mit.edu/NR/rdonlyres/Mechanical-Engineering.pdf>.

Unimeasure, Inc. "Linear Position Transducers." 9 May 2007. <http://www.unimeasure.com/img--pdf/PDF--STD-images.pdf>.

Wiggins, Andrew. "Multi-Frequency Cable Vibration Experiments." MIT M.S. Thesis, 2005, page 21.

Wood, Tim. "BP's Thunderhorse Platform Still Listing Precariously-- Pictures." Online posting. 13 July 2005. Resource Investor. 9 May 2007. <http://www.resourceinvestor.com/pebble.asp?relid=11305>.

Young, Walter W. Vibration Resistant Overhead Electrical Cable. U.S. Patent 6,353,177 B1. Date of patent Mar. 5, 2002.

Zdravkovich, M.M. (1980). Review and Classification of Various Aerodynamic and Hydrodynamic Means for Suppressing Vortex Shedding. Journal of Wind Engineering and Industrial Aerodynamics, 7 (1981) 145-189.